Sensor and Simulation Notes
Note 128
January 1971

The Diffraction of an Electromagnetic Plane Wave by Interior and Exterior Bends in a Perfectly Conducting Sheet

Lt. Daniel F. Higgins
Air Force Weapons Laboratory

Abstract

Using a method developed by Keller and Blank, the wave equation is solved to give an exact expression for the diffracted magnetic field about a perfectly conducting wedge. From one of Maxwell's curl equations, the corresponding electric field components are written in terms of integrals over certain derivatives of the magnetic field. These results are applied to the diffraction of an incident semi-infinite plane wave propagating parallel to a perfectly conducting sheet when this incoming wave hits an interior or exterior bend in the sheet. For a unit incident electromagnetic plane wave with a step-function time history, the fields were calculated numerically and contour plots of field values in the area surrounding the bend are presented. Such results have obvious application to the diffraction at bends in a parallel plate wave guide. Also, the special case of a plane wave coming to the end of a flat plate (i.e. the limiting case of a very thin wedge) is specifically considered since it describes the diffracted fields at the end of an unterminated wave guide or the edge of a ground plane.

Acknowledgement

I wish to thank Mr. Terry Brown of the Dikewood Corporation for the computer programming and his extensive work in helping to prepare the large number of graphs and contour plots accompanying this note. I would also like to thank Captain Carl Baum for his interest and advice in the preparation of this work.

NOTE 128

THE DIFFRACTION OF AN ELECTROMAGNETIC PLANE WAVE BY INTERIOR AND EXTERIOR BENDS IN A PERFECTLY CONDUCTING SHEET

by

Lt. Daniel F. Higgins

Air Force Weapons Laboratory

January 1971

THE DIFFRACTION OF AN ELECTROMAGNETIC PLANE WAVE BY INTERIOR AND EXTERIOR BENDS IN A PERFECTLY CONDUCTING SHEET

ABSTRACT

Using a method developed by Keller and Blank, the wave equation is solved to give an exact expression for the diffracted magnetic field about a perfectly conducting wedge. From one of Maxwell's curl equations, the corresponding electric field components are written in terms of integrals over certain derivatives of the magnetic field. These results are applied to the diffraction of an incident semi-infinite plane wave propagating parallel to a perfectly conducting sheet when this incoming wave hits an interior or exterior bend in the sheet. For a unit incident electromagnetic plane wave with a step-function time history, the fields were calculated numerically and contour plots of field values in the area surrounding the bend are presented. Such results have obvious application to the diffraction at bends in a parallel plate waveguide. Also, the special case of a plane wave coming to the end of a flat plate (i.e., the limiting case of a very thin wedge) is specifically considered since it describes the diffracted fields at the end of an unterminated waveguide or the edge of a ground plane.

ACKNOWLEDGEMENT

I wish to thank Mr. Terry Brown of the Dikewood Corporation for the computer programming and his extensive work in helping to prepare the large number of graphs and contour plots accompanying this note. I would also like to thank Captain Carl Baum for his interest and advice in the preparation of this work.

I. Introduction

When an electromagnetic plane wave encounters an obstacle, the resultant fields are generally much more complicated than the incoming fields and correspondingly more difficult to calculate. One of the few cases where Maxwell's equations can be solved in closed forms is that of the diffraction of a uniform electromagnetic plane wave at a bend in an infinite, perfectly conducting sheet. If the direction of propagation of the incoming pulse is perpendicular to the straight line formed by the bend, the problem reduces to that of calculating the two-dimensional diffracted fields at a perfectly conducting wedge. If the incident $\vec{H}$ is parallel to the bend and the incoming semi-infinite wave travels along one edge of the two-dimensional wedge (i.e. wedge is infinite in direction perpendicular to cross-section being considered), the magnetic field has only one component and the vector wave equation reduces to the much simpler scalar wave equation. Such restrictions on the incoming pulse are just those required for TEM mode propagation on a wave guide. Thus our results will be directly applicable to the early-time (i.e. before other reflections and diffractions interfere) diffracted fields at a bend in the plates of a parallel plate wave guide.

The problem of diffraction of a scalar plane wave by a wedge has been considered by several people.[1,2] The results of the work by Keller and Blank (reference 1) were applied in an earlier note[3] to calculate the diffracted electromagnetic fields at an interior bend in a conducting plate. This note is an extension of the earlier work where we now consider the case of an exterior bend. (See figure 5 for an explanation of the terms "interior" and "exterior" bends.) The interior and exterior bend problems vary in several respects. First of all, for the interior bend a reflected pulse must be considered, while the exterior bend case has no reflected pulse but a shadow region instead. Perhaps more important is the fact that, as one approaches the bend, $\vec{E}$ goes to zero for the interior bend while $\vec{E}$ approaches infinity for the exterior bend. As in reference 3 we will first calculate $\vec{H}$ using the scalar wave equation and then find $\vec{E}$ from one of Maxwell's equations along with known boundary conditions.

Solutions for the field diffracted by an exterior bend have obvious applications to bends in a parallel plate wave guide. If we let the bend angle α (see figure 5b) approach zero, we have a solution for the fields reflected and diffracted at the end of an unterminated wave guide. And in future notes we also hope to consider using solutions for the two-dimensional case discussed here as approximations for the fields diffracted by more complicated three-dimensional geometries such as a cone-cylinder interface.

II. Diffraction of a Plane Wave by a Perfectly Conducting Wedge

We will first consider the general case of diffraction of a step function plane wave by a perfectly conducting wedge. For completeness we will first repeat some of the development given in reference 3 and then we will depart from the previous work to develop new and mathematically simpler expressions for the diffracted fields.

The incoming plane wave is described by

$$\vec{H}_i = H_o U\left[t - \frac{r}{c}\cos(\phi - \phi_1)\right]\hat{z} \tag{1}$$

where

$H_o = |\vec{H}_i|$ = magnitude of incoming magnetic field

U is the Heaviside unit step function

r, ϕ are coordinates shown in figure 1

c = velocity of propagation of the pulse

t = time (t = 0 when pulse reaches bend)

ϕ_1 is the angle of the direction of propagation with respect to the x-axis

$\hat{z}$ is a unit vector along the bend (see figure 1)

Similarly

$$\vec{E}_i = E_o U\left[t - \frac{r}{c}\cos(\phi - \phi_1)\right]\hat{y} \tag{2}$$

where

$$|\vec{E}_i| = Z_o|\vec{H}_i| \tag{3}$$

Z_o = impedance of free space = $\sqrt{\frac{\mu_o}{\varepsilon_o}} = 120\pi$

(For convenience it is assumed that $\varepsilon = \varepsilon_o$, $\mu = \mu_o$.)

Since the incoming wave arrives at the bend (i.e. origin) at t = 0, the diffracted field can have reached only as far as r = ct at some time t > 0. The bend is just a line along the z-axis; i.e. a surface of zero area. Thus, no net energy is scattered from the bend. This requires both $\vec{E}$ and $\vec{H}$ to be continuous across the surface r = ct. The total $\vec{E}$ and $\vec{H}$ fields must also satisfy the wave equation

$$\nabla^2 \begin{pmatrix} \vec{E} \\ \vec{H} \end{pmatrix} - \frac{1}{c^2} \frac{\partial^2}{\partial t^2} \begin{pmatrix} \vec{E} \\ \vec{H} \end{pmatrix} = 0 \tag{4}$$

along with the boundary conditions at a perfectly conducting plane

$$\begin{aligned} [\vec{E} \cdot \hat{r}]_{\phi_n} &= 0 \\ \left[\frac{\partial \vec{H}}{\partial \phi}\right]_{\phi_n} &= 0 \end{aligned} \tag{5}$$

where ϕ_n describes the perfectly conducting surfaces.

Since $\vec{H}$ has only a component along $\hat{z}$, the vector wave equation reduces to the scalar equation

$$\nabla^2 h_o - \frac{1}{c^2} \frac{\partial^2}{\partial t^2} h_o = 0 \tag{6}$$

where

$$\frac{\vec{H}}{H_o} \equiv h_o \hat{z}$$

(The subscript o will be used to indicate the various diffracted fields for the general case of a plane wave approaching a wedge at an arbitrary angle.) Outside the diffracted region (i.e. r > ct), h_o is just the sum of the incident and reflected fields. Since the fields must be continuous across the boundary r = ct, the diffracted fields are just solutions of the wave

equations which satisfy the known boundary conditions at r = ct and at the surfaces of the wedge.

Now

$$\nabla^2 h_o = \frac{\partial^2 h_o}{\partial x^2} + \frac{\partial^2 h_o}{\partial y^2}$$

$$= \frac{1}{r}\frac{\partial}{\partial r}\left(r\frac{\partial h_o}{\partial r}\right) + \frac{1}{r^2}\frac{\partial^2 h_o}{\partial \phi^2} \tag{7}$$

where it is assumed that h_o is independent of z. If one considers the diffracted region as it expands with time, it can be seen that the only characteristic length of the problem is r = ct. Thus h_o has to be a function r/ct rather than of r or t separately. Therefore, define the variables

$$p = ct\left[1 - \left(\frac{r}{ct}\right)^2\right]^{1/2} \tag{8}$$

$$q = \left[1 - \left(\frac{r}{ct}\right)^2\right]^{1/2} \tag{9}$$

and when we write the wave equation in terms of p and q, one gets

$$-\frac{1}{q^2}\frac{\partial}{\partial p}\left(p^2\frac{\partial h_o}{\partial p}\right) - \frac{\partial}{\partial q}\left([q^2-1]\frac{\partial h_o}{\partial q}\right) - \frac{1}{q^2-1}\frac{\partial^2 h_o}{\partial \phi} = 0 \tag{10}$$

However, since h_o is only a function of ϕ and r/ct, it must be independent of p. Then equation 10 reduces to

$$\frac{\partial}{\partial q}\left([q^2-1]\frac{\partial h_o}{\partial q}\right) + \frac{1}{q^2-1}\frac{\partial^2 h_o}{\partial \phi^2} = 0 \tag{11}$$

Making the further change of variable

$$\rho = \left(\frac{q - 1}{q + 1}\right)^{1/2} = \left\{\frac{ct}{r} + \left[\left(\frac{ct}{r}\right)^2 - 1\right]^{1/2}\right\}^{-1} \tag{12}$$

the above equation becomes

$$\frac{1}{\rho}\frac{\partial}{\partial\rho}\left(\rho\,\frac{\partial h_o}{\partial\rho}\right) + \frac{1}{\rho^2}\,\frac{\partial^2 h_o}{\partial\phi^2} = 0 \tag{13}$$

which is just the Laplace equation in a cylindrical (ρ, ϕ) coordinate system with $\rho = 0$ at $r = 0$ and $\rho = 1$ at $r = ct$.

Thus we must solve the Laplace equation subject to the boundary conditions of field continuity across a circular sector at $\rho = 1$ and $[\partial h_o/\partial\phi]_{\phi_n} = 0$ on the conducting surface of the wedge. The circular sector is mapped into a semicircle in the upper half of the W-plane by the conformal transformation

$$W = \left(e^{-i\phi_o}\rho e^{i\phi}\right)^{\lambda} \tag{14}$$

where

$$\lambda = \frac{1}{2}\left[1 - \frac{\phi_o}{\pi}\right]^{-1} \tag{15}$$

The above transformation is for a wedge of angle $\alpha = 2\phi_o$ which is bisected by the x-z plane (see figure 1). If a point in the W-plane is described by the polar coordinates (R, ω) (see figure 2), then

$$R = \rho^{\lambda} \tag{16}$$

$$\omega = \lambda(\phi - \phi_o) \tag{17}$$

By forming an image of the semicircle below the real axis, we obtain the problem of solving Laplace's equation given boundary conditions on a unit circle. For the wedge, we have two cases:

(1) If $0 < \phi_1 < \phi_o$, we have reflected pulses on both sides of the wedge (see figure 3a). Thus at $r = ct$

$$h_o = 2 \text{ for } \phi_o < \phi < \phi_2 \tag{18}$$

$$h_o = 1 \text{ for } \phi_2 < \phi < 2\pi - \phi_3 \tag{19}$$

$$h_o = 2 \text{ for } 2\pi - \phi_3 < \phi < 2\pi - \phi_o \tag{20}$$

where

$$\phi_2 = 2\phi_o - \phi_1 \tag{21}$$

$$\phi_3 = 2\phi_o + \phi_1 \tag{22}$$

When mapped into the complex W-plane, we get corresponding boundary conditions on the unit circle.

$$h_o = 2 \text{ for } 0 < \omega < \omega_1 = \lambda(\phi_2 - \phi_o) \tag{23}$$

$$h_o = 1 \text{ for } \omega_1 < \omega < \omega_2 = \lambda(2\pi - \phi_3 - \phi_o) \tag{24}$$

$$h_o = 2 \text{ for } \omega_2 < \omega < \pi \tag{25}$$

where image regions below the real axis have the same boundary values as the corresponding regions above the real axis. Thus $\partial h_o/\partial \phi$ will be zero along the real axis, which corresponds to the conducting edges of the wedge.

(2) When $\phi_o < \phi_1$, we get both a reflected region and a shadow region (see figure 3b). On the unit circle in the complex plane the boundary conditions become

$$h_o = 0 \text{ for } 0 < \omega < \omega_1 = \lambda(\phi_1 - \phi_o) \tag{26}$$

$$h_o = 1 \text{ for } \omega_1 < \omega < \omega_2 = \lambda(2\pi - \phi_3 - \phi_o) \tag{27}$$

where in this case $\phi_3 = \phi_o + \phi_1$

$$h_o = 2 \text{ for } \omega_2 < \omega \tag{28}$$

with corresponding values below the real axis.

Thus the problem becomes one of solving the Laplace equation subject to different constant boundary values along various arcs of the unit circle. By superposition, the solution may be written as the sum of solutions which take on a specified constant value on one arc of the circle and zero value over the rest of the boundary. Therefore, we want a harmonic function v which has the boundary condition v = C on the arc $\omega_b \geq \omega \geq \omega_a$ of the unit circle and v = 0 elsewhere on the circle. It can be shown that

$$v = \text{Im } f(W) \tag{29}$$

where

$$f(W) = \frac{C}{\pi} \ln\left[\frac{W - e^{i\omega_b}}{W - e^{i\omega_a}}\right] - \frac{iC}{\pi}(\omega_b - \omega_a) \tag{30}$$

Using transformations of this type, Keller and Blank (reference 1) obtain the following expressions for h_o:

(1) For $0 < \phi_1 < \phi_o$

$$h_o = 1 + \frac{1}{\pi}\tan^{-1}\left\{\frac{(1-\rho^{2\lambda})\cos\lambda(\phi_1-\pi)}{(1+\rho^{2\lambda})\sin\lambda(\phi_1-\pi) - 2\rho^{\lambda}\sin\lambda(\phi-\pi)}\right\}$$

$$+ \frac{1}{\pi}\tan^{-1}\left\{\frac{-(1-\rho^{2\lambda})\cos\lambda(\phi_1+\pi)}{(1+\rho^{2\lambda})\sin\lambda(\phi_1+\pi) - 2\rho^{\lambda}\sin\lambda(\phi-\pi)}\right\} \tag{31}$$

(2) For $\phi_1 > \phi_o$

$$h_o = 1 - \frac{1}{\pi}\tan^{-1}\left\{\frac{-(1-\rho^{2\lambda})\cos\lambda(\phi_1-\pi)}{(1+\rho^{2\lambda})\sin\lambda(\phi_1-\pi) - 2\rho^{\lambda}\sin\lambda(\phi-\pi)}\right\}$$

$$+ \frac{1}{\pi}\tan^{-1}\left\{\frac{-(1-\rho^{2\lambda})\cos\lambda(\phi_1+\pi)}{(1+\rho^{2\lambda})\sin\lambda(\phi_1+\pi) - 2\rho^{\lambda}\sin\lambda(\phi-\pi)}\right\} \qquad (32)$$

where for both cases above the value of the arctangent is taken to be in the interval between 0 and π.

An equivalent expression for h_o which holds for any direction of incidence has been developed by Friedlander by the use of Green's functions.[2] In Friedlander's notation

$$h_o = \frac{1}{\pi}\tan^{-1}\left[\frac{\sinh \kappa\xi \sin \kappa\pi}{\cosh \kappa\xi \cos \kappa\pi - \cos \kappa(\theta-\theta_o)}\right]$$

$$+ \frac{1}{\pi}\tan^{-1}\left[\frac{\sinh \kappa\xi \sin \kappa\pi}{\cosh \kappa\xi \cos \kappa\pi - \cos \kappa(\theta+\theta_o)}\right] \qquad (33)$$

where

$$\xi = \cosh^{-1}\frac{ct}{r} \equiv \cosh^{-1}\tau \qquad (34)$$

$$\kappa = \frac{\pi}{\beta} = \frac{\pi}{2\pi - \alpha} \qquad (35)$$

α is the wedge angle

θ is the polar angle as measured from one face of the wedge

θ_o is the angle of incidence of the incoming plane wave (see figure 4)

Again the arctangent is evaluated in the range from 0 to π.

Friedlander's notation is easily related to that of Keller and Blank.

$$\alpha = 2\phi_o \tag{36}$$

$$\lambda = \kappa \tag{37}$$

$$\theta = \phi - \phi_o = \phi - \frac{\alpha}{2} \tag{38}$$

$$\theta_o = \phi_1 - \phi_o \tag{39}$$

and the expressions can be shown to be equivalent by considering that $\cosh^{-1}\tau = \xi$ implies

$$\tau = \cosh \xi \tag{40}$$

$$\sinh \xi = \sqrt{\cosh^2 - 1} \tag{41}$$

Therefore, from equation 12

$$\rho = \frac{1}{\tau + (\tau^2-1)^{1/2}} = \frac{1}{\cosh \xi + \sinh \xi} = e^{-\xi} \tag{42}$$

Thus

$$(1-\rho^{2\lambda}) = 1 - e^{-2\kappa\xi} = 2e^{-\kappa\xi} \sinh \kappa\xi \tag{43}$$

$$(1+\rho^{2\lambda}) = 2e^{-\kappa\xi} \cosh \kappa\xi \tag{44}$$

Upon substituting these expressions into the Keller and Blank formulas equation 33 is shown to be equivalent to both equations 31 and 32.

The Friedlander expression for h_o (equation 33) is found to be easier to work with than the Keller and Blank expressions (equations 31 and 32) are, and therefore will be used throughout the rest of this note.

Using the method described in reference 3, we can find the electric field from the Maxwell curl equation

$$\nabla \times \vec{H} = \varepsilon \frac{\partial \vec{E}}{\partial t} \tag{45}$$

Now put

$$\frac{\vec{H}}{H_o} \equiv \vec{h}_o \equiv h_o \hat{z} \tag{46}$$

$$\vec{E} \equiv \sqrt{\frac{\mu_o}{\varepsilon_o}}\, \vec{e}_o \tag{47}$$

and since

$$c = \sqrt{\frac{1}{\varepsilon_o \mu_o}} \tag{48}$$

the above curl equation reduces to

$$\nabla \times \vec{h}_o = \frac{\partial \vec{e}_o}{\partial (ct)} \tag{49}$$

When we define $\tau \equiv ct/r$ equation 49 becomes

$$r\nabla \times \vec{h}_o = \frac{\partial \vec{e}_o}{\partial \tau} \tag{50}$$

which, when written in cylindrical coordinates gives

$$\frac{\partial e_{o_r}}{\partial \tau} = \frac{\partial h_o}{\partial \theta} \tag{51}$$

$$\frac{\partial e_{o_\theta}}{\partial \tau} = -r \frac{\partial h_o}{\partial r} = -r \frac{\partial \xi}{\partial r} \frac{\partial h_o}{\partial \xi} \tag{52}$$

Thus

$$e_{o_r}(\tau) = \int_1^\tau \frac{\partial h_o}{\partial \theta}\, d\tau' + C_1 \tag{53}$$

$$e_{o_\theta}(\tau) = \int_1^\tau -r\, \frac{\partial \xi}{\partial r}\, \frac{\partial h_o}{\partial \xi}\, d\tau' + C_2 \tag{54}$$

where C_1 and C_2 are functions independent of τ whose values are determined by the requirement of continuity across the circular sector defined by $\tau = 1$. Also note that since we are integrating a partial derivative with respect to τ the integrals must be considered along a path of constant θ.

Now consider the partial derivatives of h_o appearing in the integrands of equations 53 and 54. Using equation 33 for h_o, one obtains

$$\frac{\partial h_o}{\partial \theta} = -\frac{\kappa}{\pi} \sinh\kappa\xi \sin\kappa\pi \left[\frac{\sin\kappa(\theta-\theta_o)}{[\cosh\kappa\xi \cos\kappa\pi - \cos\kappa(\theta-\theta_o)]^2 + \sinh^2\kappa\xi \sin^2\kappa\pi} \right.$$

$$\left. + \frac{\sin\kappa(\theta+\theta_o)}{[\cosh\kappa\xi \cos\kappa\pi - \cos\kappa(\theta+\theta_o)]^2 + \sinh^2\kappa\xi \sin^2\kappa\pi} \right] \tag{55}$$

$$-r\, \frac{\partial \xi}{\partial r} = -r\, \frac{\partial}{\partial r}\left[\cosh^{-1}\left(\frac{ct}{r}\right)\right] = \frac{\tau}{\sqrt{\tau^2 - 1}} \tag{56}$$

$$\frac{\partial h_o}{\partial \xi} = \frac{\kappa}{\pi} \sin\kappa\pi \left[\frac{\cos\kappa\pi - \cosh\kappa\xi \cos\kappa(\theta-\theta_o)}{[\cosh\kappa\xi \cos\kappa\pi - \cos\kappa(\theta-\theta_o)]^2 + \sinh^2\kappa\xi \sin^2\kappa\pi} \right.$$

$$\left. + \frac{\cos\kappa\pi - \cosh\kappa\xi \cos\kappa(\theta+\theta_o)}{[\cosh\kappa\xi \cos\kappa\pi - \cos\kappa(\theta+\theta_o)]^2 + \sinh^2\kappa\xi \sin^2\kappa\pi} \right] \tag{57}$$

In evaluating e_{or} and $e_{o\theta}$, the integrals were calculated numerically. No particular problem occurred in evaluating

$$\int^{\tau} \frac{\partial h_o}{\partial \theta} d\tau'$$

but difficulties appeared with the convergence of the numerical integration of

$$\int_1^{\tau} -r \frac{\partial \xi}{\partial r} \frac{\partial h_o}{\partial \xi} d\tau' = \int_1^{\tau} \frac{\tau'}{\sqrt{\tau'^2 - 1}} \frac{\partial h_o}{\partial \xi} d\tau' \tag{58}$$

due to the fact that the denominator of the integrand goes to zero at the lower limit of the integral. One can avoid this problem by integrating over ξ instead of τ'. Since

$$\xi = \cosh^{-1}\tau \tag{59}$$

$$\tau = \cosh\xi \tag{60}$$

$$d\tau = \sinh\xi \, d\xi = \sqrt{\tau^2 - 1} \, d\xi \tag{61}$$

Thus

$$\int_1^{\tau} -r \frac{\partial \xi}{\partial r} \frac{\partial h_o}{\partial \xi} d\tau' = \int_o^{\xi(\tau)} \cosh\xi \frac{\partial h_o}{\partial \xi} d\xi \tag{62}$$

When written in this form, the rate of convergence of the integral, using Gaussian quadrature numerical integration techniques, was greatly increased. The numerical convergence was worst along $|\theta \pm \theta_o| = \pi$ (i.e. the boundary line between various shadow and reflected regions); along that line the integrals are accurate to 10^{-4}. Elsewhere, accuracy exceeds 10^{-6}.

III. The Interior Bend

The case of the interior bend is shown in figure 5a. The interior bend is just a special case of the more general wedge diffraction formulas developed in section II where now the wedge angle is

$$\alpha = 2\phi_o \tag{63}$$

and the incoming pulse is traveling at the angle

$$\theta_o = \frac{\beta}{2} = \frac{2\pi - \alpha}{2} = \pi - \phi_o \tag{64}$$

From symmetry considerations, a conducting plane can be placed along the bisector of the wedge without disturbing the fields. Thus we have the appropriate diffracted fields for the interior bend by substituting the above expressions in the diffraction formulas derived for the wedge.

Since the interior bend was discussed in reference 3, the field expressions will simply be listed here in a slightly simpler form. The subscript I will be used to indicate fields referring to the interior bend.

From equation 33

$$h_I = \frac{1}{\pi}\tan^{-1}\left[\frac{\sinh\kappa\xi\ \sin\kappa\pi}{\cosh\kappa\xi\ \cos\kappa\pi - \sin\kappa\theta}\right]$$

$$+ \frac{1}{\pi}\tan^{-1}\left[\frac{\sinh\kappa\xi\ \sin\kappa\pi}{\cosh\kappa\xi\ \cos\kappa\pi + \sin\kappa\theta}\right] \tag{65}$$

where we have used the fact that

$$\cos\left[\kappa\left(\theta \pm \frac{\beta}{2}\right)\right] = \mp\sin\kappa\theta \tag{66}$$

since $\kappa = \pi/\beta$. Similarly, from equations 53, 54, and 62

$$e_{I_r} = \int_1^{\tau} \frac{\partial h_I}{\partial\theta}\, d\tau' + C_{1_I} \tag{67}$$

$$e_{I_\theta} = \int_o^{\xi(\tau)} \cosh\xi\, \frac{\partial h_I}{\partial\xi}\, d\xi + C_{2_I} \tag{68}$$

where for the interior bend

$$C_{1_I} = \begin{cases} [1+\cos\alpha]\,\sin\left(\theta+\frac{\alpha}{2}\right) - \sin\alpha\,\cos\left(\theta+\frac{\alpha}{2}\right) & \text{for } \theta < \frac{\alpha}{2} \\ \sin\left(\theta+\frac{\alpha}{2}\right) & \text{for } \theta > \frac{\alpha}{2} \end{cases} \tag{69}$$

$$C_{2_I} = \begin{cases} \sin\alpha\,\sin\left(\theta+\frac{\alpha}{2}\right) + [1+\cos\alpha]\,\cos\left(\theta+\frac{\alpha}{2}\right) & \text{for } \theta < \frac{\alpha}{2} \\ \cos\left(\theta+\frac{\alpha}{2}\right) & \text{for } \theta > \frac{\alpha}{2} \end{cases} \tag{70}$$

while from equations 55 and 57

$$\frac{\partial h_I}{\partial\theta} = -\frac{\kappa}{\pi}\,\sinh\kappa\xi\,\sin\kappa\pi\left[\frac{-\cos\kappa\theta}{[\cosh\kappa\xi\,\cos\kappa\pi - \sin\kappa\theta]^2 + \sinh^2\kappa\xi\,\sin^2\kappa\pi}\right.$$

$$\left. + \frac{\cos\kappa\theta}{[\cosh\kappa\xi\,\cos\kappa\pi + \sin\kappa\theta]^2 + \sinh^2\kappa\xi\,\sin^2\kappa\pi}\right] \tag{71}$$

$$\frac{\partial h_I}{\partial\xi} = \frac{\kappa}{\pi}\,\sin\kappa\pi\left[\frac{\cos\kappa\pi - \cosh\kappa\xi\,\sin\kappa\theta}{[\cosh\kappa\xi\,\cos\kappa\pi - \sin\kappa\theta]^2 + \sinh^2\kappa\xi\,\sin^2\kappa\pi}\right.$$

$$\left. + \frac{\cos\kappa\pi + \cosh\kappa\xi\,\sin\kappa\theta}{[\cosh\kappa\xi\,\cos\kappa\pi + \sin\kappa\theta]^2 + \sinh^2\kappa\xi\,\sin^2\kappa\pi}\right] \tag{72}$$

In reference 3 the fact that the electric field goes to zero as one approaches the apex of the interior bend was used to change the range of integration of the integrals giving e_{I_r} and e_{I_θ}, thus avoiding numerical problems involved in integrating the expressions near $\tau = 1$. Using Friedlander's notation we were able to numerically integrate the appropriate functions near $\tau = 1$ and thus did not use the limiting forms of e_I as τ goes to infinity. In fact, for the exterior bend the electric field goes to infinity near the bend so that such limiting forms are not even available for the more general case.

The expressions for h_I, e_{I_r}, and e_{I_θ} were evaluated numerically and contour plots of the values of various field components within the diffracted region are attached (see figures 8-17). [Note: For all calculations the polar angle θ was used since θ is measured from one face of the wedge and is independent of any coordinate system. However for all the attached

graphs the incoming wave is assumed to be propagating along the x-axis and polar angles are listed in terms of ϕ, the angle as measured from the x-axis.]

IV. The Exterior Bend

A. Exact Expressions

To apply the solutions of the wedge problem to the diffraction by an exterior bend, we simply let the incoming pulse travel parallel to one side of the wedge; i.e. $\theta_o = \beta$ (see figure 5b). Thus

$$\cos\kappa(\theta \pm \theta_o) = -\cos\kappa\theta \tag{73}$$

since $\kappa = \pi/\beta$. Let the subscript E refer to fields for the exterior bend.

Because $\cos\kappa(\theta+\beta) = \cos\kappa(\theta-\beta)$, equation 33 reduces to

$$h_E^* = \frac{2}{\pi} \tan^{-1}\left[\frac{\sinh\kappa\xi \sin\kappa\pi}{\cosh\kappa\xi \cos\kappa\pi + \cos\kappa\theta}\right] \tag{74}$$

Note however that h_E^* goes to 2 at $r = ct$ for $\theta > \pi - \alpha$ rather than 1 as indicated in figure 5b. Why this occurs can easily be seen by considering figure 3b in the limit as the direction of propagation of the incoming wave becomes parallel to the lower edge of the wedge. When the incoming pulse direction is almost parallel to the edge, we get a reflected pulse giving a boundary condition of $h = 2$ at $r = ct$ over much of the boundary. However, when the direction of incidence is actually parallel to the edge, no reflected pulse appears, requiring $h_E = 1$ on the boundary. Simply dividing equation 74 by 2 will give us the required boundary condition without changing the fact that h_E satisfies the wave equation and the appropriate boundary conditions on the conducting surfaces of the wedge. Thus

$$h_E = \frac{h_E^*}{2} \tag{75}$$

As before, we write

$$e_{E_r} = \int_1^\tau \frac{\partial h_E}{\partial\theta}\, d\tau' + C_{1_E} \tag{76}$$

$$e_{E_\theta} = \int_o^{\xi(\tau)} \cosh\xi \, \frac{\partial h_E}{\partial \xi} \, d\xi + C_{2_E} \tag{77}$$

where now

$$C_{1_E} = \begin{cases} 0 & \text{for } 0 < \theta < \pi - \alpha \\ \sin(\theta - \pi + \alpha) & \text{for } \theta > \pi - \alpha \end{cases} \tag{78}$$

$$C_{2_E} = \begin{cases} 0 & \text{for } 0 < \theta < \pi - \alpha \\ \cos(\theta - \pi + \alpha) & \text{for } \theta > \pi - \alpha \end{cases} \tag{79}$$

$$\frac{\partial h_E}{\partial \theta} = \frac{\kappa}{\pi} \frac{\sinh\kappa\xi \, \sin\kappa\pi \, \sin\kappa\theta}{[\cosh\kappa\xi \, \cos\kappa\pi + \cos\kappa\theta]^2 + \sinh^2\kappa\xi \, \sin^2\kappa\pi} \tag{80}$$

$$\frac{\partial h_E}{\partial \xi} = \frac{\kappa}{\pi} \frac{\sin\kappa\pi[\cos\kappa\pi + \cosh\kappa\xi \, \cos\kappa\theta]}{[\cosh\kappa\xi \, \cos\kappa\pi + \cos\kappa\theta]^2 + \sinh^2\kappa\xi \, \sin^2\kappa\pi} \tag{81}$$

h_E, e_{Er}, and $e_{E\theta}$ were evaluated numerically and contour plots of the various field components are attached. Also, for the exterior case, plots of the field components versus τ are presented for various bends and angles of observation. (Such plots for the interior bend appear in SSN #47--see figures 18-35 for the exterior bend.) These graphs are useful in that they give the time domain waveforms that would be seen on an oscilloscope monitoring the fields at a given point near the bend. [Note: The field strengths on these graphs are actually plotted versus $\tau^* = \tau - \cos\phi$ where $\phi = \theta - \pi + \alpha$ (see figure 5b) since an observer at (r, ϕ) first sees the incoming pulse at $\tau^* = 0$.]

B. Special Cases

In general, the integrals in the expressions for the electric fields must be evaluated numerically. However, in the special case that the wedge angle goes to zero, i.e. the case of a perfectly conducting half-plane, we can find analytic expressions for both the electric and magnetic fields. This case is particularly interesting in that the half-plane corresponds to the edge of a ground plane or the end of an unterminated parallel plate wave guide, and the diffracted fields at the edge of the half-plane describe the effects as a pulse traveling along the ground plane or wave guide hits the edge.

When the wedge angle goes to zero

$$\kappa = \frac{1}{2} \tag{82}$$

Thus

$$\cos\kappa\pi = 0 \tag{83}$$

$$\sin\kappa\pi = 1 \tag{84}$$

and the expression for h_E simplifies to

$$h_E = \frac{1}{\pi} \tan^{-1}\left[\frac{\sinh\frac{\xi}{2}}{\cos\frac{\theta}{2}}\right] \tag{85}$$

Therefore,

$$\frac{\partial h_E}{\partial\theta} = \frac{1}{2\pi} \frac{\sinh\frac{\xi}{2}\sin\frac{\theta}{2}}{\cos^2\frac{\theta}{2} + \sinh^2\frac{\xi}{2}} \tag{86}$$

$$\frac{\partial h_E}{\partial\xi} = \frac{1}{2\pi} \frac{\cosh\frac{\xi}{2}\cos\frac{\theta}{2}}{\cos^2\frac{\theta}{2} + \sinh^2\frac{\xi}{2}} \tag{87}$$

Using equations 76 and 77 and the identities

$$\sinh\xi \equiv 2\sinh\frac{\xi}{2}\cosh\frac{\xi}{2} \tag{88}$$

$$\cosh\xi \equiv 1 + 2\sinh^2\frac{\xi}{2} \tag{89}$$

we find for $\alpha = 0$ that

$$e_{E_r} = \frac{1}{\pi} \sin \frac{\theta}{2} \int_o^{\xi(\tau)} \frac{\sinh^2 \frac{\xi}{2} \cosh \frac{\xi}{2}}{\cos^2 \frac{\theta}{2} + \sinh^2 \frac{\xi}{2}} d\xi + C_{1_E} \tag{90}$$

$$e_{E_\theta} = \frac{1}{2\pi} \cos \frac{\theta}{2} \int_o^{\xi(\tau)} \frac{\left(1+2\sinh^2 \frac{\xi}{2}\right)\cosh \frac{\xi}{2}}{\cos^2 \frac{\theta}{2} + \sinh^2 \frac{\xi}{2}} d\xi + C_{2_E} \tag{91}$$

If we make the change of variables

$$u = \sinh \frac{\xi}{2} \tag{92}$$

$$du = \frac{1}{2} \cosh \frac{\xi}{2} d\xi \tag{93}$$

equations 90 and 91 become

$$e_{E_r} = \frac{2}{\pi} \sin \frac{\theta}{2} \int_o^{u(\tau)} \frac{u^2}{\cos^2 \frac{\theta}{2} + u^2} du + C_{1_E} \tag{94}$$

$$e_{E_\theta} = \frac{1}{\pi} \cos \frac{\theta}{2} \int_o^{u(\tau)} \frac{(1+2u^2)}{\cos^2 \frac{\theta}{2} + u^2} du + C_{2_E} \tag{95}$$

The above integrals over u are easily evaluated giving

$$e_{E_R} = \frac{2}{\pi} \sin \frac{\theta}{2} \left[\sinh \frac{\xi}{2} - \cos \frac{\theta}{2} \tan^{-1} \left(\frac{\sinh \frac{\xi}{2}}{\cos \frac{\theta}{2}} \right) \right] + C_{1_E} \tag{96}$$

$$e_{E_\theta} = \frac{1}{\pi} \tan^{-1} \left(\frac{\sinh \frac{\xi}{2}}{\cos \frac{\theta}{2}} \right) + \frac{2}{\pi} \cos \frac{\theta}{2} \left[\sinh \frac{\xi}{2} - \cos \frac{\theta}{2} \tan^{-1} \left(\frac{\sinh \frac{\xi}{2}}{\cos \frac{\theta}{2}} \right) \right] + C_{2_E} \tag{97}$$

where in both equations 96 and 97 the arctangent is evaluated between $-\pi/2$ and $\pi/2$.

C. Early-Time Diffracted Fields

Although it is not readily apparent how to find analytic expressions for the electric field integrals for an arbitrary bend angle, one can find certain asymptotic expressions for the fields for certain ranges of τ.

The early-time diffracted fields are described in the region just inside the diffraction boundary at $\tau = 1$. As τ approaches 1,

$$\xi \equiv \cosh^{-1}\tau \simeq [2(\tau-1)]^{1/2} \tag{98}$$

Since ξ goes to zero as τ approaches 1,

$$\cosh\kappa\xi = 1 + \frac{\kappa^2\xi^2}{2} + O(\xi^4) \tag{99}$$

$$\sinh\kappa\xi = \kappa\xi + O(\xi^3) \tag{100}$$

$$\tau = 1 + \frac{\xi^2}{2} + O(\xi^4) \tag{101}$$

and

$$\sqrt{\tau^2 - 1} \simeq \sqrt{2(\tau-1)} = \xi + O(\xi^2) \tag{102}$$

Therefore, using these approximations near $\tau = 1$, one can write from Equations 75, 76, and 77

$$h_E \simeq \frac{1}{\pi}\tan^{-1}\left[\frac{\kappa\xi\,\sin\kappa\pi}{\cos\kappa\pi + \cos\kappa\theta + \frac{\kappa^2\xi^2}{2}\cos\kappa\pi}\right] + O(\xi^3)$$

$$\simeq \frac{1}{\pi}\frac{\kappa\xi\,\sin\kappa\pi}{\cos\kappa\pi + \cos\kappa\theta + \frac{\kappa^2\xi^2}{2}\cos\kappa\pi} + O(\xi^3) \tag{103}$$

$$\frac{\partial e_{E_\theta}}{\partial \tau} = \frac{\tau}{\sqrt{\tau^2 - 1}} \frac{\partial h_E}{\partial \xi} \simeq \frac{\kappa}{\pi} \sin\kappa\pi \frac{\left[1 + \frac{\xi^2}{2}\right]}{\xi}$$

$$\cdot \left\{ \frac{\cos\kappa\pi + \cos\kappa\theta + \frac{\kappa^2\xi^2}{2} \cos\kappa\theta}{[\cos\kappa\pi + \cos\kappa\theta]^2 + \kappa^2\xi^2[1 + \cos\kappa\pi \cos\kappa\theta]} \right\} + O(\xi^4) \qquad (104)$$

$$\frac{\partial e_{E_r}}{\partial \tau} = \frac{\partial h_E}{\partial \theta} \simeq \frac{\kappa}{\pi} \sin\kappa\pi \left\{ \frac{\kappa\xi \sin\kappa\theta}{[\cos\kappa\pi + \cos\kappa\theta]^2 + \kappa^2\xi^2[1 + \cos\kappa\pi\cos\kappa\theta]} \right\} + O(\xi^3) \qquad (105)$$

Since in the region near $\tau = 1$

$$d\tau \simeq \xi d\xi \qquad (106)$$

one can analytically integrate equations 104 and 105 giving

$$e_{E_\theta} = C_3\xi + C_4 \tan^{-1}\left(\frac{\xi}{C_5}\right) + C_{2_E} + O(\xi^3) \qquad (107)$$

$$e_{E_r} = C_6\xi + C_7 \tan^{-1}\left(\frac{\xi}{C_5}\right) + C_{1_E} + O(\xi^4) \qquad (108)$$

where C_{1_E} and C_{2_E} are defined in equations 78 and 79

$$C_3 = \frac{\sin\kappa\pi}{2\kappa\pi} \frac{[\cos\kappa\pi + \cos\kappa\theta + \kappa^2 \cos\kappa\theta]}{1 + \cos\kappa\pi \cos\kappa\theta} \qquad (109)$$

$$C_4 = -C_3C_5 + \frac{\sin\kappa\pi}{\pi[1 + \cos\kappa\pi \cos\kappa\theta]^{1/2}} \qquad (110)$$

$$C_5 = \frac{\cos\kappa\pi + \cos\kappa\theta}{\kappa[1 + \cos\kappa\pi \cos\kappa\theta]^{1/2}} \qquad (111)$$

$$C_6 = \frac{\sin\kappa\pi \sin\kappa\theta}{\pi[1+\cos\kappa\pi \cos\kappa\theta]} \tag{112}$$

$$C_7 = -C_6C_5 \tag{113}$$

where the arctangent term in equations 107 and 108 is evaluated in the range between $-\pi/2$ and $\pi/2$.

Since ξ is small the $\tan^{-1}(\xi/C_5)$ term in both equations 107 and 108 can be approximated by the first few terms of its series expansion, provided C_5 is not also near zero. In this case, we just get

$$e_{E_\theta} = C_3\xi + C_4\left(\frac{\xi}{C_5}\right) + C_{2_E} + O(\xi^3)$$

$$\simeq \frac{\kappa \sin\kappa\pi}{\pi[\cos\kappa\pi+\cos\kappa\theta]} \sqrt{2(\tau-1)} + C_{2_E} \tag{114}$$

$$e_{E_r} = C_6\xi + C_7\left(\frac{\xi}{C_5}\right) - \frac{C_7}{3}\left(\frac{\xi}{C_5}\right)^3 + C_{1_E} + O(\xi^4)$$

$$\simeq \frac{C_6}{3C_5^2}[2(\tau-1)]^{3/2} + C_{1_E} \tag{115}$$

Note that when we expand the arctangent in this way, the θ-component of $\vec{e}_E$ just varies as the first power of ξ; i.e. a $\sqrt{\tau - 1}$. The r-component on the other hand varies as ξ^3 since the first power terms cancel.

Now consider what happens when C_5 is small. From equation 111 C_5 goes to zero as θ approaches $\pi - \alpha$. This is just the value of θ which marks the boundary of the shadow region, and when we are actually on the boundary $\tau = 1$ at $\theta = \pi - \alpha$ we are at the point where we get a discontinuous change in the field magnitudes from zero to one. If we consider the actual limits as $\tau \to 1$ we see that

$$\lim_{\tau\to 1} e_{E_\theta} = C_{2_E} = \begin{cases} 0 & \text{for } 0 < \theta < \pi - \alpha \\ \cos(\theta-\pi+\alpha) & \text{for } \theta > \pi - \alpha \end{cases} \tag{116}$$

$$\lim_{\tau \to 1} e_{E_r} = C_{1_E} = \begin{cases} 0 & \text{for } 0 < \theta < \pi - \alpha \\ \sin(\theta - \pi - \alpha) & \text{for } \theta > \pi - \alpha \end{cases} \tag{117}$$

except when $\theta = \pi - \alpha$ (i.e. $C_5 = 0$). As C_5 approaches zero, we can write

$$\lim_{C_5 \to 0^-} \tan^{-1}\left(\frac{\xi}{C_3}\right) = -\frac{\pi}{2} \qquad \theta > \pi - \alpha \tag{118}$$

$$\lim_{C_5 \to 0^+} \tan^{-1}\left(\frac{\xi}{C_3}\right) = \frac{\pi}{2} \qquad \theta < \pi - \alpha \tag{119}$$

From equation 108 it is easily seen that e_{E_r} goes to zero as we approach $\theta = \pi - \alpha$ from either side along the circle $\tau = 1$. The case for e_{E_θ} is slightly different since $C2_E$ is not continuous across the line $\theta = \pi - \alpha$ and C_4 does not go to zero there. Upon considering C_4 it can be seen that

$$\lim_{\theta \to \pi - \alpha} C_4 = \frac{1}{\pi} \tag{120}$$

Thus

$$\lim_{\substack{\tau \to 1^+ \\ \theta \to \pi - \alpha}} e_{E_\theta} = \begin{cases} C_{2_E} + \frac{1}{2} & \text{for } \theta < \pi - \alpha \\ C_{2_E} - \frac{1}{2} & \text{for } \theta > \pi - \alpha \end{cases} \tag{121}$$

and since

$$C_{2_E} = \begin{cases} 0 & \text{for } \theta < \pi - \alpha \\ \cos(\theta - \pi + \alpha) & \text{for } \theta > \pi - \alpha \end{cases} \tag{122}$$

e_{E_θ} goes to the limit of 1/2 as we approach the limit from either side of the line $\theta = \pi - \alpha$; i.e. along the line e_{E_θ} goes to a value half way in between the values at $\tau = 1$ slightly

away from the boundary of the shadow region. Thus, along $\theta = \pi - \alpha$ equations 107 and 108 reduce to

$$e_{E_\theta} = -\frac{\kappa}{\pi}\frac{\cos\kappa\pi}{\sin\kappa\pi}[2(\tau-1)]^{1/2} + \frac{1}{2} + O(\xi^3) \tag{123}$$

$$e_{E_r} = \frac{1}{\pi}[2(\tau-1)]^{1/2} + O(\xi^4) \tag{124}$$

Figure 6 shows a plot comparing equations 114, 115, 123, and 124 to the numeric solutions for $\alpha = \pi/2$. The rate of convergence shown in this figure is typical of that of other wedge angles α. As expected, the expressions in equations 114 and 115 converge rather slowly to the numeric solutions when θ is near $\pi - \alpha$.

D. Late-Time Diffracted Fields

For late times the diffracted fields approach the static limit. Thus, since late times correspond to large τ (i.e. the region near the bend), the electric field will go to infinity as one approaches the apex of the interior bend. We are interested in obtaining an approximate expression for how both $\vec{e}_F$ and $\vec{h}_E$ vary in the region near the bend.

Now, for large τ,

$$\xi = \cosh^{-1}\tau \simeq \log(2\tau) + O(\tau^{-2}) \tag{125}$$

Thus

$$\sinh\kappa\xi \simeq \frac{1}{2}[\exp(\kappa \log 2\tau) - \exp(-\kappa \log 2\tau)] \tag{126}$$

$$\cosh\kappa\xi \simeq \frac{1}{2}[\exp(\kappa \log 2\tau) + \exp(-\kappa \log 2\tau)] \tag{127}$$

Since $1/2 \leq \kappa \leq 1$ and $\kappa \log(2\tau) = \log[(2\tau)^\kappa]$

$$\sinh\kappa\xi \simeq \cosh\kappa\xi \simeq 2^{\kappa-1}\tau^\kappa \simeq \frac{1}{2}e^{\kappa\xi} \tag{128}$$

Thus, from equation 75, for large τ

$$h_E \simeq \frac{1}{\pi} \tan^{-1}\left[\frac{\sin\kappa\pi}{\cos\kappa\pi}\right]$$

$$= \kappa = \frac{\pi}{2\pi - \alpha} \tag{129}$$

Note that this is just half the large τ limit on h_I as derived in SSN #47. This factor of two difference occurs because we normalized the h_E field in equation 75. However, h_E for large τ still goes to the expected limit of 1 as α approaches π (i.e. limit of no bend in plane).

To find large τ asymptotic forms for e_{E_r} and e_{E_θ} one must find a way to approximate the integrals in equations 76 and 77. First consider e_{E_r}. Equation 76 can be rewritten as

$$e_{E_r}(\tau) - e_{E_r}(0) = \int_1^\tau \frac{\partial h_E}{\partial \theta} d\tau'$$

$$= \int_o^{\xi(\tau)} \sinh\xi f_r(\xi) d\xi' = I_r \tag{130}$$

where $f_r(\xi) = \partial h_E/\partial\theta$. Now the integral I_r can be written as an infinite series by continually integrating by parts. One obtains

$$I_r = f_r(\xi)\cosh\xi - \frac{\partial f_r(\xi)}{\partial\xi}\sinh\xi + \frac{\partial^2 f_r(\xi)}{\partial\xi^2}\cosh\xi$$

$$- \frac{\partial^3 f_r(\xi)}{\partial\xi^3}\sinh\xi + \ldots \tag{131}$$

For large τ

$$f_r(\xi) = \frac{\partial h_E}{\partial\theta} \simeq \frac{\kappa}{\pi}\frac{\sin\kappa\pi\,\sin\kappa\theta}{\frac{1}{2}e^{\kappa\xi}} + O(e^{-2\kappa\xi}) \tag{132}$$

Thus

$$\frac{\partial^n f_r(\xi)}{\partial \xi^n} \simeq (-\kappa)^n f_r(\xi) \tag{133}$$

and the series for I_r becomes

$$I_r \simeq f_r(\xi)\left[\frac{1}{2}\, e^{\xi}\right]\sum_{n=0}^{\infty}\kappa^n \tag{134}$$

But since $\kappa < 1$ we have a simple geometric series which can be summed.

$$\sum_{n=0}^{\infty}\kappa^n = \frac{1}{1-\kappa} \tag{135}$$

Thus

$$I_r \simeq \left(\frac{1}{1-\kappa}\right)\frac{\kappa}{\pi}\,\sin\kappa\pi\,\sin\kappa\theta\; e^{(1-\kappa)\xi} + O(e^{(1-2\kappa)\xi})$$

$$= \frac{1}{1-\kappa}\,\frac{\kappa}{\pi}\,\sin\kappa\pi\,\sin\kappa\theta\,(2\tau)^{1-\kappa} + O(\tau^{1-2\kappa}) \tag{136}$$

One can similarly expand

$$I_\theta = \int_o^{\xi} \cosh\xi\,\frac{\partial h_E}{\partial \xi}\, d\xi \tag{137}$$

and obtain for large τ

$$I_\theta \simeq \frac{1}{1-\kappa}\cdot\frac{\kappa}{\pi}\,\sin\kappa\pi\,\cos\kappa\theta\,(2\tau)^{1-\kappa} + O(\tau^{1-2\kappa}) \tag{138}$$

Thus it can be seen that eE_r and eE_θ just vary as $\tau^{1-\kappa}$ as τ becomes large. Since $\kappa < 1$

$$\lim_{\tau\to\infty} e_{E_r} = \lim_{\tau\to\infty} e_{E_\theta} = \pm\infty \tag{139}$$

Note that

$$e_{E_r},\ e_{E_\theta} \propto r^{(\alpha-\pi)/2\pi-\alpha)} = r^{\kappa-1} \tag{140}$$

If one considers the more general problem of diffraction at any sharp edge, a set of edge conditions describing the field variation as one approaches the edge can be derived from energy conservation considerations. Jones[4] has derived such edge conditions and they match the variation with r given above.

Although equations 136 and 138 describe the behavior of the electric field for large ξ, the actual values of e_{Er} and $e_{E\theta}$ approach these limits very slowly with increasing τ due to the logarithmic dependence of ξ on τ (see equation 125). To obtain an asymptotic expression that approximates the desired integrals more closely it is necessary to obtain another term in the asymptotic series describing the integrals. One way of finding such terms is to consider the integral of the difference between the actual integrand and the large τ approximations; i.e. write

$$I_r = \int_o^\xi \sinh\xi'\ f_r(\xi')d\xi'$$

$$= \int_o^\xi \left[\sinh\xi'\ f_r(\xi') - \frac{\kappa}{\pi}\sin\kappa\pi\ \sin\kappa\theta\ e^{(1-\kappa)\xi'}\right]d\xi'$$

$$+\int_o^\xi \frac{\kappa}{\pi}\sin\kappa\pi\ \sin\kappa\theta\ e^{(1-\kappa)\xi'}d\xi' = I_{r_1} + I_{r_o} \tag{141}$$

The second integral is just equal to the expression in equation 136. Since the first integral must go to zero as ξ becomes large, it can be written as

$$I_{r_1} = -\int_\xi^\infty \left[\sinh\xi'\ f_r(\xi') - \frac{\kappa}{\pi}\sin\kappa\pi\ \sin\kappa\theta\ e^{(1-\kappa)\xi'}\right]d\xi' \tag{142}$$

Here we use the large τ approximation

$$f_r(\xi) = \frac{\partial h_E}{\partial \theta} \simeq \frac{\kappa}{\pi} \frac{\frac{1}{2} e^{\kappa\xi} \sin\kappa\pi \sin\kappa\theta}{\left(\frac{1}{2} e^{\kappa\xi}\right)^2 + 2\left(\frac{1}{2} e^{\kappa\xi}\right) \cos\kappa\pi \cos\kappa\theta} \qquad (143)$$

Upon substitution into equation 142 and simplification by dropping certain unimportant terms, one gets

$$I_{r_1} \simeq -\frac{2\kappa \sin\kappa\pi \sin\kappa\theta}{\pi(1-2\kappa)} \cos\kappa\pi \cos\kappa\theta \, e^{\xi(1-2\kappa)} + O(e^{\xi(1-3\kappa)}) \qquad (144)$$

Similarly, the first order correction to the integral giving $e_{E\theta}$ is for large τ

$$I_{\theta_1} \simeq -\frac{2\kappa \sin\kappa\pi}{\pi(1-2\kappa)}(\cos\kappa\pi+\cos\kappa\theta)\cos\kappa\pi \cos\kappa\theta \, e^{\xi(1-2\kappa)} + O(e^{\xi(1-3\kappa)}) \qquad (145)$$

However, even including these first order corrections, the asymptotic forms do not approach the numerical calculation of the integral very rapidly. A graph showing both the asymptotic approximations and the results of numerical integration is attached (see figure 7). This graph is plotted for a wedge angle of $\alpha = \pi/2$ and gives a fairly representative idea of the rate of convergence of the above asymptotic forms for large τ. It is apparent however that higher order terms in equations 144 and 145 are dependent on κ; since κ goes to 1 as the wedge angle approaches π (no bend) the above expressions converge faster for small bends.

V. Results

The results of this note are primarily contained in the attached contour plots of the various diffracted field components in the region around the bend. However, a few of the general characteristics of these contour plots can easily be summarized.

For the interior bend, refer to figures 8-17 of this note and to SSN #47. It is easily seen that the magnitude of h_I is enhanced everywhere in the diffracted region with the greatest values occurring in the reflection zone of geometrical optics (i.e. in the region $\phi_o \leq \phi \leq 2\phi_o$). And in this reflected zone,

h_I increases to the limiting value of $h_I = 2$ at the outer boundary of the diffraction region (i.e. at $\tau = 1$). It is also obvious that the magnetic field becomes larger everywhere in the diffracted region as the bend angle ϕ_o increases.

The total magnitude of the electric field behaves quite differently. $e_{I_{total}}$ is generally less than 1 for negative x, while $e_{I_{total}}$ is enhanced for positive x, particularly in the reflected zone $\phi_o \leq \phi \leq 2\phi_o$. $e_{I_{total}}$ becomes smaller as one approaches the apex of the bend (actually goes to the limit of zero) and the contours approach circular arcs near the apex. This is expected since the fields go to the static limit in this area. At the edge of the diffracted region, $e_{I_{total}}$ has the limits

$$\lim_{\tau \to 1^+} e_{I_{total}} = \begin{cases} 1 & \text{for } 2\phi_o < \phi < \pi \\ 2\cos\phi_o & \text{for } \phi_o < \phi < 2\phi_o \end{cases} \tag{146}$$

Thus the largest electric fields occur just inside the diffracted region boundary when $\phi_o < \phi < 2\phi_o$.

The x-component of the diffracted electric field is by itself a good measure of the amount of diffraction since the incident electric field has no x-component. Also note that e_{I_x} is negative everywhere in the diffracted region.

For small bends, e_{I_y} is almost the same as the total electric field since e_{I_x} is very small for slight bends. As the bend angle increases, e_{I_y} becomes less than 1 over an increasing area of the diffracted region. In fact, for $\phi_o \geq \pi/4$, e_{I_y} is less than 1 everywhere in the diffracted region.

One should also note that e_{I_x} and e_{I_y} have the following limits at the boundary $\tau = 1$

$$\lim_{\tau \to 1^+} e_{I_x} = \begin{cases} -\sin 2\phi_o & \text{for } \phi_o < \phi < 2\phi_o \\ 0 & \text{for } 2\phi_o < \phi < \pi \end{cases} \tag{147}$$

$$\lim_{\tau \to 1^+} e_{I_y} = \begin{cases} 1 + \cos 2\phi_o & \text{for } \phi_o < \phi < 2\phi_o \\ 1 & \text{for } 2\phi_o < \phi < \pi \end{cases} \tag{148}$$

Now consider the exterior bend. (See figures 18-35. Included in these figures are both contour plots and graphs of the fields as a function of time. Remember that the contour

plots describe the fields as a function of position at a given time while the graphs give the fields at a given point as a function of time.)

For the exterior bend, the magnetic field is less than the incident magnetic field everywhere inside the diffracted region. Why this is true can be seen intuitively from the fact that the diffracted fields fill a larger volume of space than the incident field would if there were no diffraction. The smallest values of h_E occur near $\tau = 1$ for $\phi < 0$ since h_E goes to the limit 0 as τ approaches 1 in the shadow region.

Now consider the diffracted electric field for the exterior bend. The magnitude of the total electric field goes to infinity at the apex of the exterior bend, rather than zero as it did for the interior case; and $e_{E_{total}}$ is greater than 1 in the upper left hand portion of the diffracted region and less than 1 elsewhere. These results are essentially opposite those observed for $e_{I_{total}}$.

The x-component of the electric field is again a measure of the amount of diffraction since the incident electric field has no x-component. Thus e_{E_x} is greatest in the shadow region, but now it has its largest magnitude near the bend rather than at the outer edge of the diffracted region as was the case for e_{I_x}.

e_{E_y} is very similar to $e_{E_{total}}$ in the upper left hand part of the diffracted region and it gradually becomes smaller as one rotates around toward the shadow region where e_{E_x} becomes more important in determining the total electric field.

The special case of diffraction at the edge of a conducting half-plane (i.e. $\alpha = 0$) is particularly interesting with respect to the symmetry of the contour lines (see figures 33 and 34). The symmetry results from the fact that the incoming wave is propagating parallel to the symmetry plane of the wedge.

Thus it can be seen that the interior and exterior bends are similar in that the diffraction effects become larger as the bends vary more from the flat plate, and both cases approach the limit of no diffraction for a planar conducting sheet. However the regions of largest fields within the diffracted area occur in essentially opposite areas for the internal and external bends.

VI. Summary

We have calculated the diffracted field around exterior and interior bends in a planar conducting sheet using an incoming step-function pulse traveling parallel to one edge of the conducting plate. For a TEM type incoming pulse, $\vec{H}$ was found

by solving the scalar wave equations, and $\vec{E}$ determined from $\vec{H}$ by use of one of Maxwell's equations. Since the interior bend case was discussed in SSN #47, the exterior bend was studied in more detail here, with contour plots of the field strengths in the neighborhood of the bend being calculated for both cases. The application of these results to bends in a parallel-plate wave guide is obvious, a special case of interest being the limiting case of a half-plane; i.e. an unterminated wave guide.

References

1. J. B. Keller and A. Blank, "Diffraction and Reflection of Pulses by Wedges and Corners," Comm. on Pure and Applied Math., vol. 4, p. 75, 1951.

2. F. G. Friedlander, Sound Pulses, Cambridge University Press, Cambridge, 1958.

3. Carl E. Baum, Sensor and Simulation Note 47, "The Diffraction of an Electromagnetic Plane Wave at a Bend in a Perfectly Conducting Planar Sheet," August 1967.

4. D. S. Jones, The Theory of Electromagnetism, Macmillan Company, New York, 1964.

		CONTOURS				WAVEFORMS		
		h	e_{total}	e_x	e_y	h	e_x	e_y
INTERIOR BEND	$\frac{\phi_0}{\pi} = 0.025$	8-A	8-B	9-A	9-B	3-A (SSN47)	3-B (SSN47)	3-C (SSN47)
	0.05	10-A	10-B	11-B	11-B	4-A (SSN47)	4-B (SSN47)	4-C (SSN47)
	0.1	12-A	12-B	13-A	13-B	5-A (SSN47)	5-B (SSN47)	5-C (SSN47)
	0.15	14-A	14-B	15-A	15-B	6-A (SSN47)	6-B (SSN47)	6-C (SSN47)
	0.25	16-A	16-B	17-A	17-B	7-A (SSN47)	7-B (SSN47)	7-C (SSN47)
EXTERIOR BEND	$\frac{\alpha}{\pi} = 0.95$	18-A	18-B	19-A	19-B	20-A	20-B	20-C
	0.9	21-A	21-B	22-A	22-B	23-A	23-B	23-C
	0.75	24-A	24-B	25-A	25-B	26-A	26-B	26-C
	0.5	27-A	27-B	28-A	28-B	29-A	29-B	29-C
	0.25	30-A	30-B	31-A	31-B	32-A	32-B	32-C
	0	33-A	33-B	34-A	34-B	35-A	35-B	35-C

TABLE OF CONTENTS OF CONTOUR PLOTS AND WAVEFORMS

EXAMPLE: THE CONTOUR PLOT OF e_x FOR THE EXTERIOR BEND $\frac{\alpha}{\pi} = 0.75$

OCCURS IN FIGURE 25-A

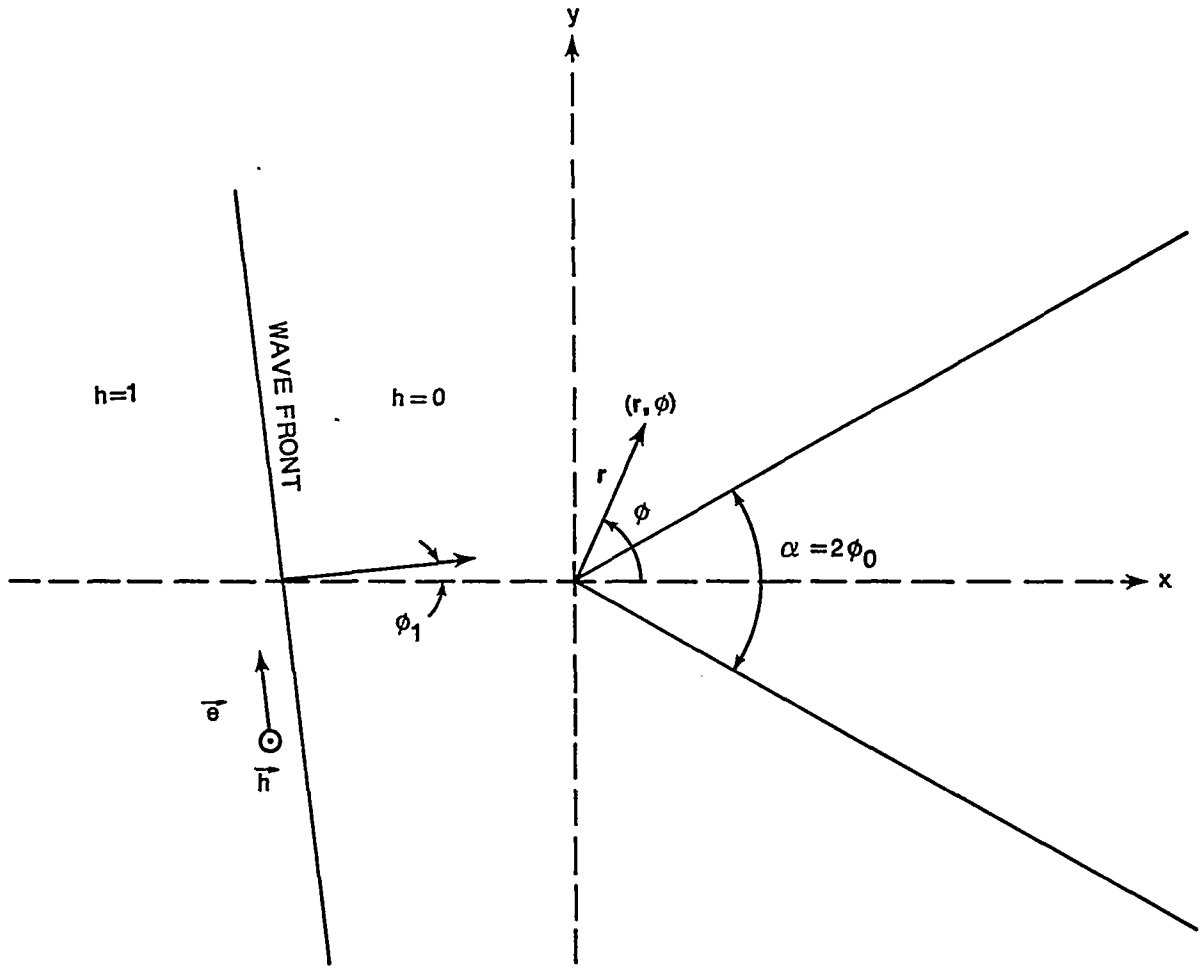

FIGURE 1. DIFFRACTION OF A STEP-FUNCTION WAVE AT A PERFECTLY CONDUCTING WEDGE: BEFORE WAVE INCIDENCE ($t<0$)

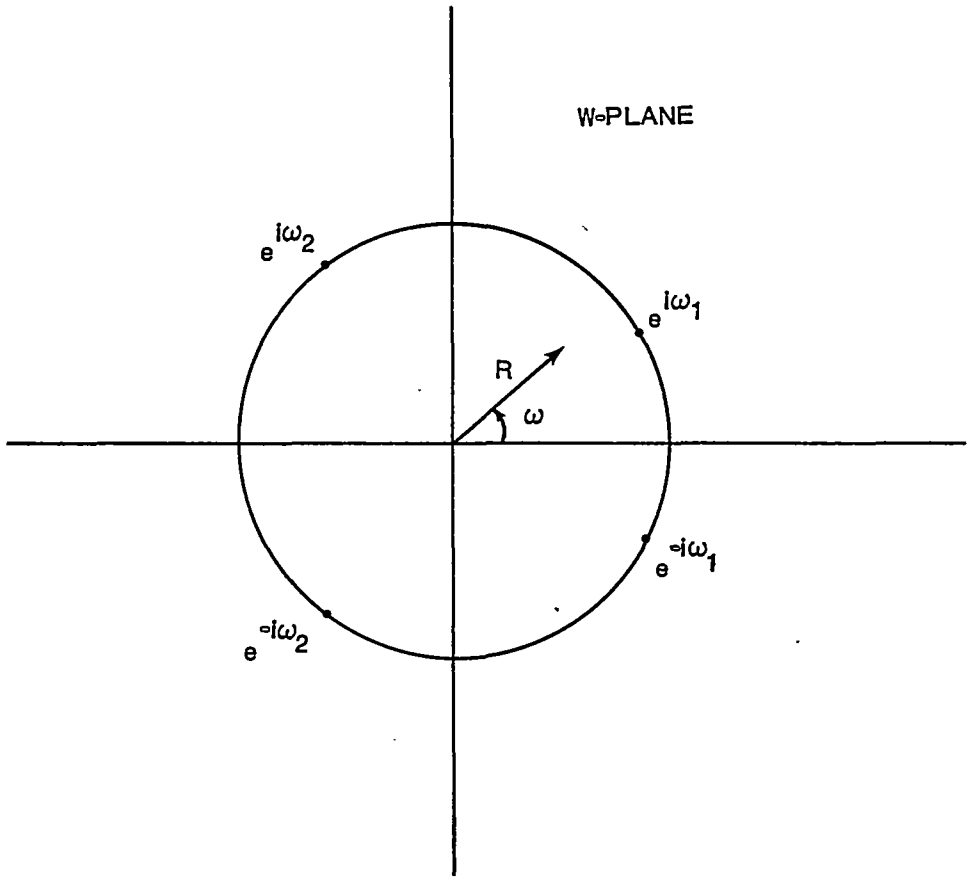

$$W = R_e{}^{i\omega} = \left(e^{-i\phi_o} \rho e^{i\phi}\right)$$

FIGURE 2. COMPLEX W-PLANE WHERE EDGES OF CONDUCTING WEDGE ARE MAPPED ONTO REAL AXIS.

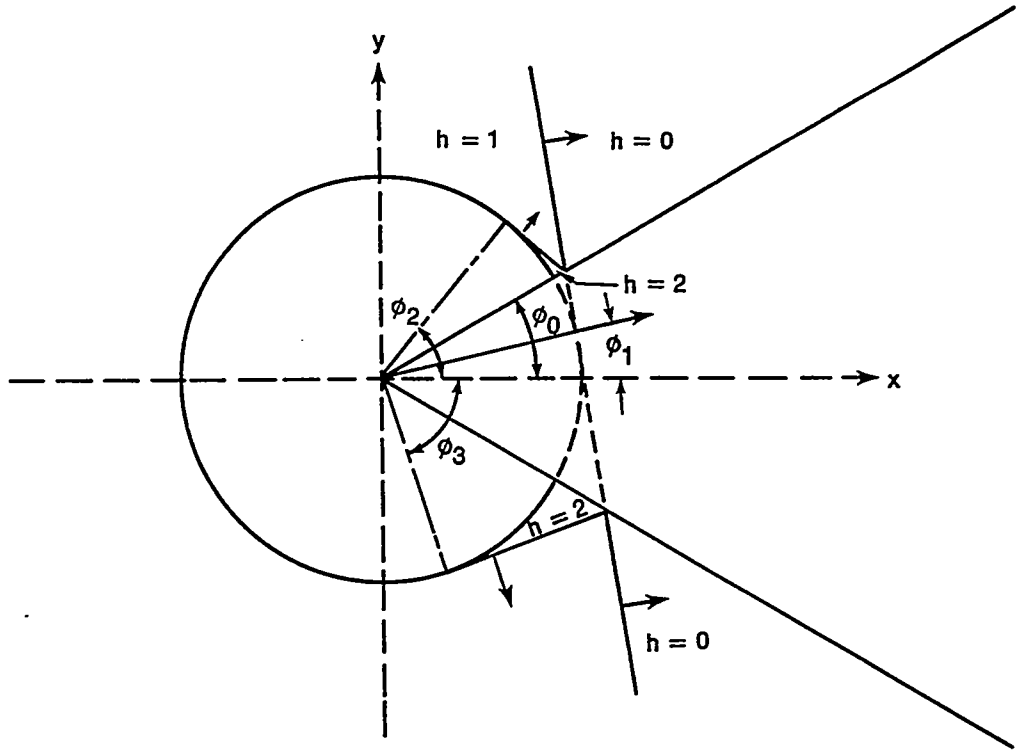

A. $0 \leq \phi_1 \leq \phi_0$

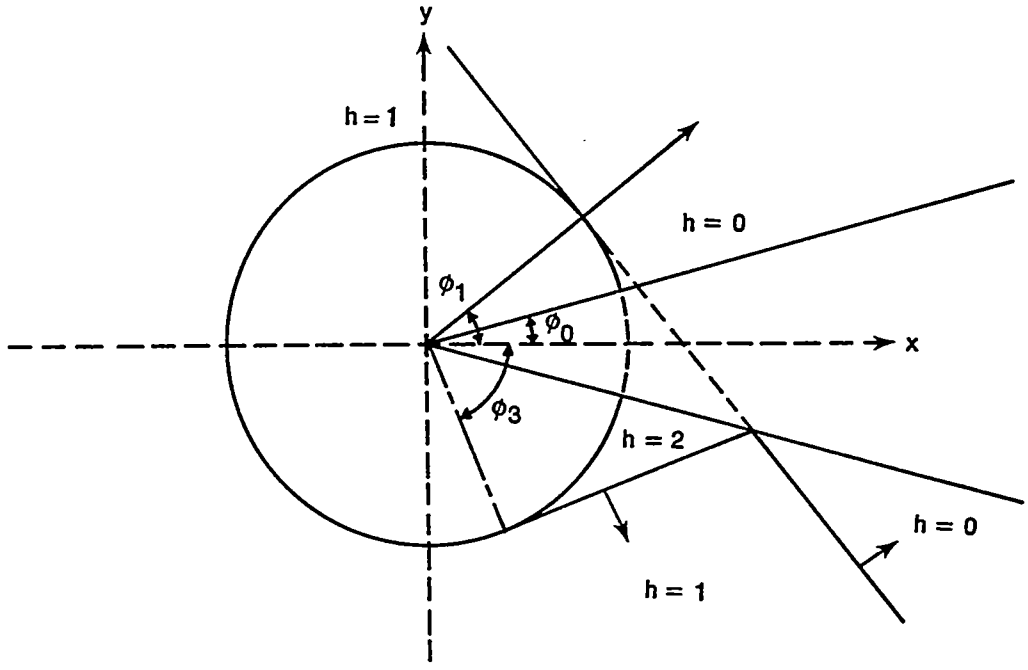

B. $\phi_1 > \phi_0$

FIGURE 3. DIFFRACTION OF A STEP-FUNCTION WAVE AT A PERFECTLY CONDUCTING WEDGE: AFTER WAVE INCIDENCE (t > 0)

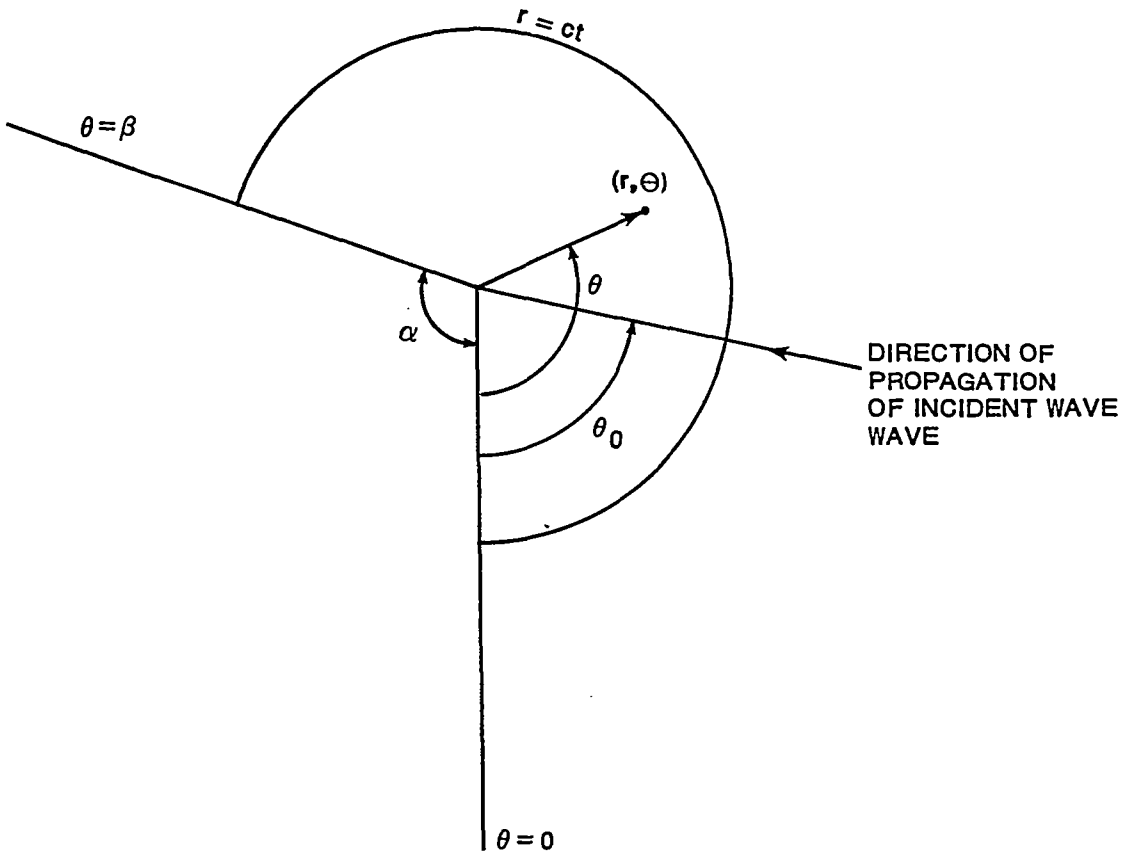

FIGURE 4. DIFFRACTION OF A STEP-FUNCTION WAVE BY A PERFECTLY CONDUCTING WEDGE: FRIEDLANDER GEOMETRY

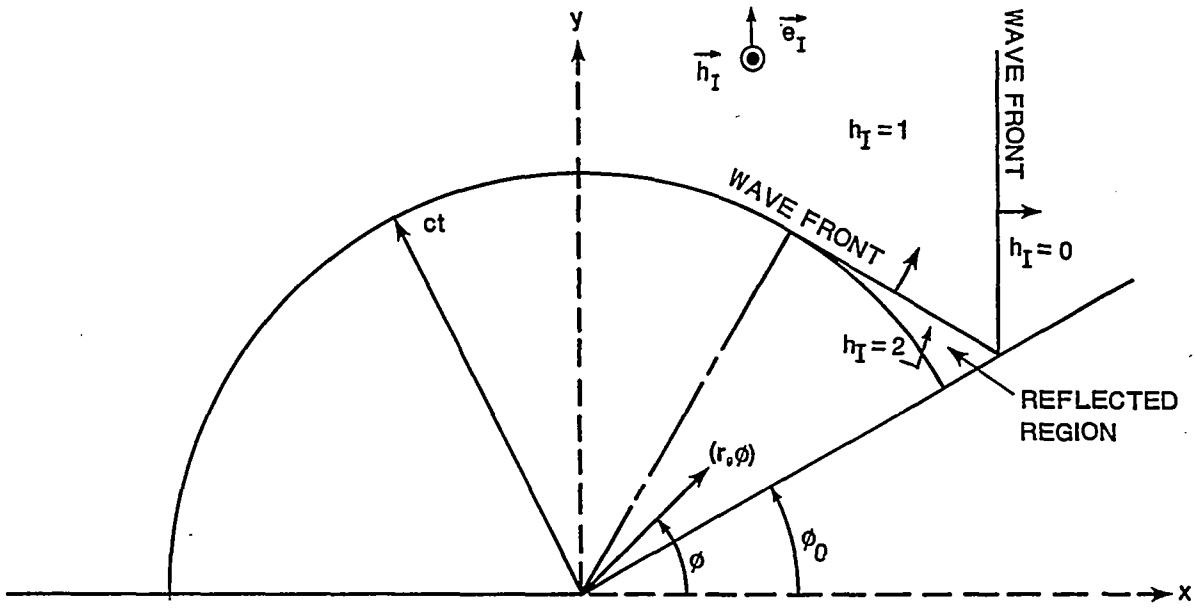

A. INTERIOR BEND

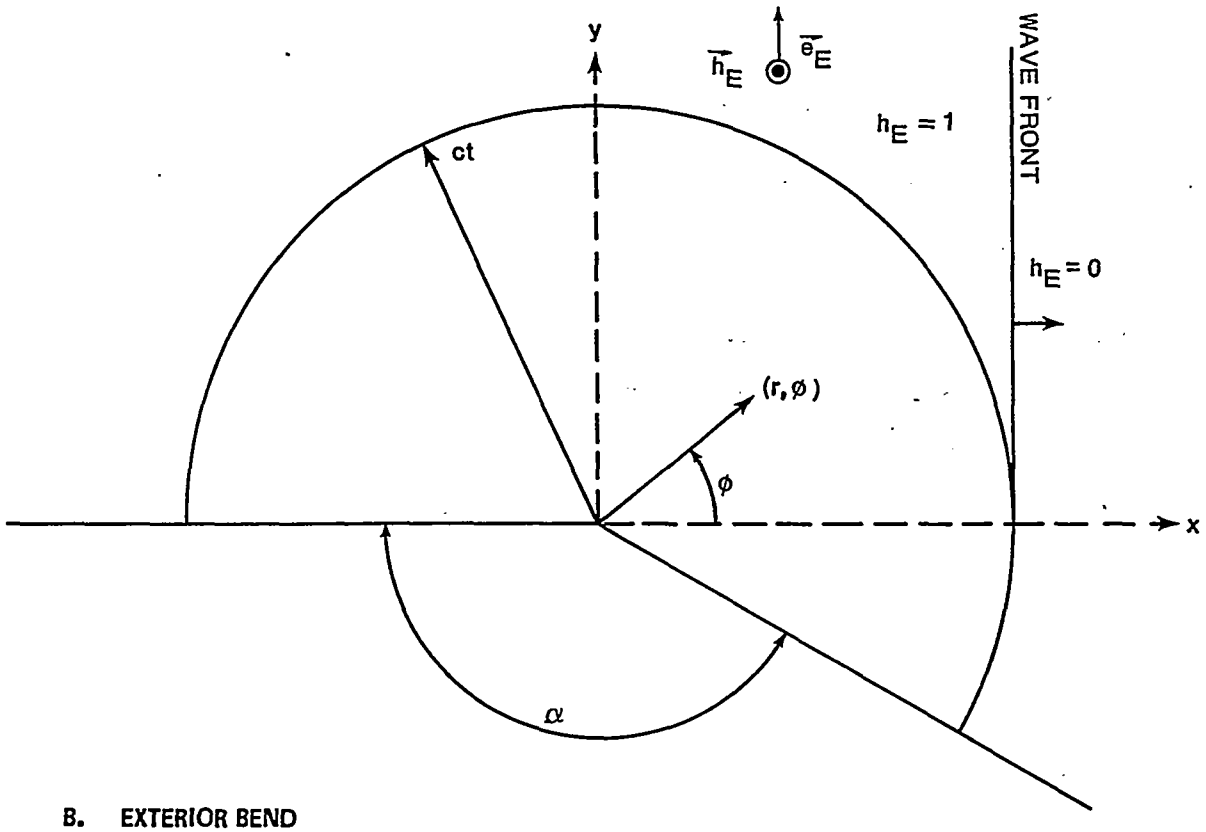

B. EXTERIOR BEND

FIGURE 5. DIFFRACTION OF AN INCIDENT STEP-FUNCTION WAVE BY INTERIOR AND EXTERIOR BENDS IN A PERFECTLY CONDUCTING SHEET.

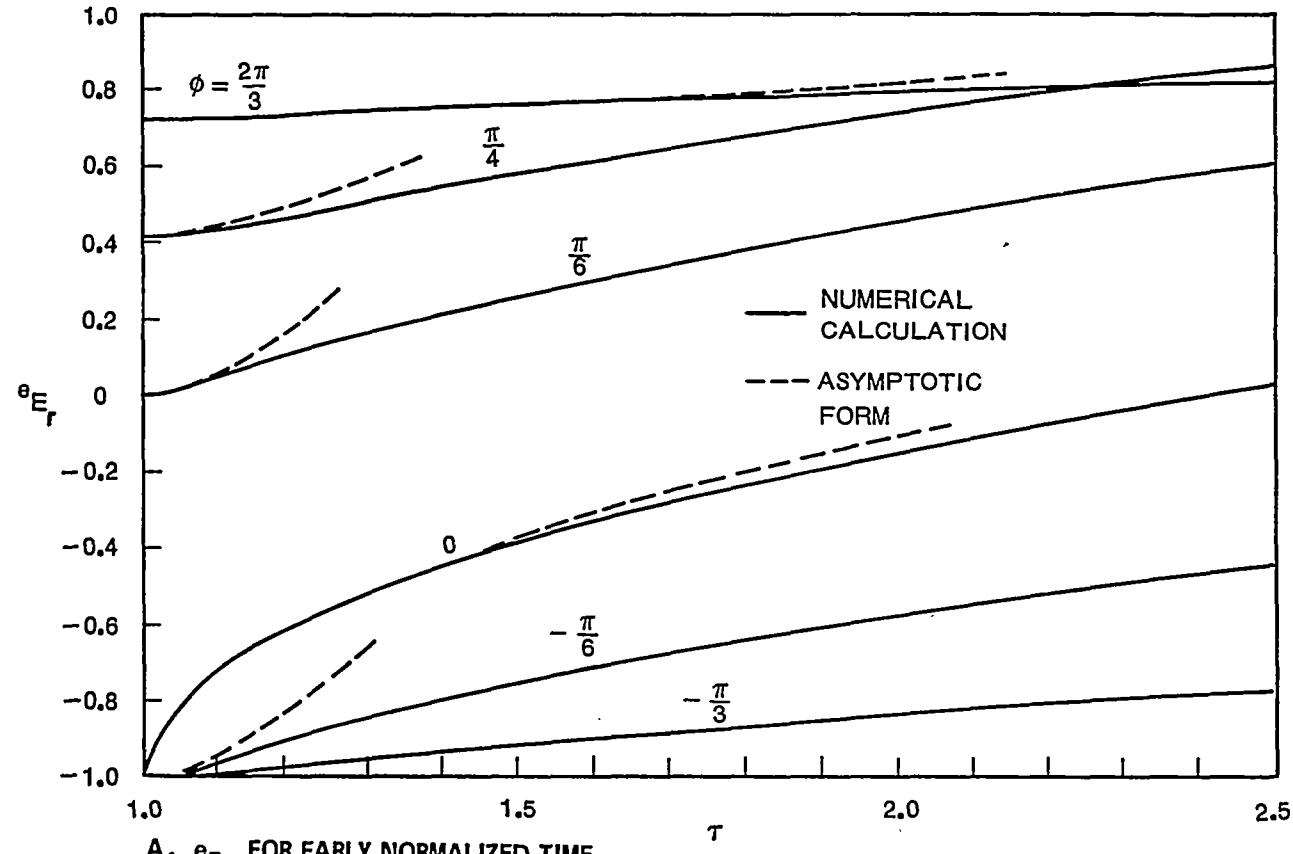

A. e_{E_r} FOR EARLY NORMALIZED TIME

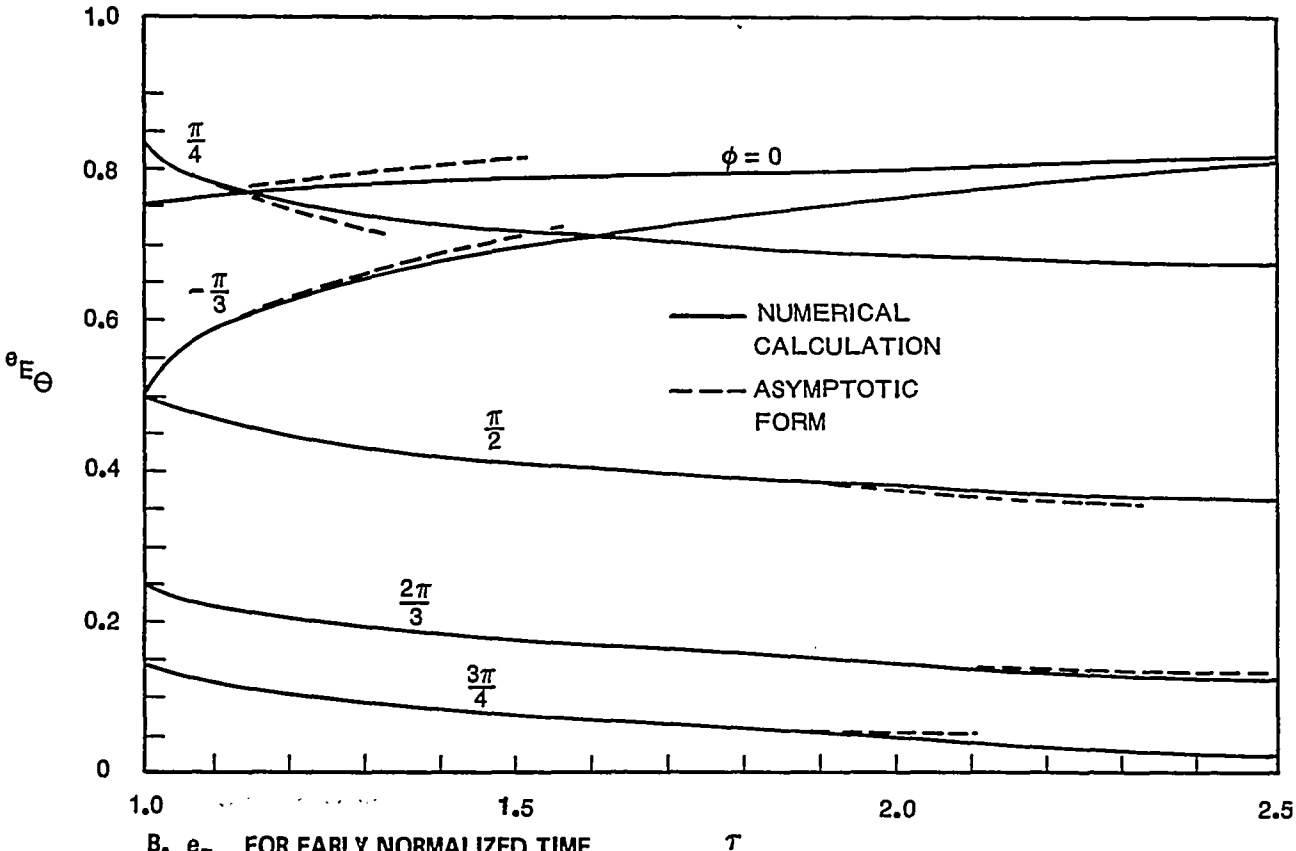

B. e_{E_θ} FOR EARLY NORMALIZED TIME

FIGURE 6. NORMALIZED ELECTRIC FIELDS FOR EARLY TIMES WITH $\alpha = \frac{\pi}{2}$

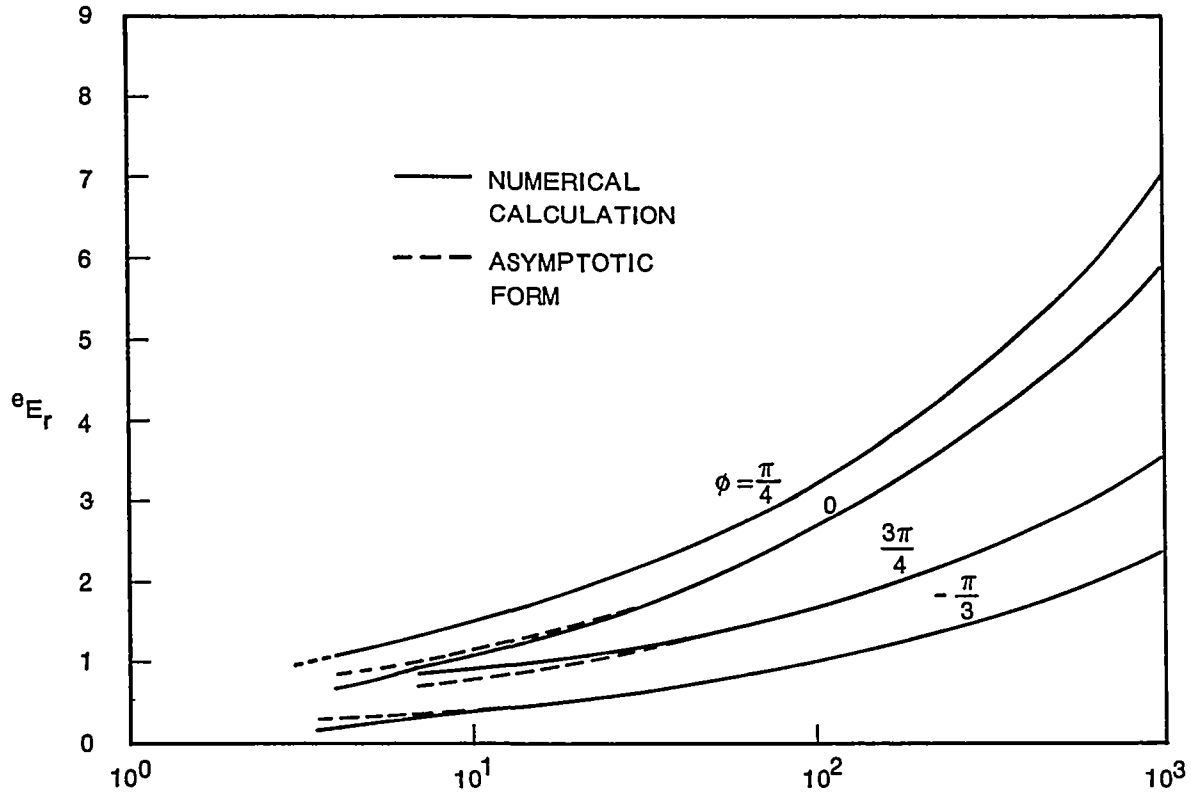

A. e_{E_r} FOR LATE NORMALIZED TIME

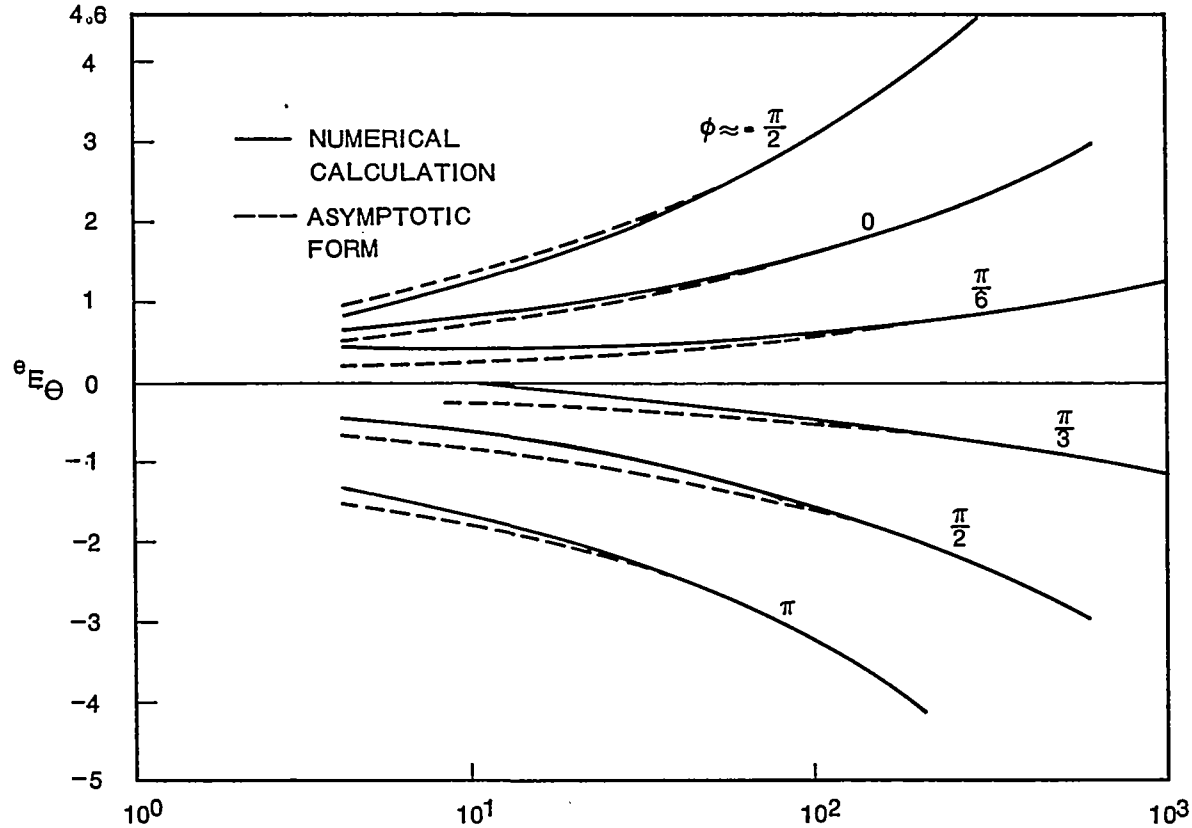

B. e_{E_θ} FOR LATE NORMALIZED TIME

FIGURE 7. NORMALIZED ELECTRIC FIELDS FOR LATE TIMES WITH $\alpha = \frac{\pi}{2}$

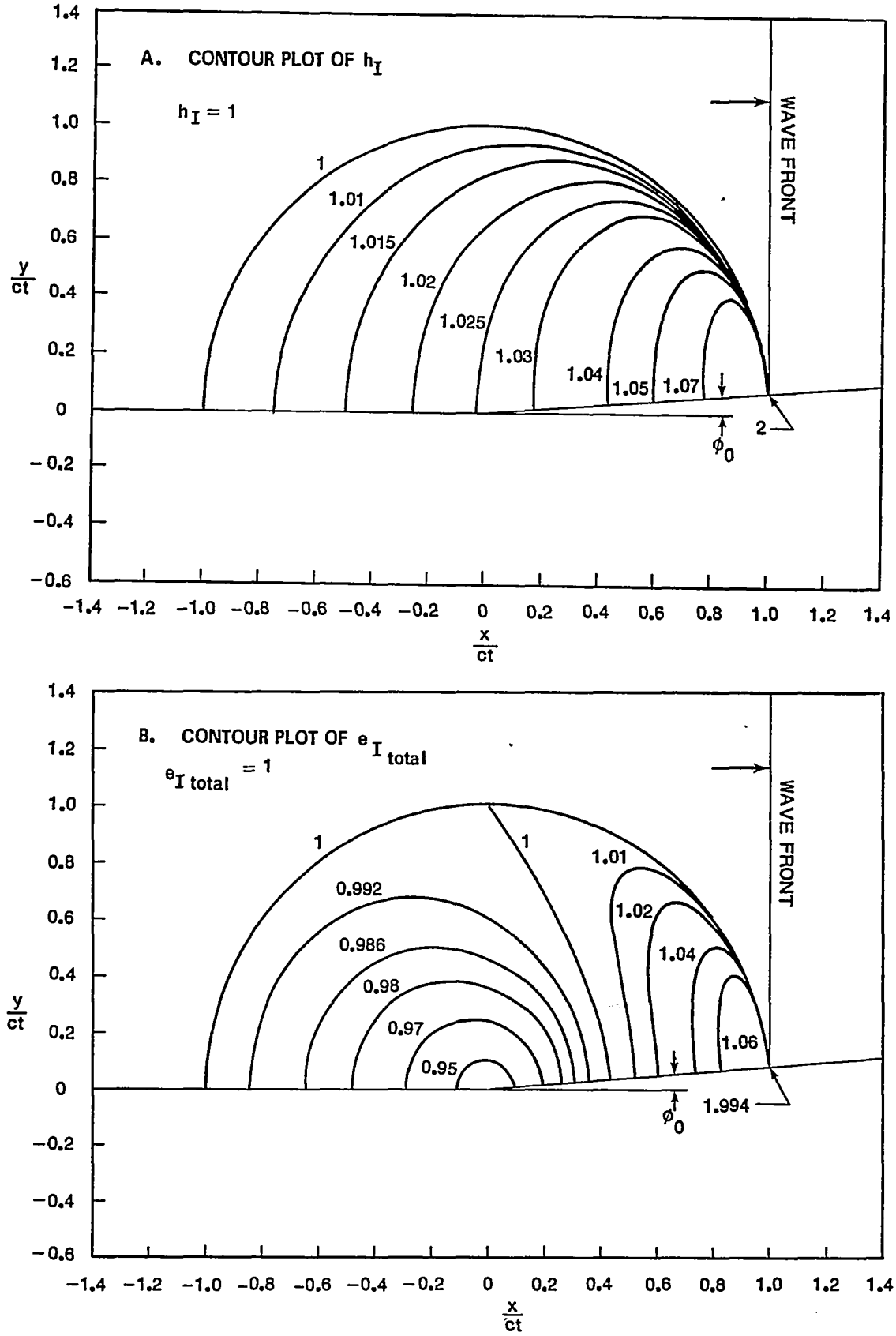

FIGURE 8. DIFFRACTION OF A STEP FUNCTION WAVE AT A BEND IN A PERFECTLY CONDUCTING SHEET FOR $\frac{\phi_0}{\pi}$=0.025

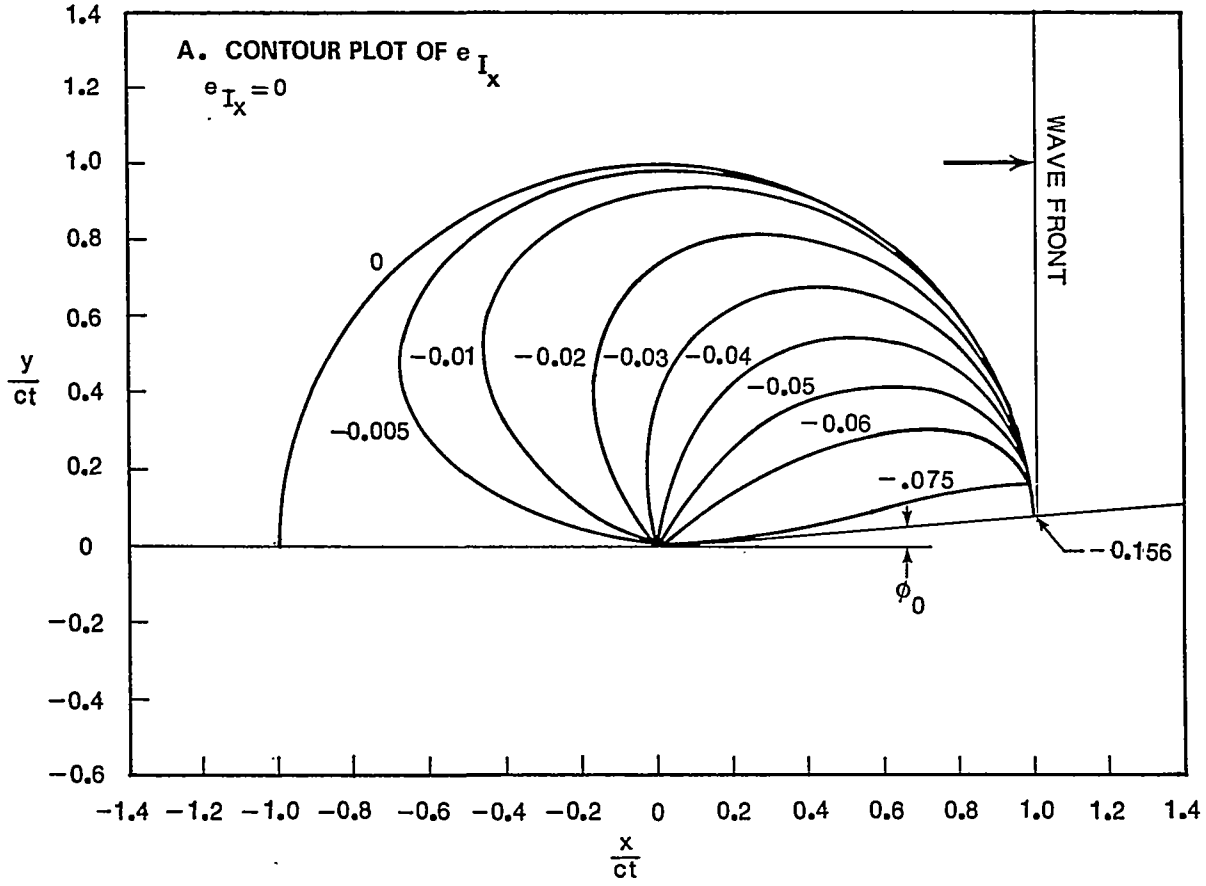

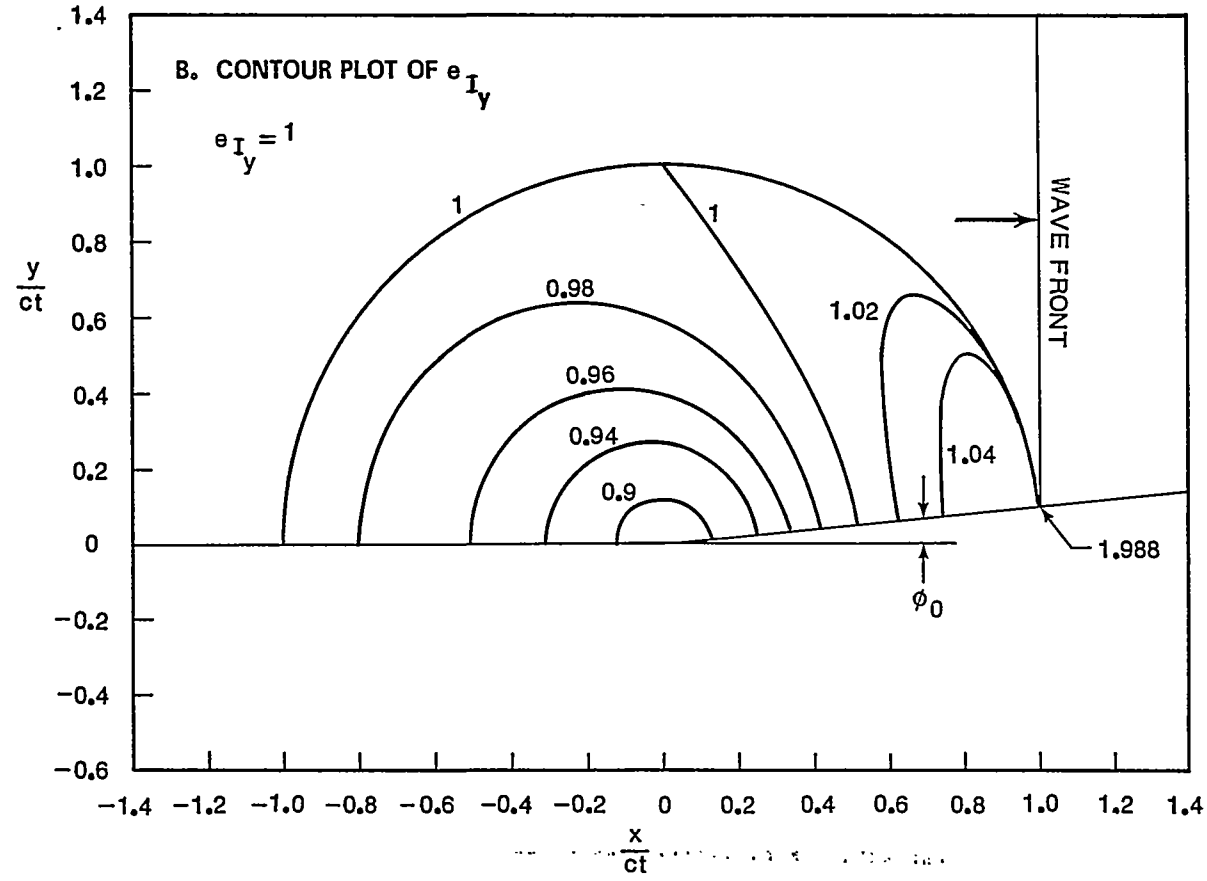

FIGURE 9. DIFFRACTION OF A STEP FUNCTION WAVE AT A BEND IN A PERFECTLY CONDUCTING SHEET FOR $\frac{\phi_0}{\pi}=0.025$

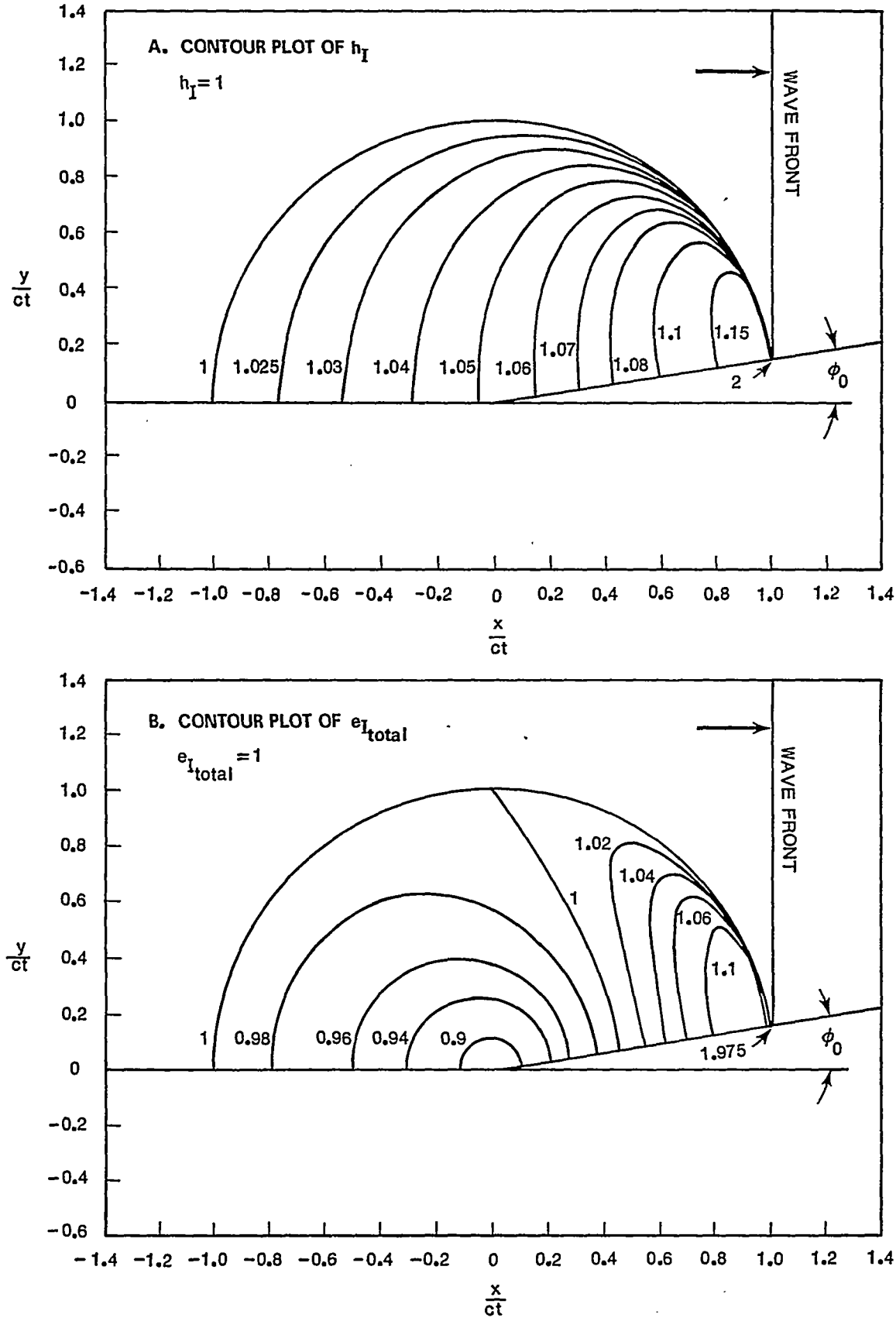

FIGURE 10. DIFFRACTION OF A STEP FUNCTION WAVE AT A BEND IN A PERFECTLY CONDUCTING SHEET FOR $\frac{\phi_0}{\pi} = 0.05$

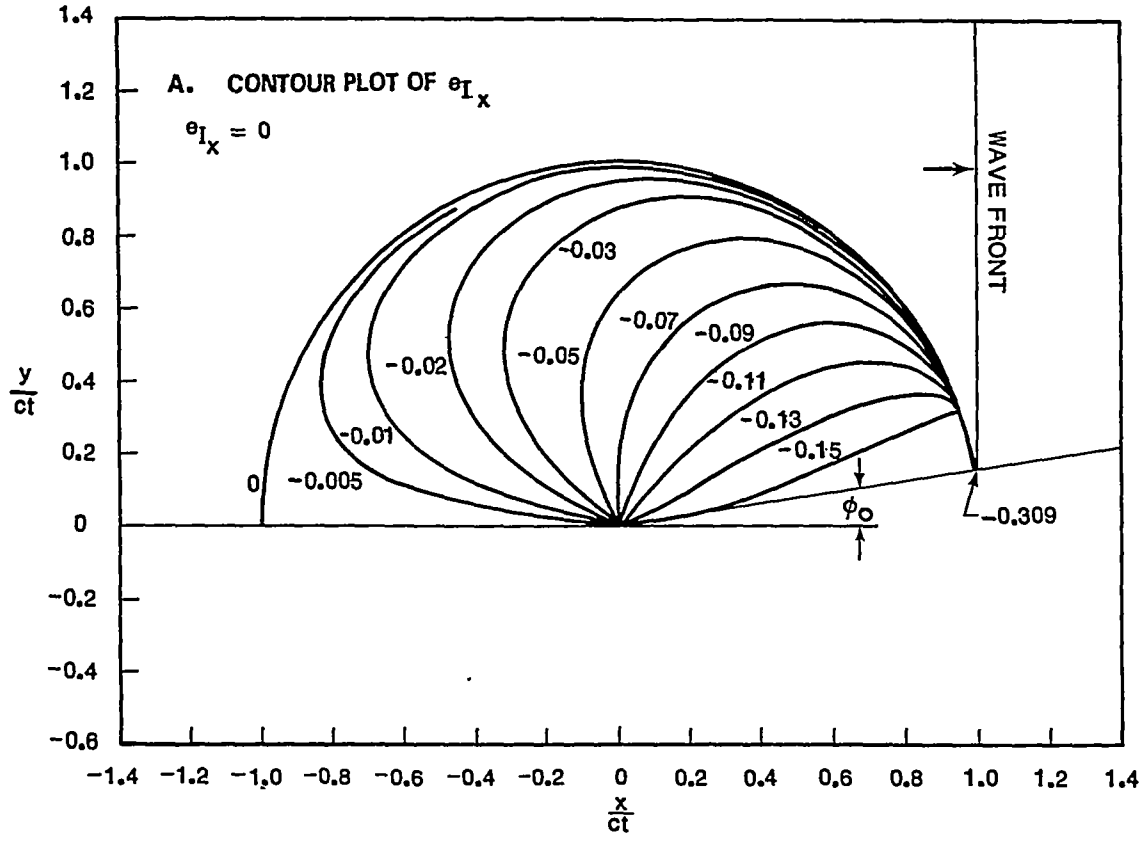

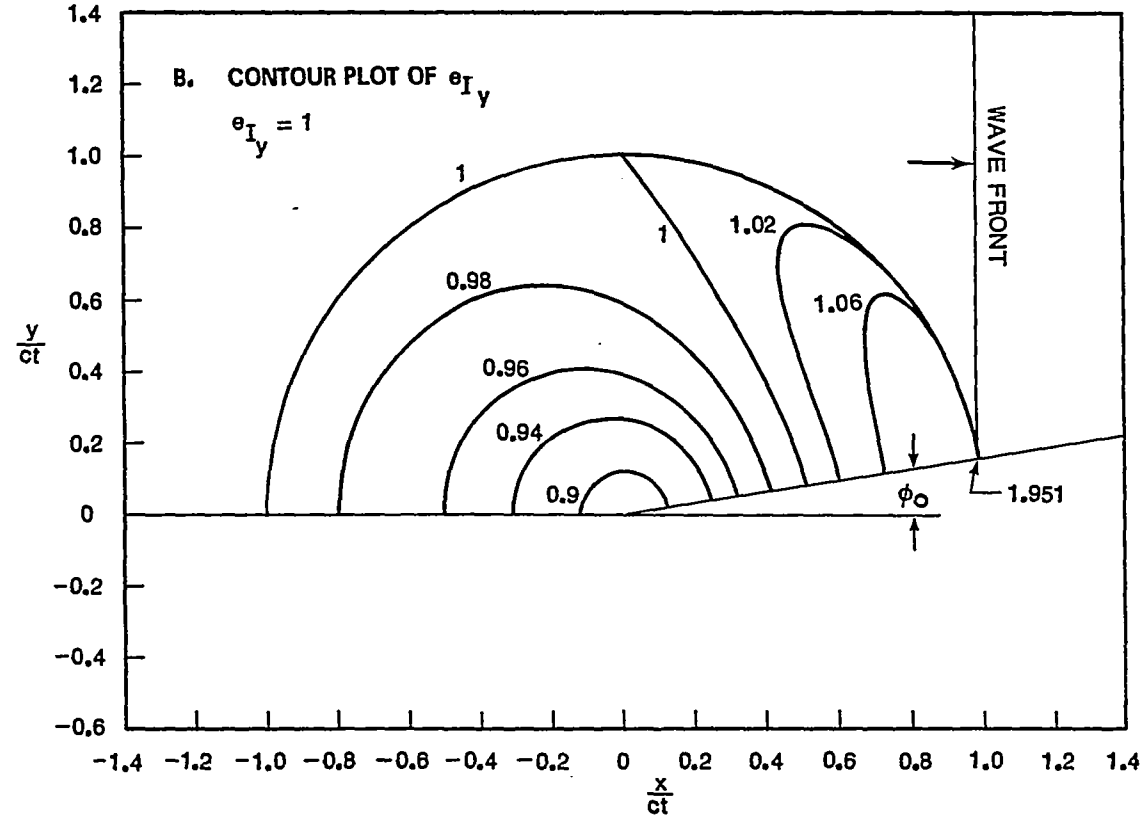

FIGURE 11. DIFFRACTION OF A STEP FUNCTION WAVE AT A BEND IN A PERFECTLY CONDUCTING SHEET FOR $\frac{\phi_0}{\pi} = 0.05$

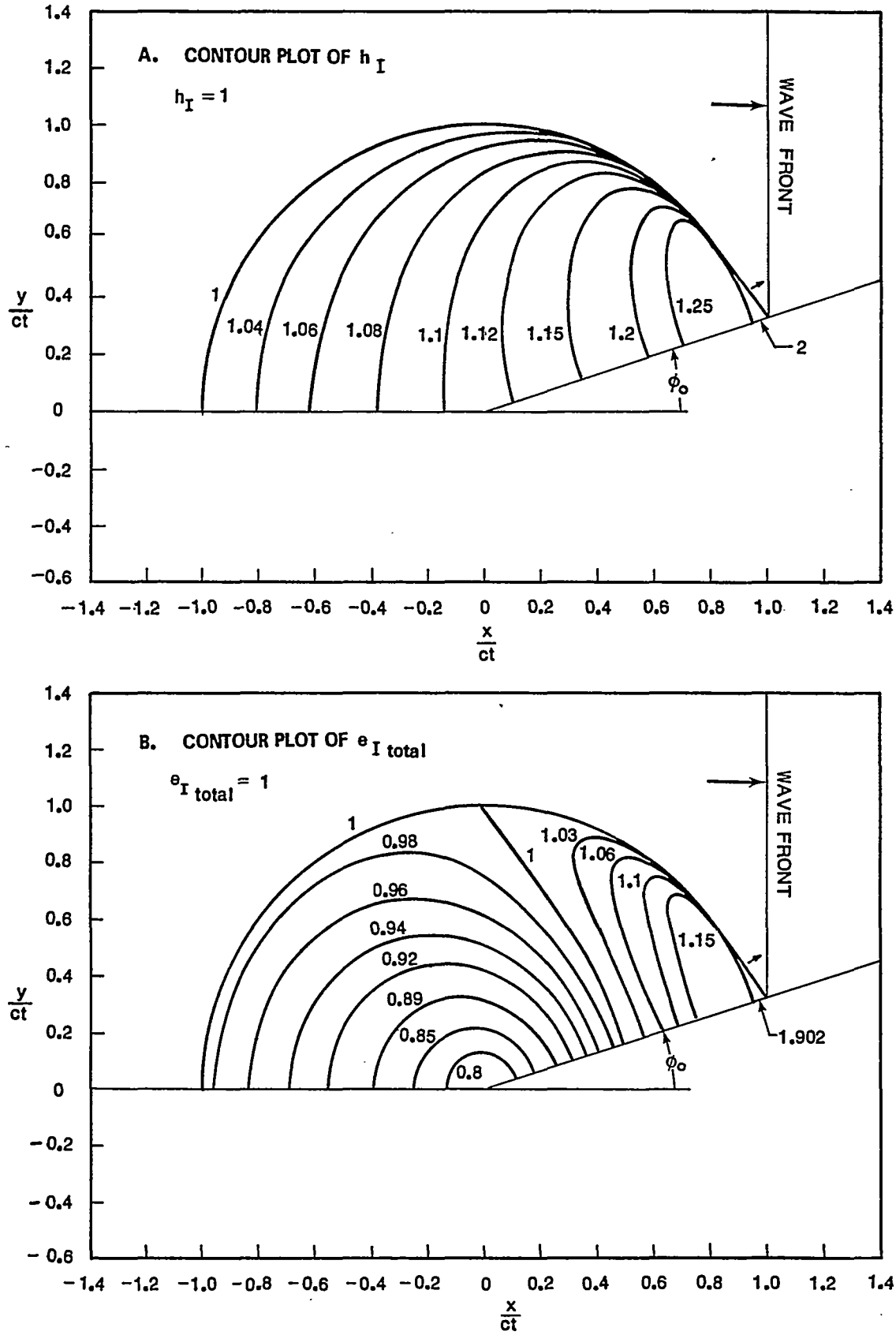

FIGURE 12. DIFFRACTION OF A STEP FUNCTION WAVE AT A BEND IN A PERFECTLY CONDUCTING SHEET FOR $\frac{\phi_0}{\pi} = 0.1$

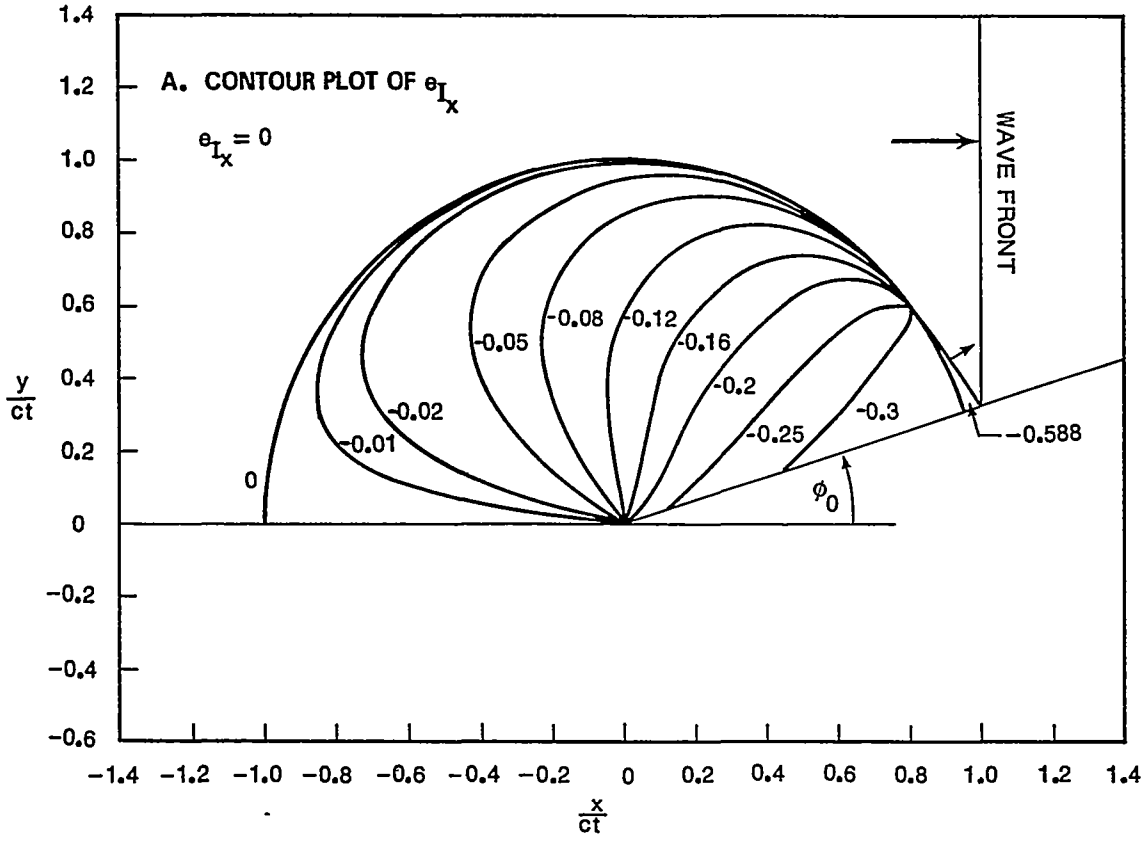

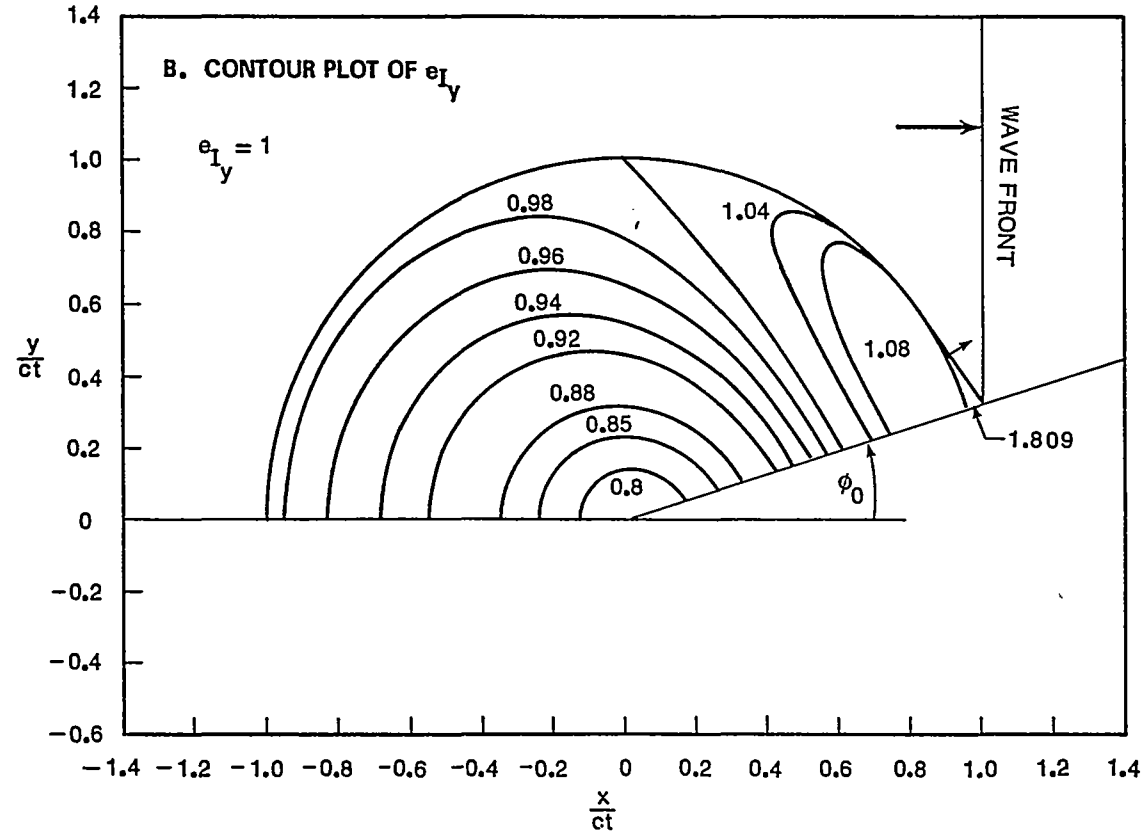

FIGURE 13. DIFFRACTION OF A STEP FUNCTION WAVE AT A BEND IN A PERFECTLY CONDUCTING SHEET FOR $\frac{\phi_0}{\pi} = 0.1$

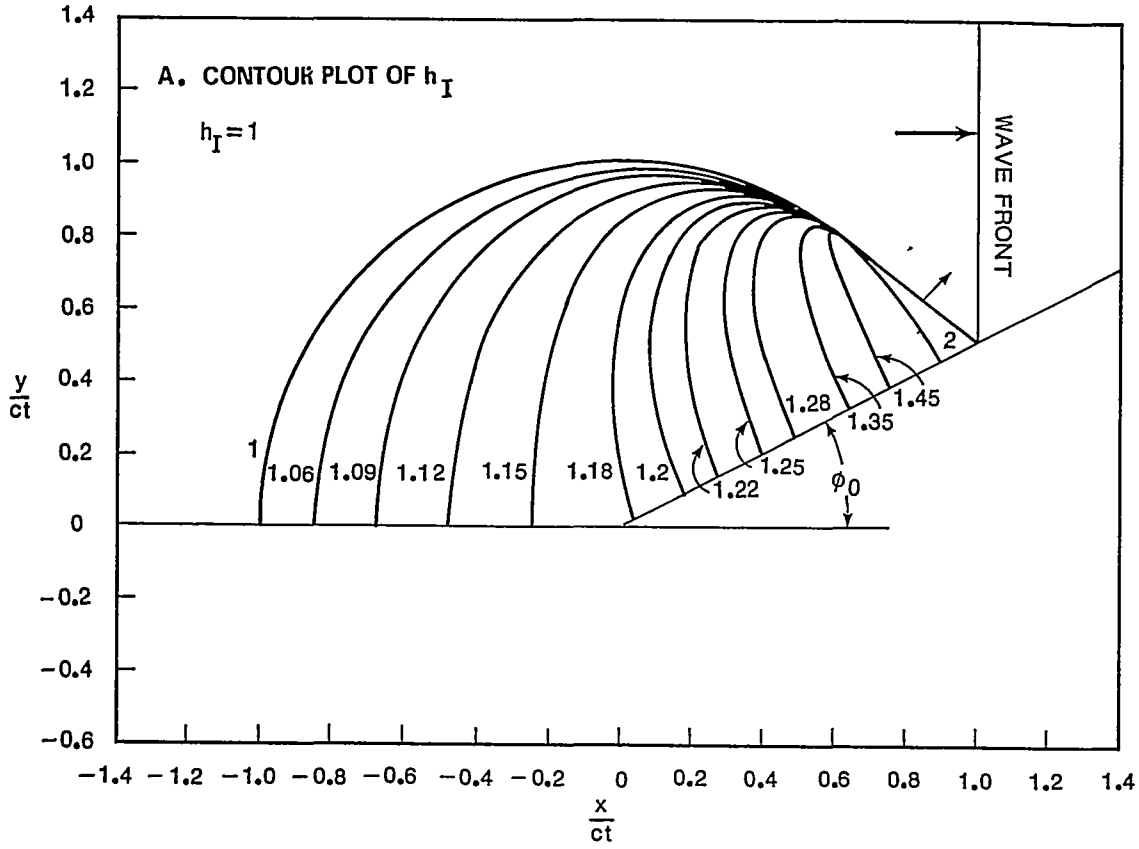

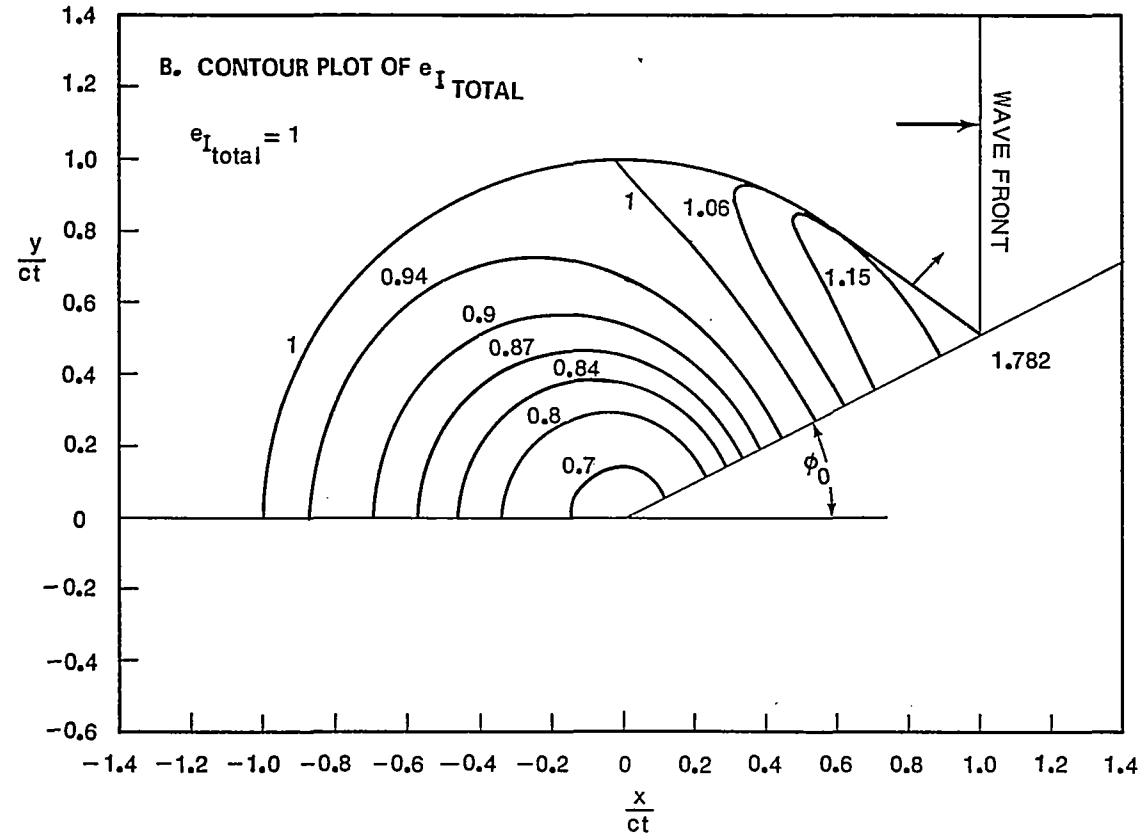

FIGURE 14. DIFFRACTION OF A STEP FUNCTION WAVE AT A BEND IN A PERFECTLY CONDUCTING SHEET FOR $\frac{\phi_0}{\pi} = 0.15$

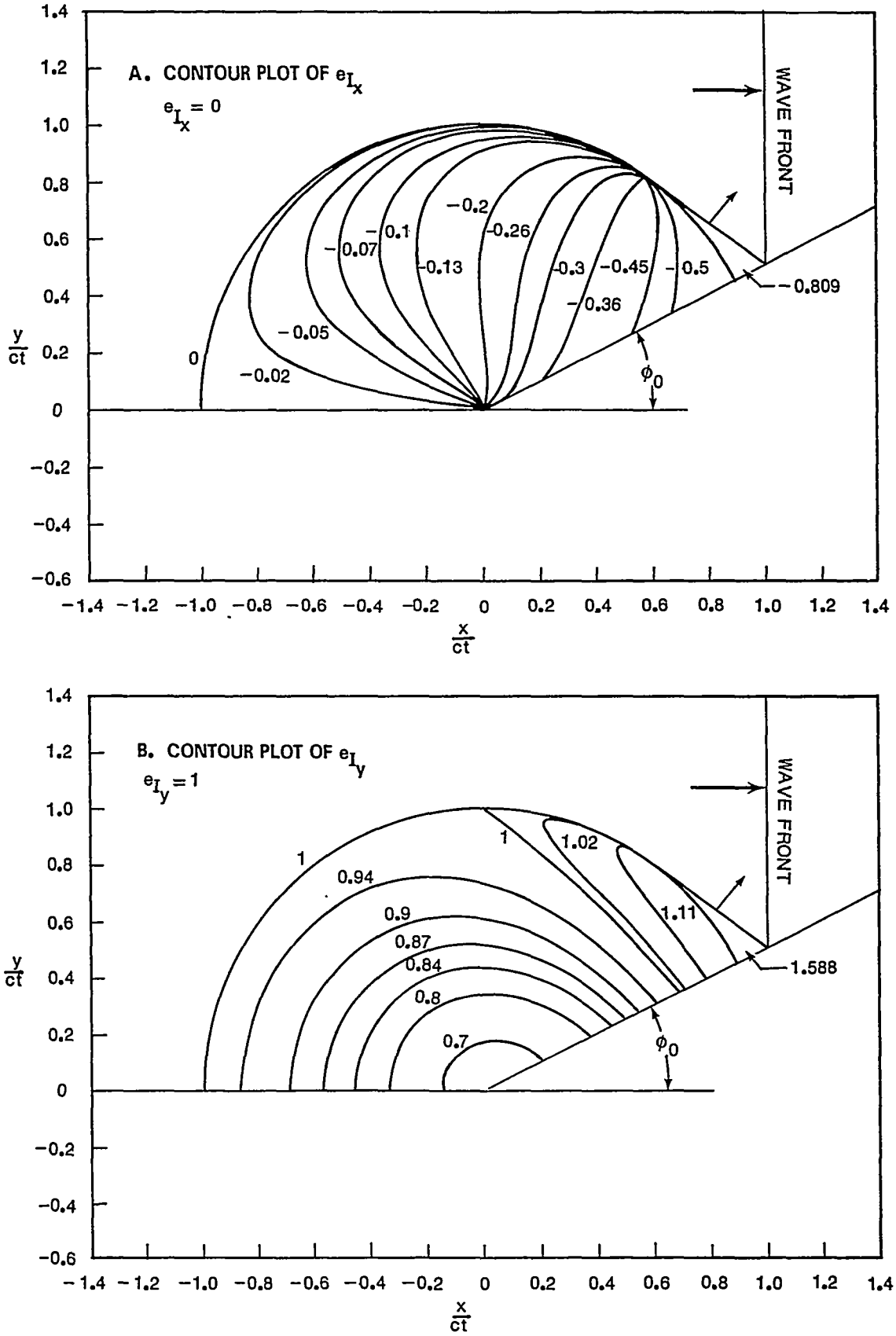

FIGURE 15. DIFFRACTION OF A STEP FUNCTION WAVE AT A BEND IN A PERFECTLY CONDUCTING SHEET FOR $\frac{\phi_0}{\pi} = 0.15$

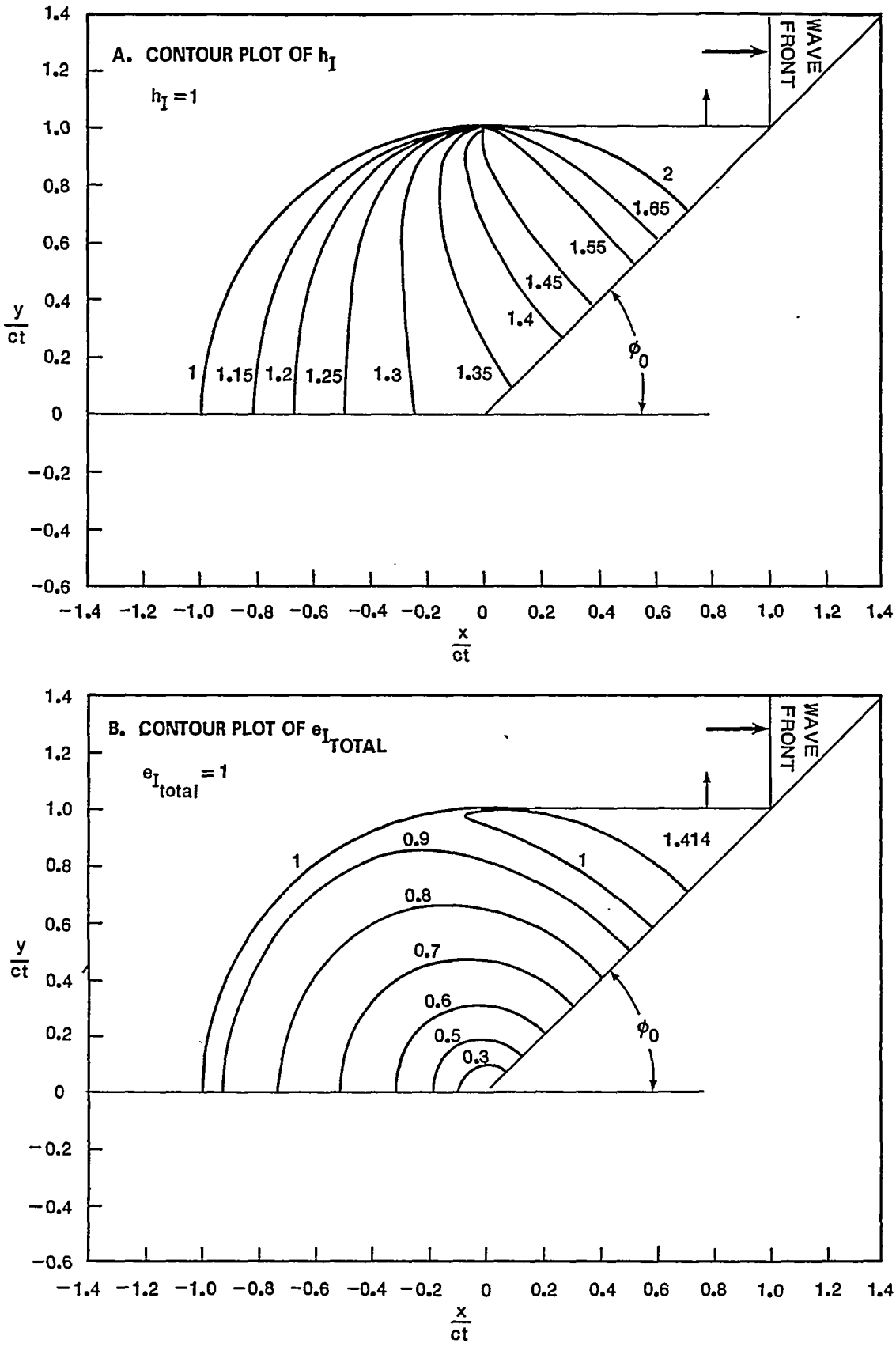

FIGURE 16. DIFFRACTION OF A STEP FUNCTION WAVE AT A BEND IN A PERFECTLY CONDUCTING SHEET FOR $\frac{\phi_0}{\pi} = 0.25$

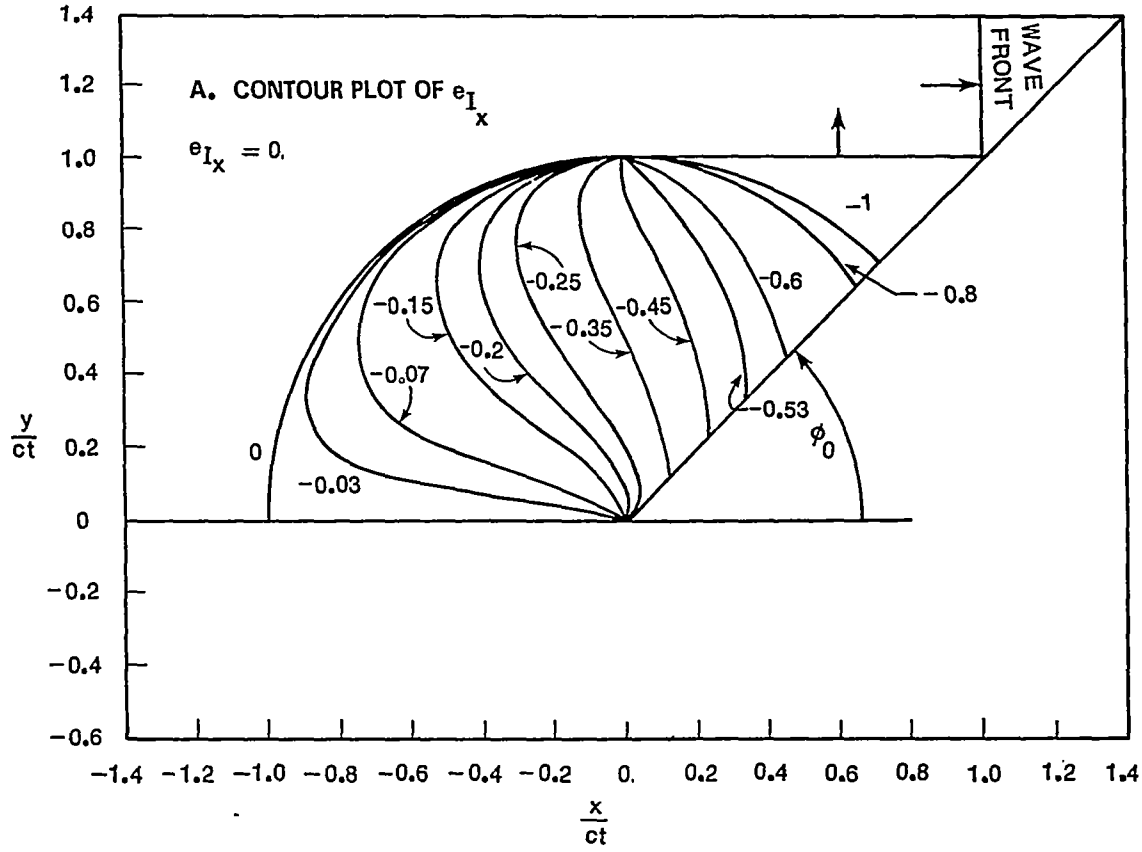

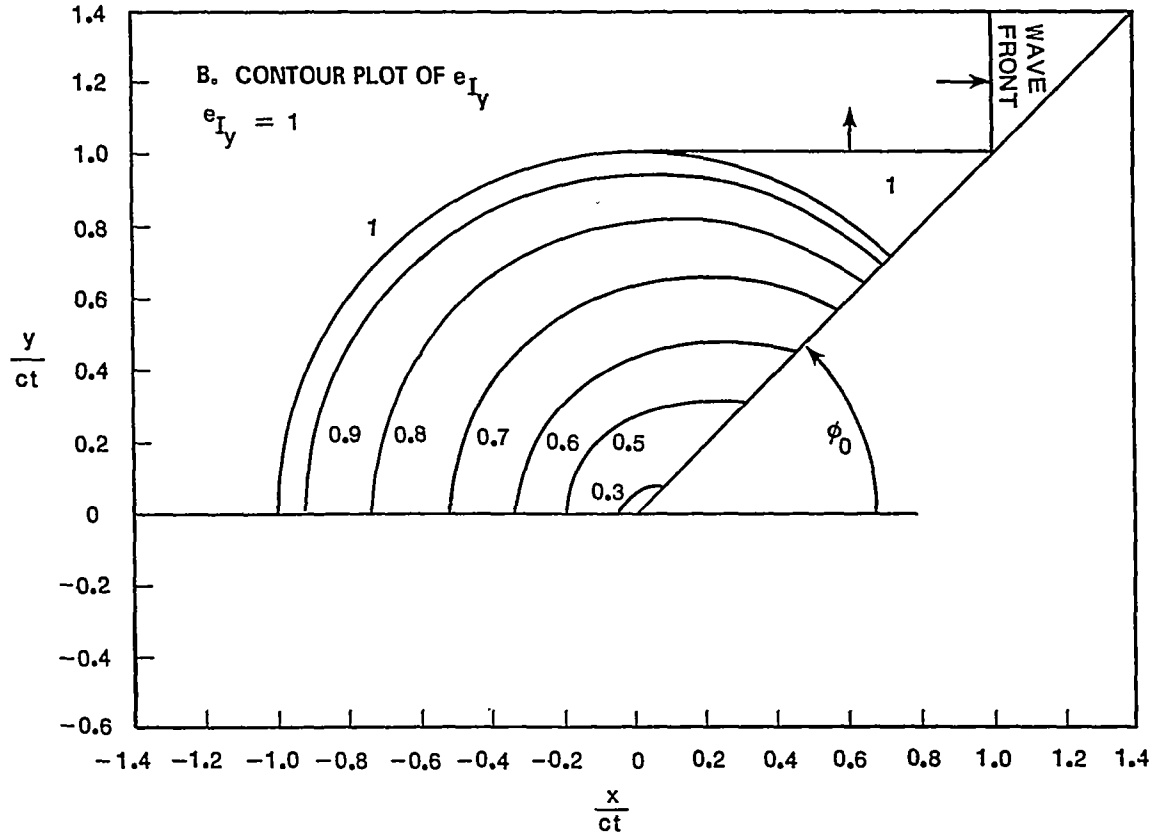

FIGURE 17. DIFFRACTION OF A STEP FUNCTION WAVE AT A BEND IN A PERFECTLY CONDUCTING SHEET FOR $\frac{\phi_0}{\pi} = 0.25$

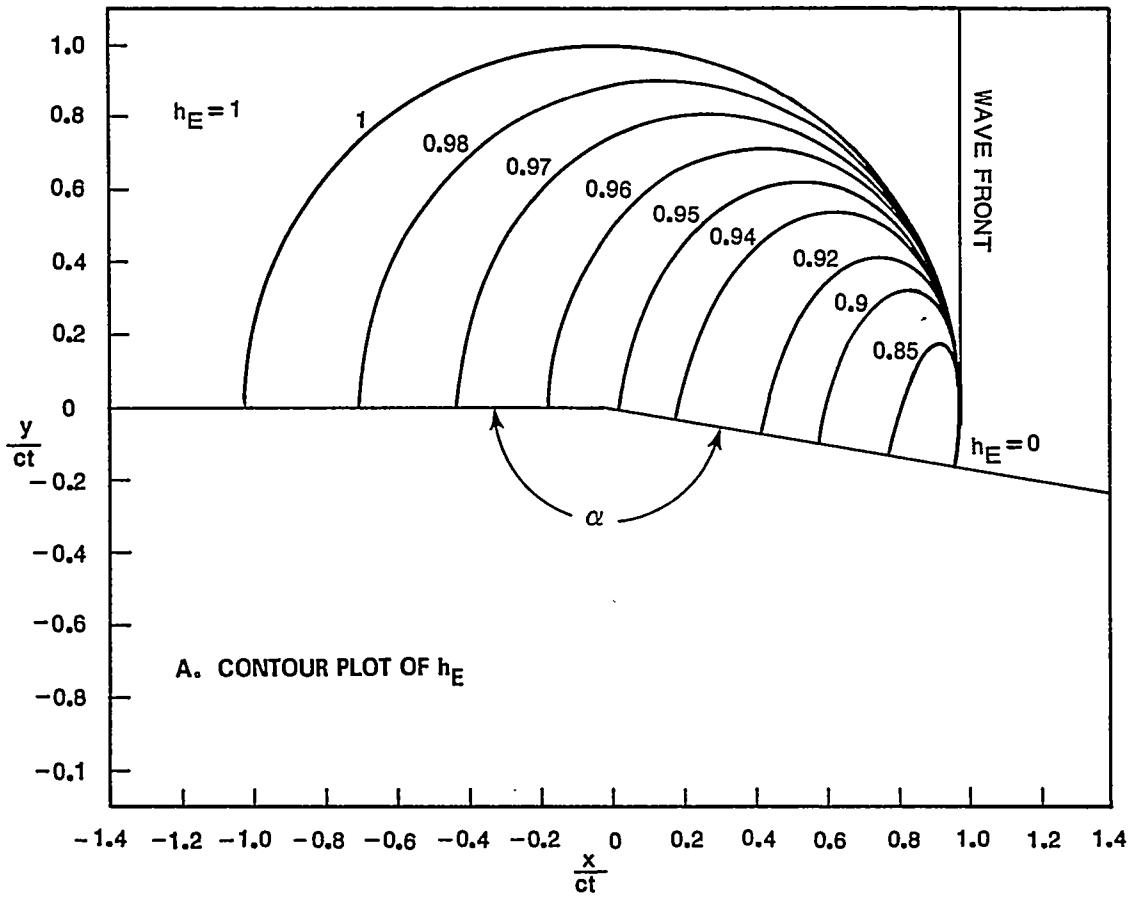

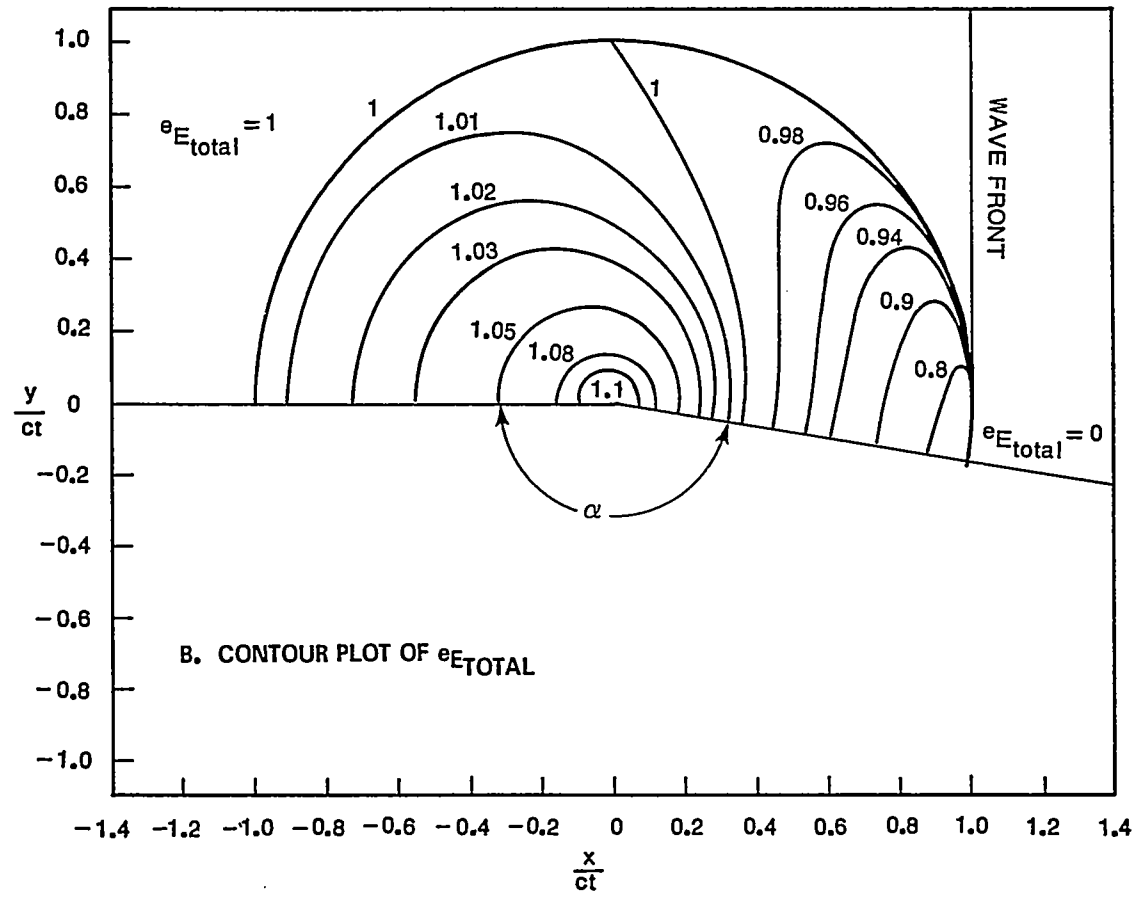

FIGURE 18. DIFFRACTION OF A STEP FUNCTION WAVE AT A BEND IN A PERFECTLY CONDUCTING SHEET FOR $\frac{\alpha}{\pi} = 0.95$

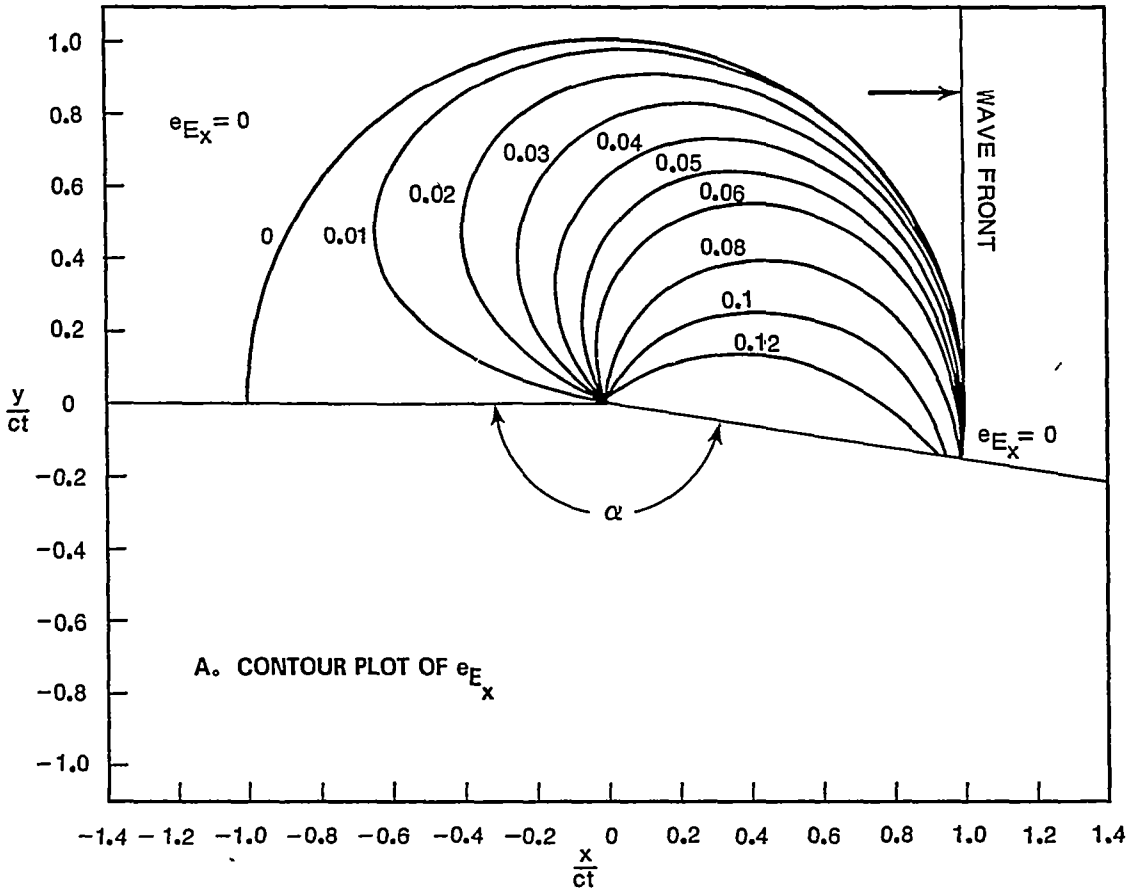

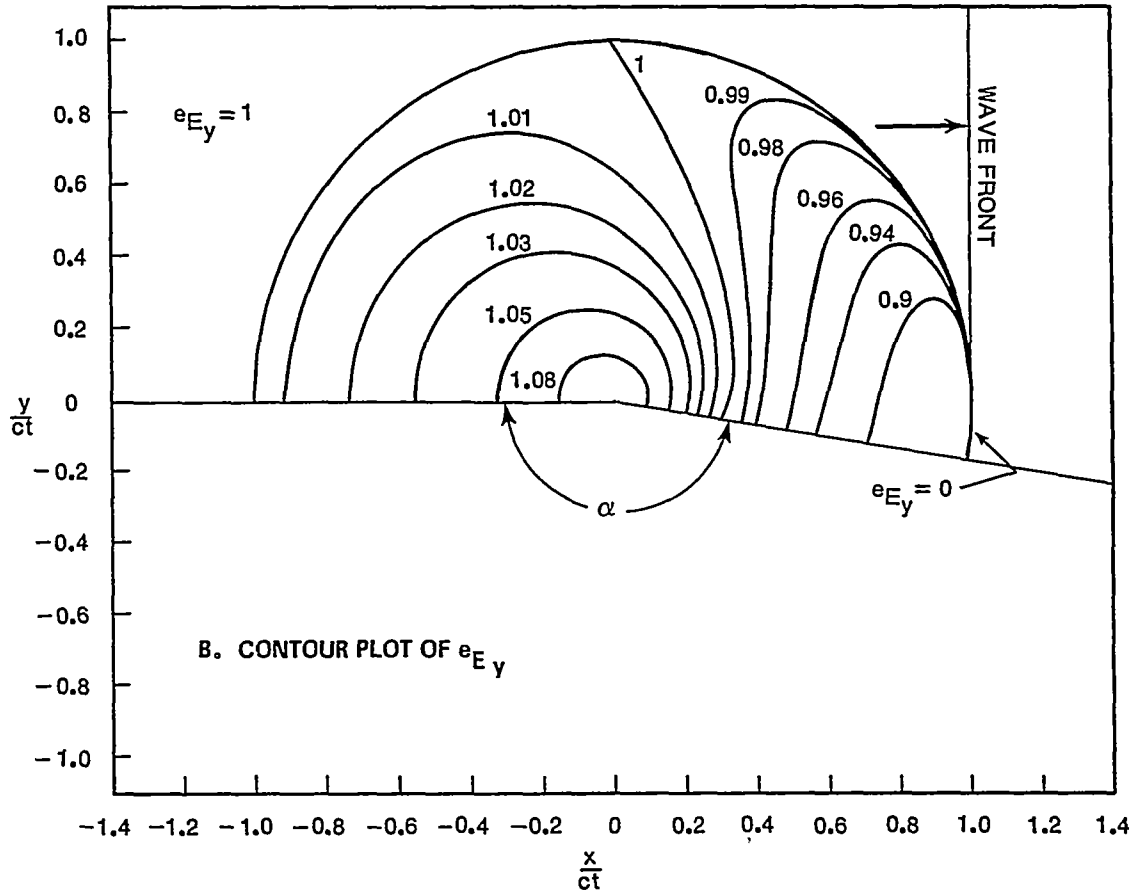

FIGURE 19. DIFFRACTION OF A STEP FUNCTION WAVE AT A BEND IN A PERFECTLY CONDUCTING SHEET FOR $\frac{\alpha}{\pi} = 0.95$

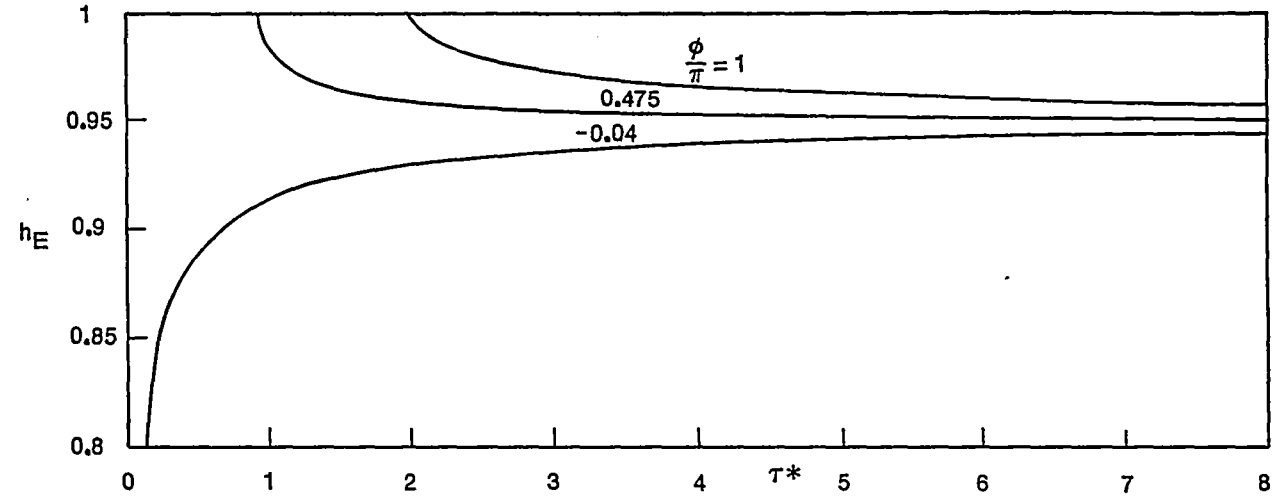

A h_E VS τ^* WITH $\frac{\phi}{\pi}$ AS A PARAMETER

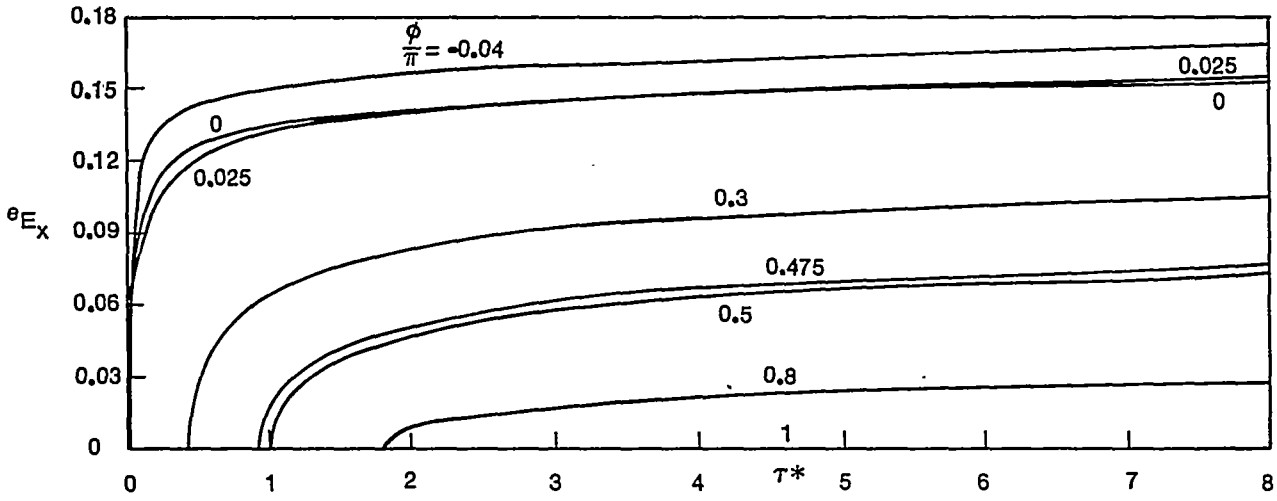

B. e_{E_x} VS τ^* WITH $\frac{\phi}{\pi}$ AS A PARAMETER

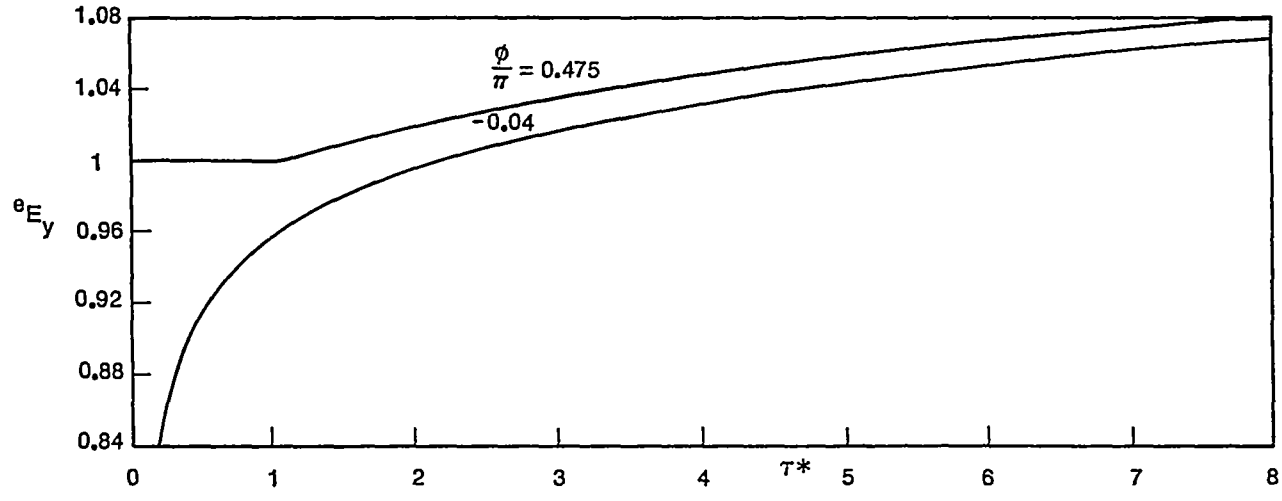

C. e_{E_y} VS τ^* WITH $\frac{\phi}{\pi}$ AS A PARAMETER

FIGURE 20. PULSE SHAPES FOR DIFFRACTION OF A STEP FUNCTION WAVE AT A BEND IN A PERFECTLY CONDUCTING SHEET $\frac{\alpha}{\pi} = 0.95$

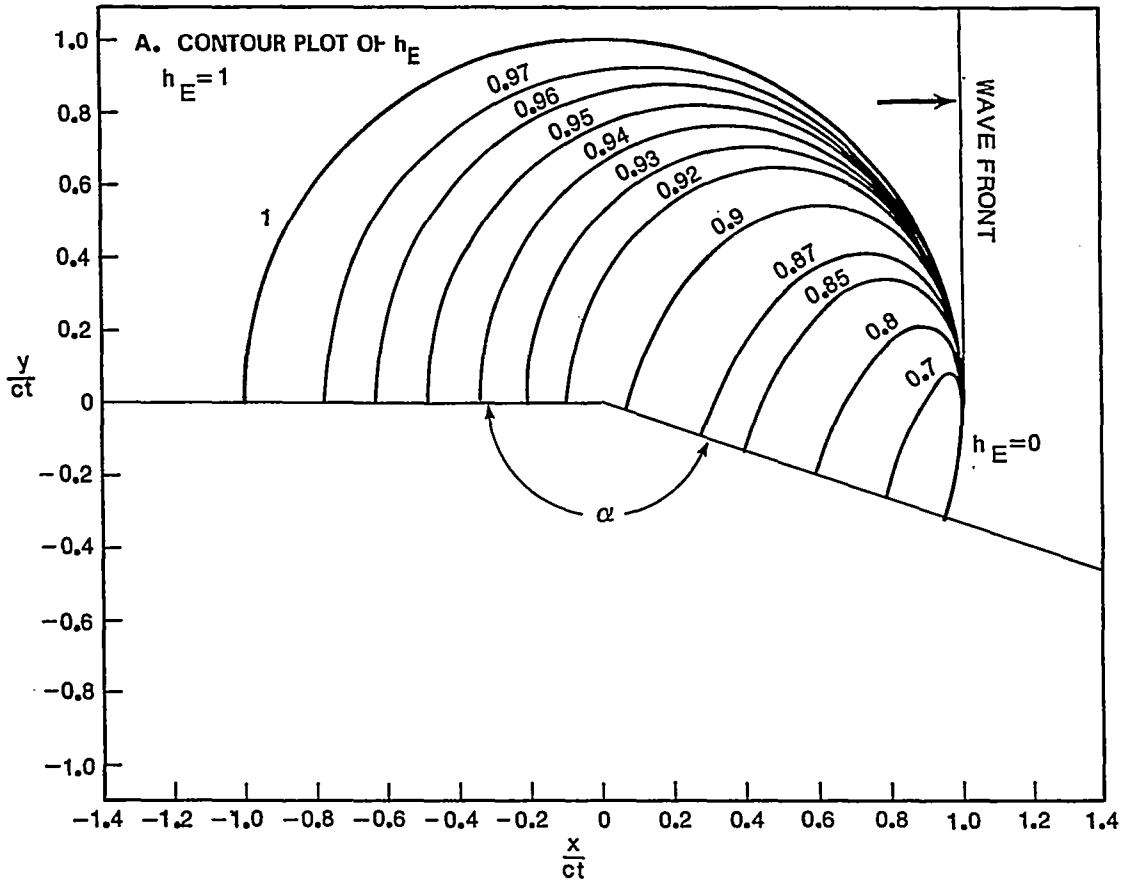

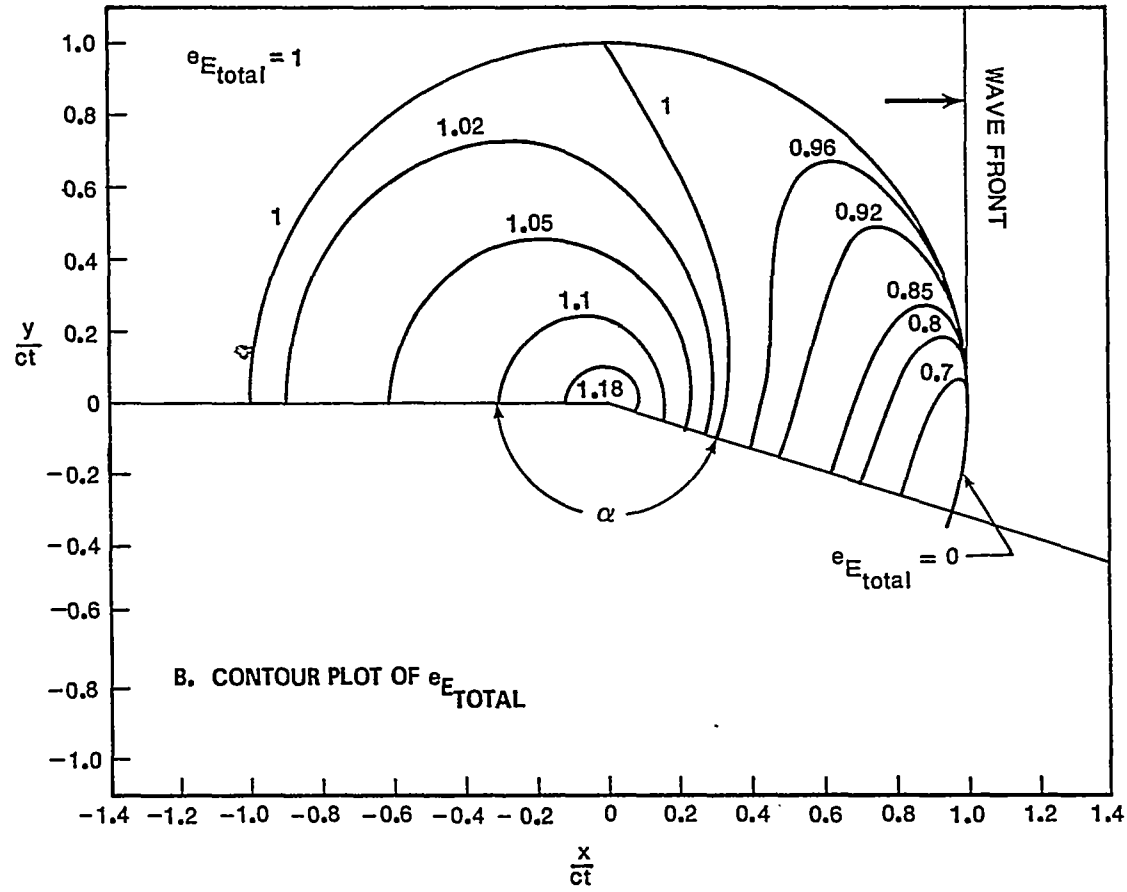

FIGURE 21. DIFFRACTION OF A STEP FUNCTION WAVE AT A BEND IN A PERFECTLY CONDUCTING SHEET FOR $\frac{\alpha}{\pi}=0.9$

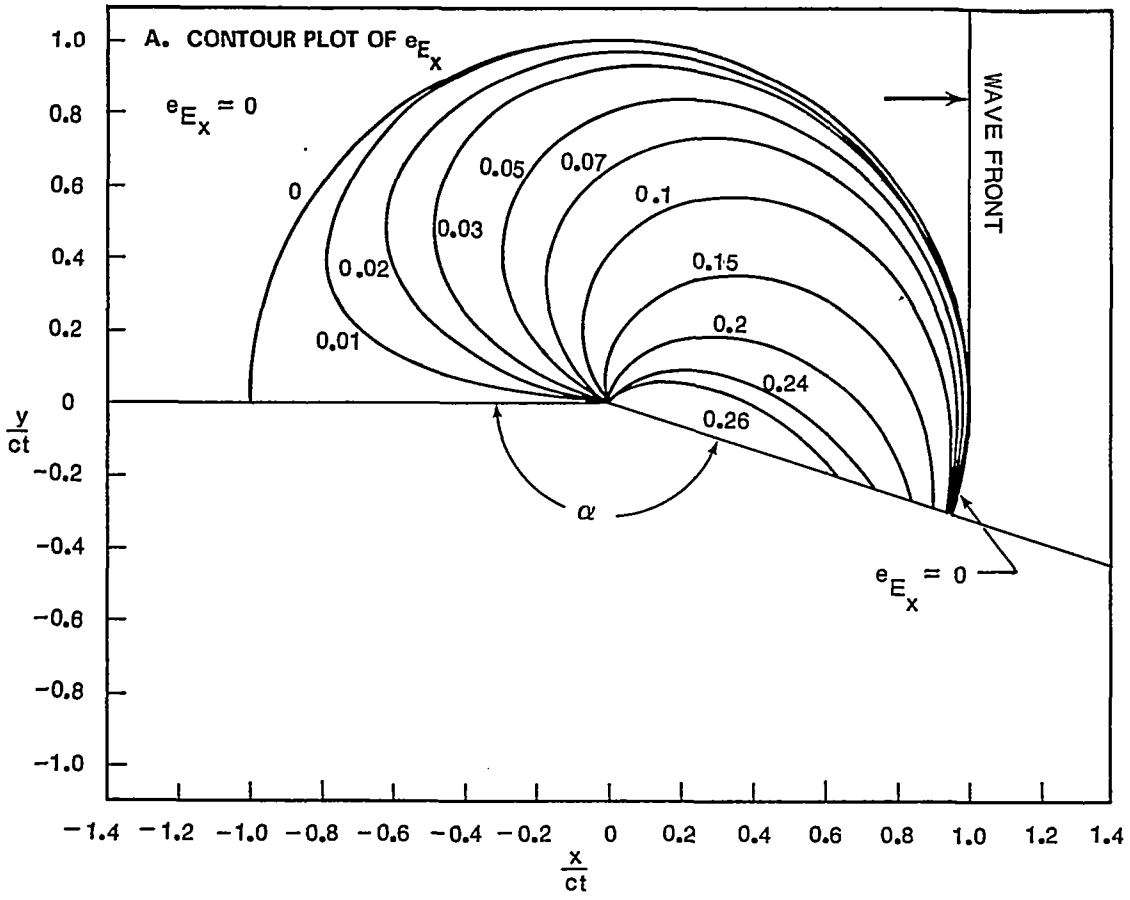

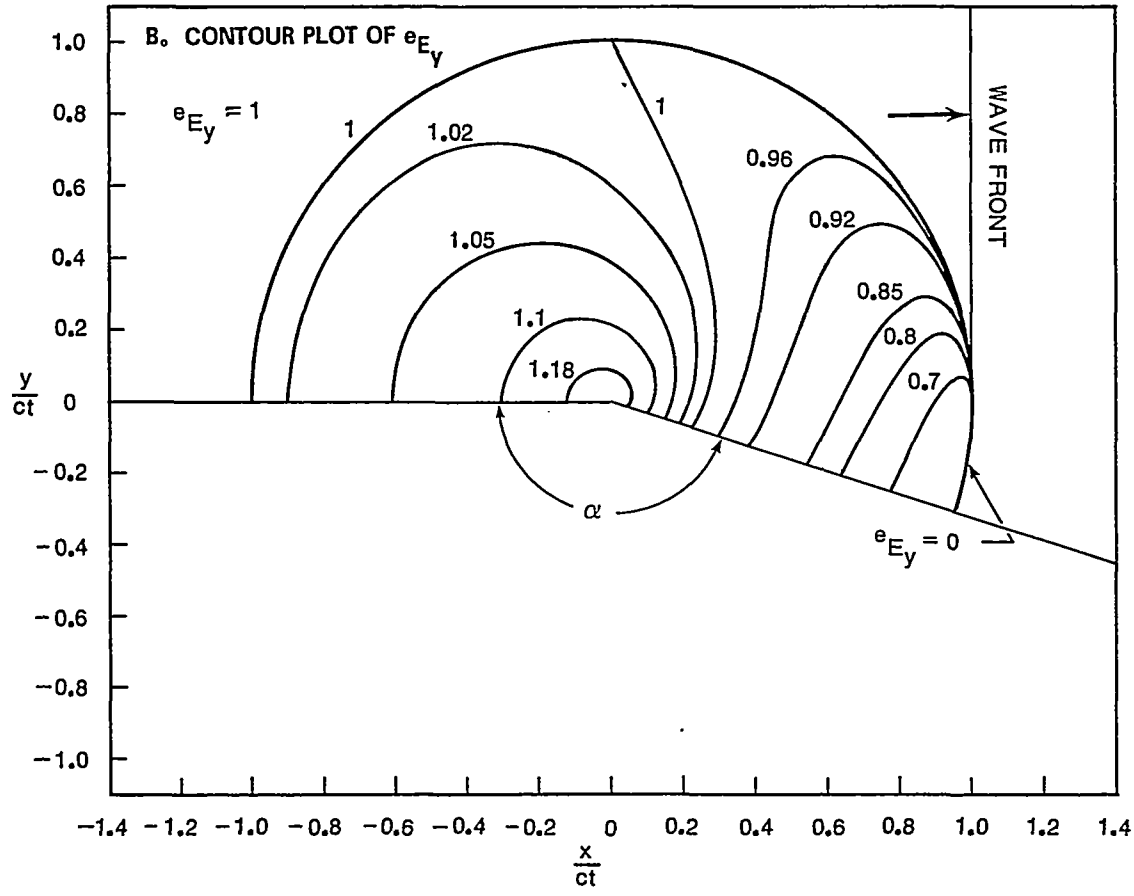

FIGURE 22. DIFFRACTION OF A STEP FUNCTION WAVE AT A BEND IN A PERFECTLY CONDUCTING SHEET FOR $\frac{\alpha}{\pi} = 0.9$

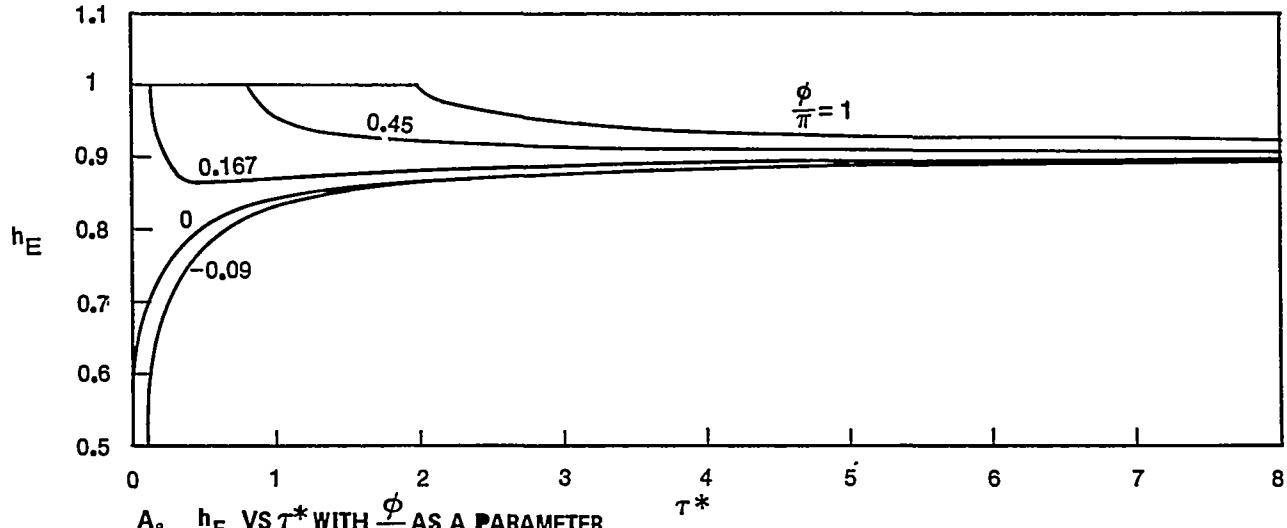

A. h_E VS τ^* WITH $\frac{\phi}{\pi}$ AS A PARAMETER

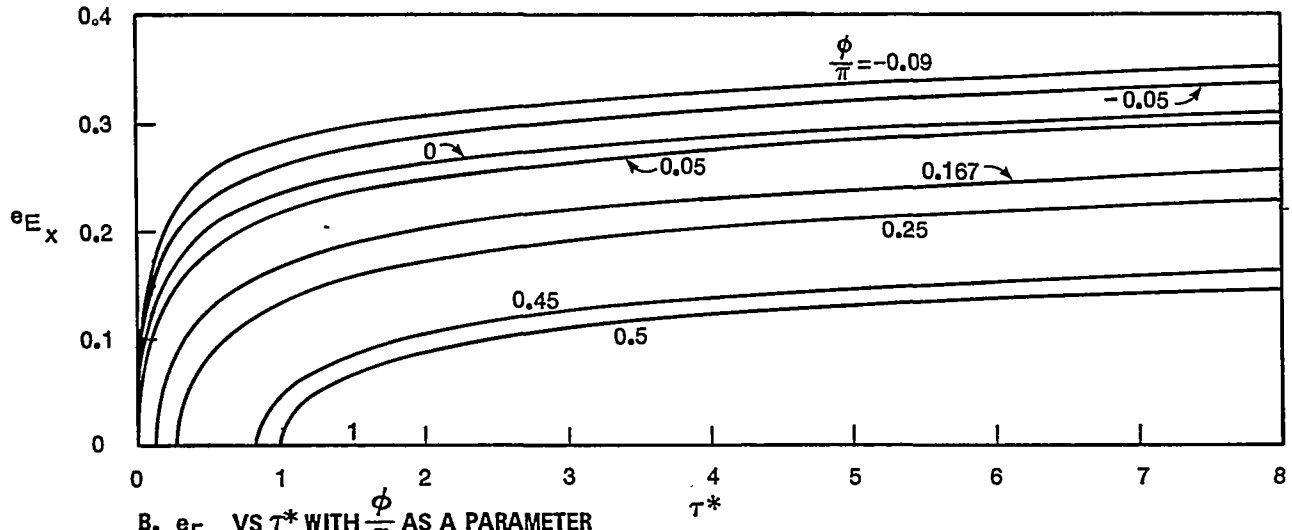

B. e_{E_x} VS τ^* WITH $\frac{\phi}{\pi}$ AS A PARAMETER

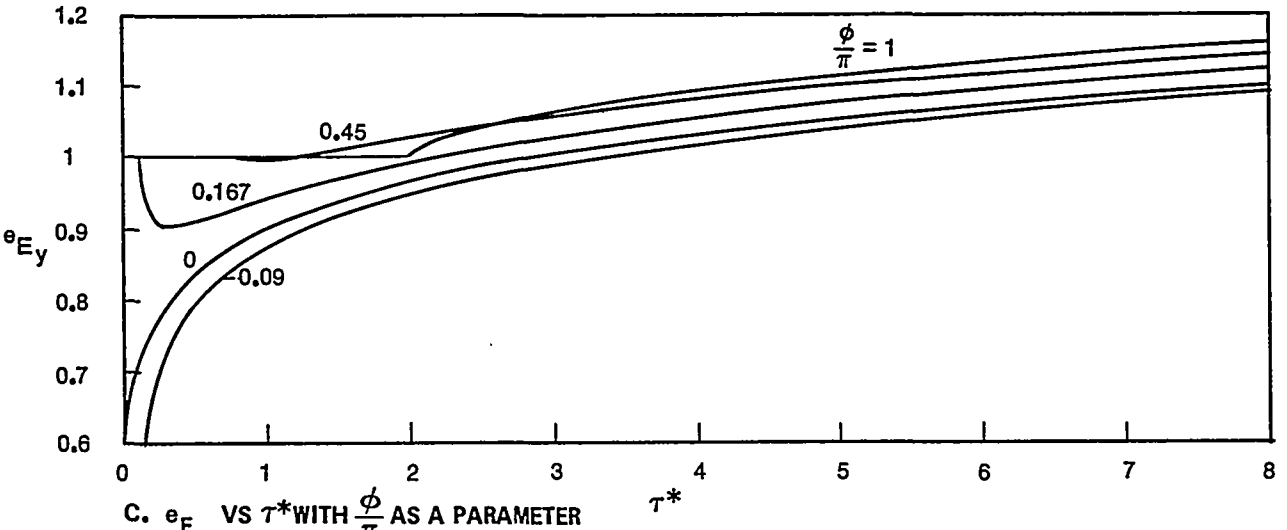

C. e_{E_y} VS τ^* WITH $\frac{\phi}{\pi}$ AS A PARAMETER

FIGURE 23. PULSE SHAPES FOR DIFFRACTION OF A STEP FUNCTION WAVE AT A BEND IN A PERFECTLY CONDUCTING SHEET $\frac{\alpha}{\pi}=0.9$

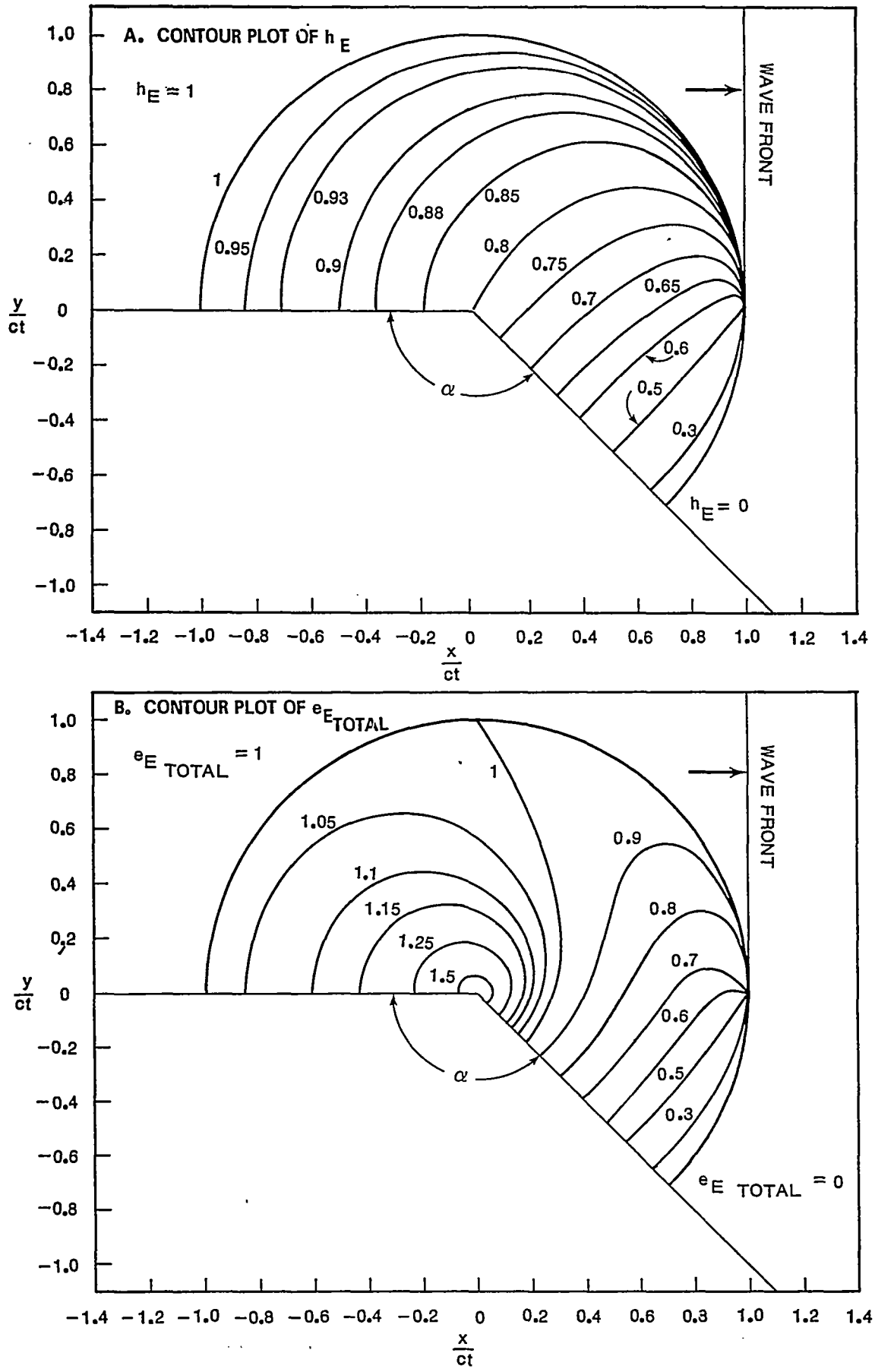

FIGURE 24. DIFFRACTION OF A STEP FUNCTION WAVE AT A BEND IN A PERFECTLY CONDUCTING SHEET FOR $\frac{\alpha}{\pi} = 0.75$

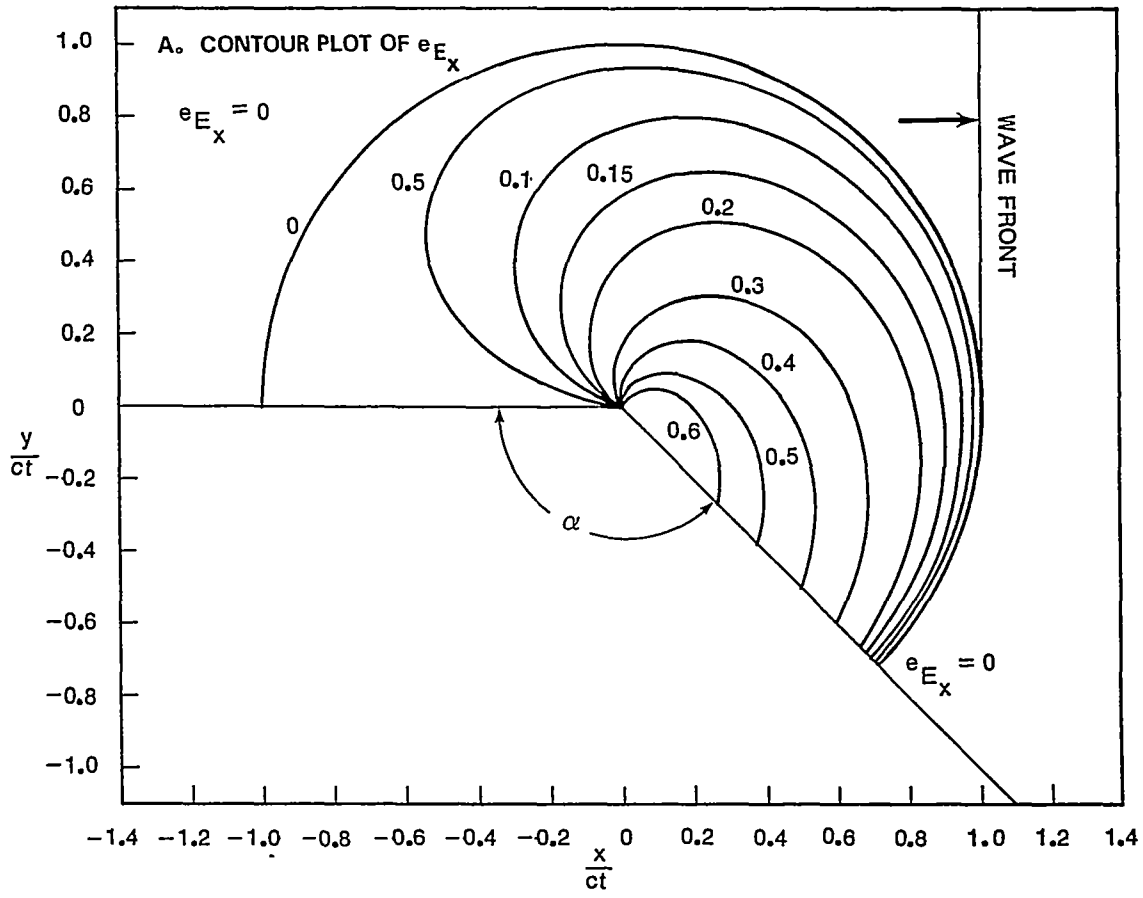

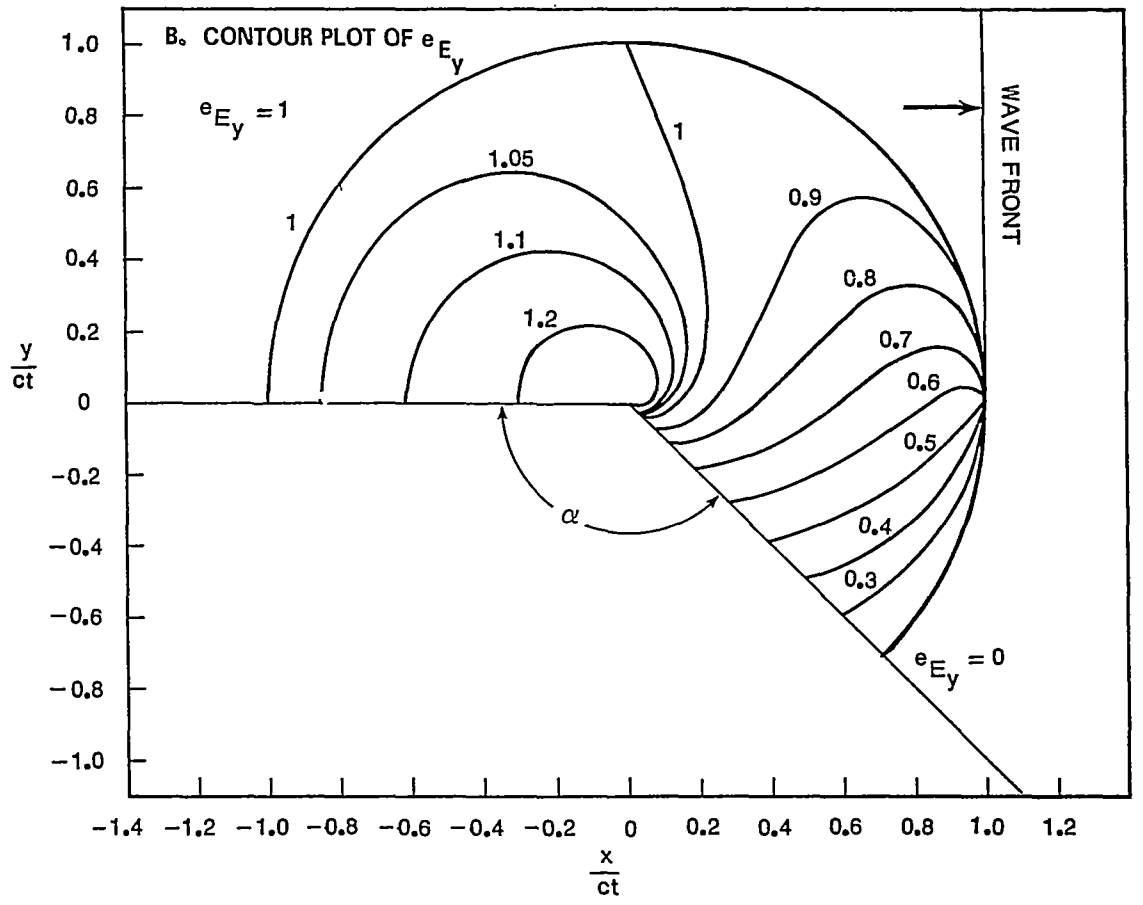

FIGURE 25. DIFFRACTION OF A STEP FUNCTION WAVE AT A BEND IN A PERFECTLY CONDUCTING SHEET FOR $\frac{\alpha}{\pi} = 0.75$

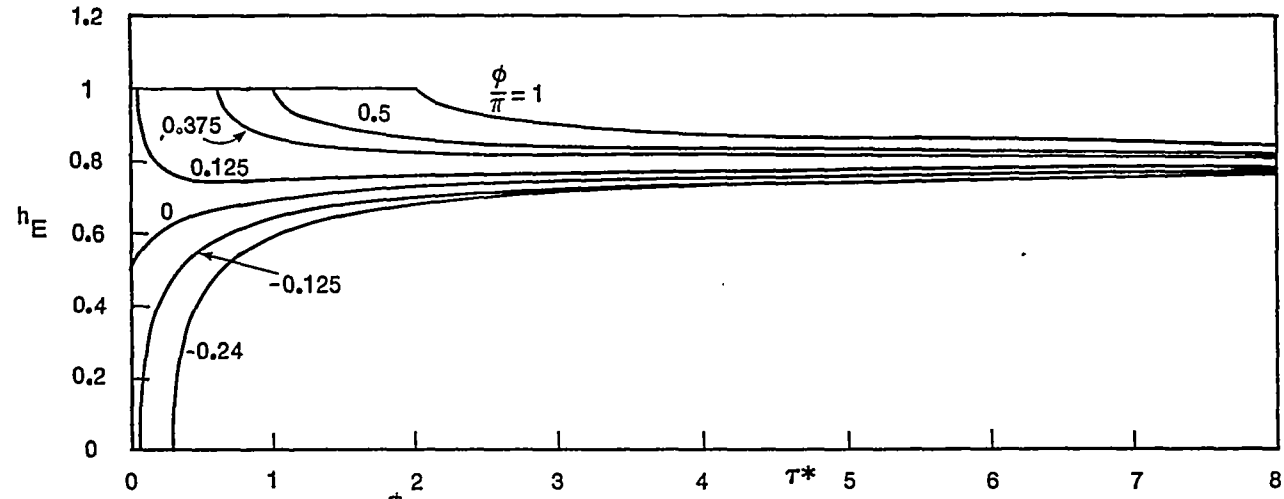

A. h_E VS τ^* WITH $\frac{\phi}{\pi}$ AS A PARAMETER

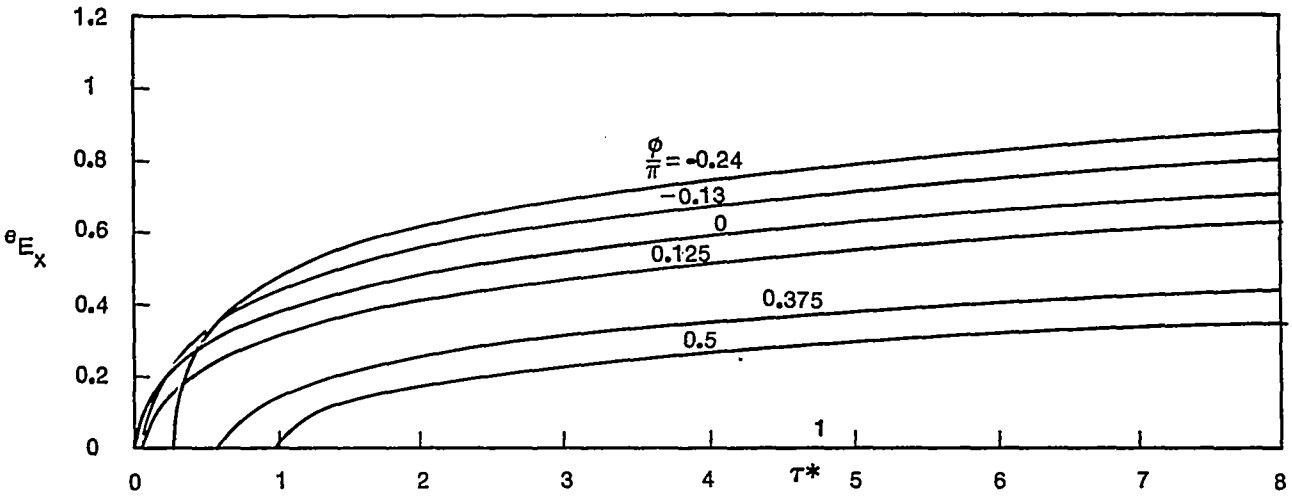

B. e_{E_x} VS τ^* WITH $\frac{\phi}{\pi}$ AS A PARAMETER

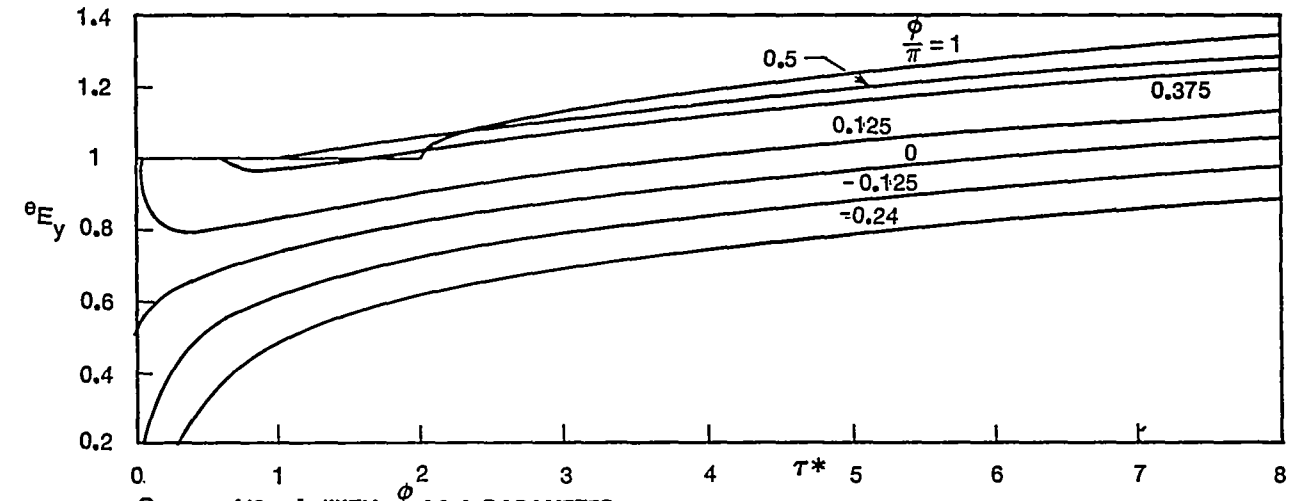

C. e_{E_y} VS τ^* WITH $\frac{\phi}{\pi}$ AS A PARAMETER

FIGURE 26. PULSE SHAPES FOR DIFFRACTION OF A STEP FUNCTION WAVE AT A BEND IN A PERFECTLY CONDUCTING SHEET $\frac{\alpha}{\pi}=0.75$

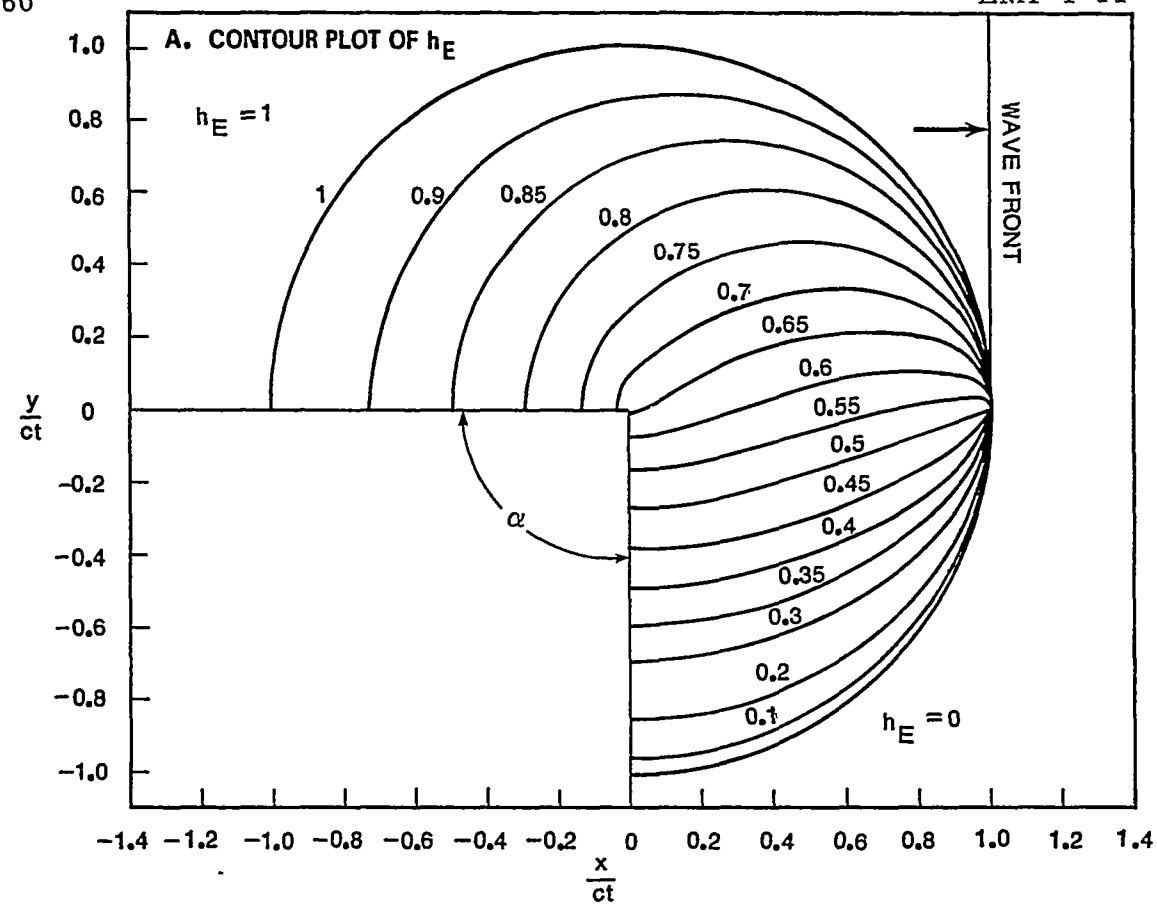

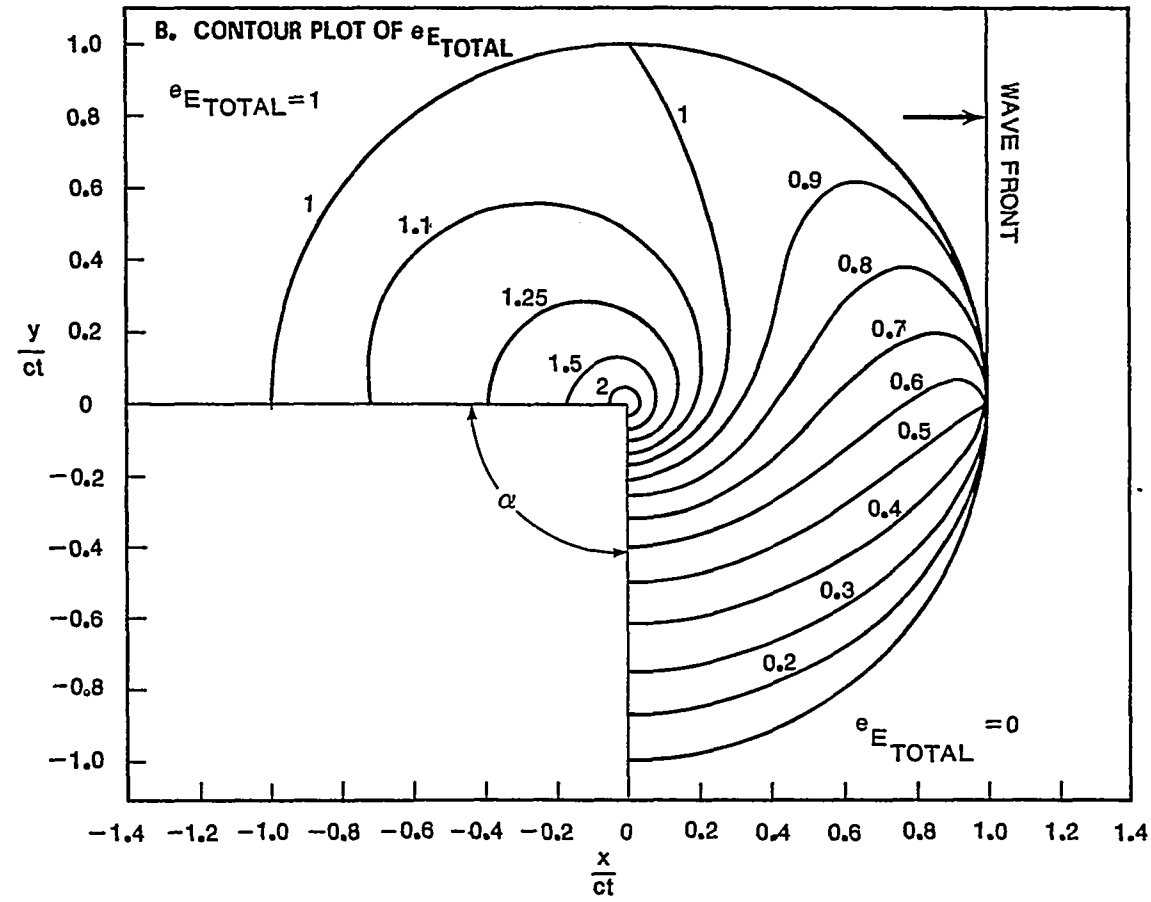

FIGURE 27. DIFFRACTION OF A STEP FUNCTION WAVE AT A BEND IN A PERFECTLY CONDUCTING SHEET FOR $\frac{\alpha}{\pi} = 0.5$

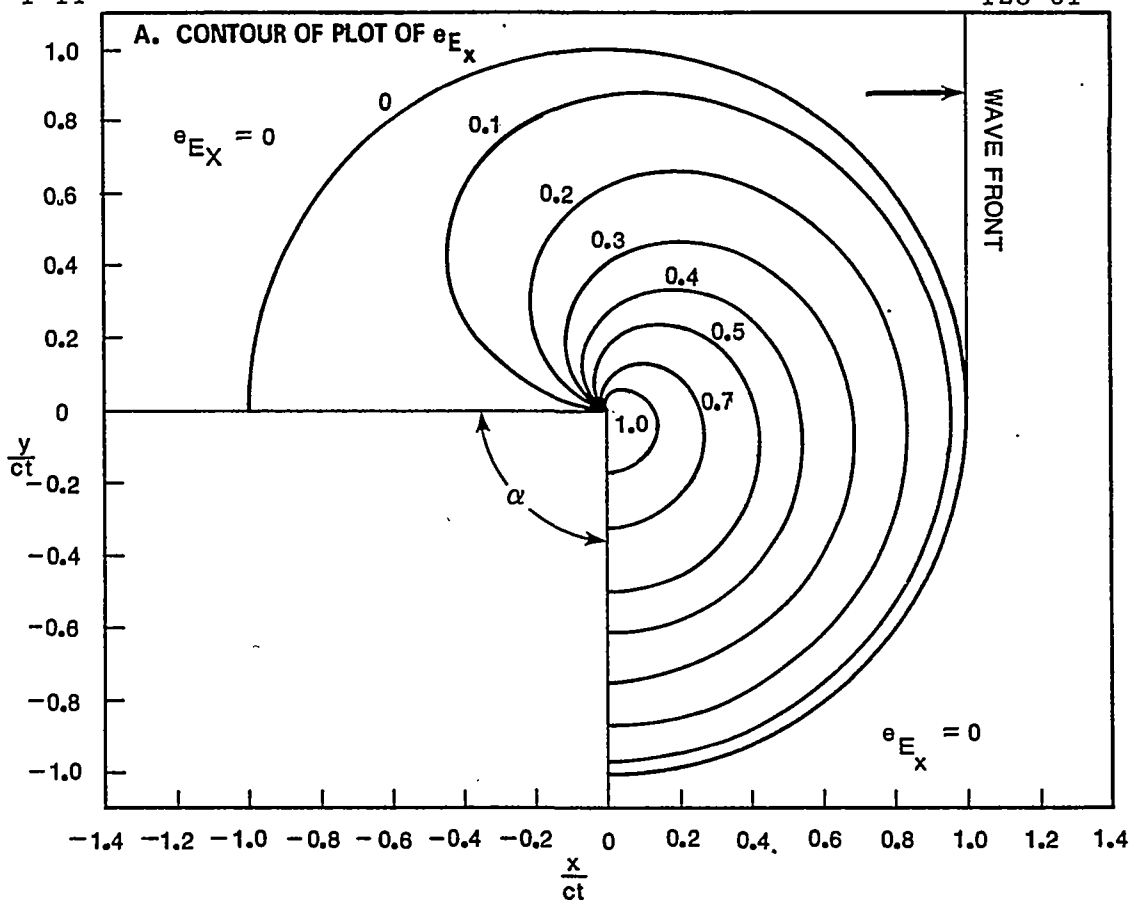

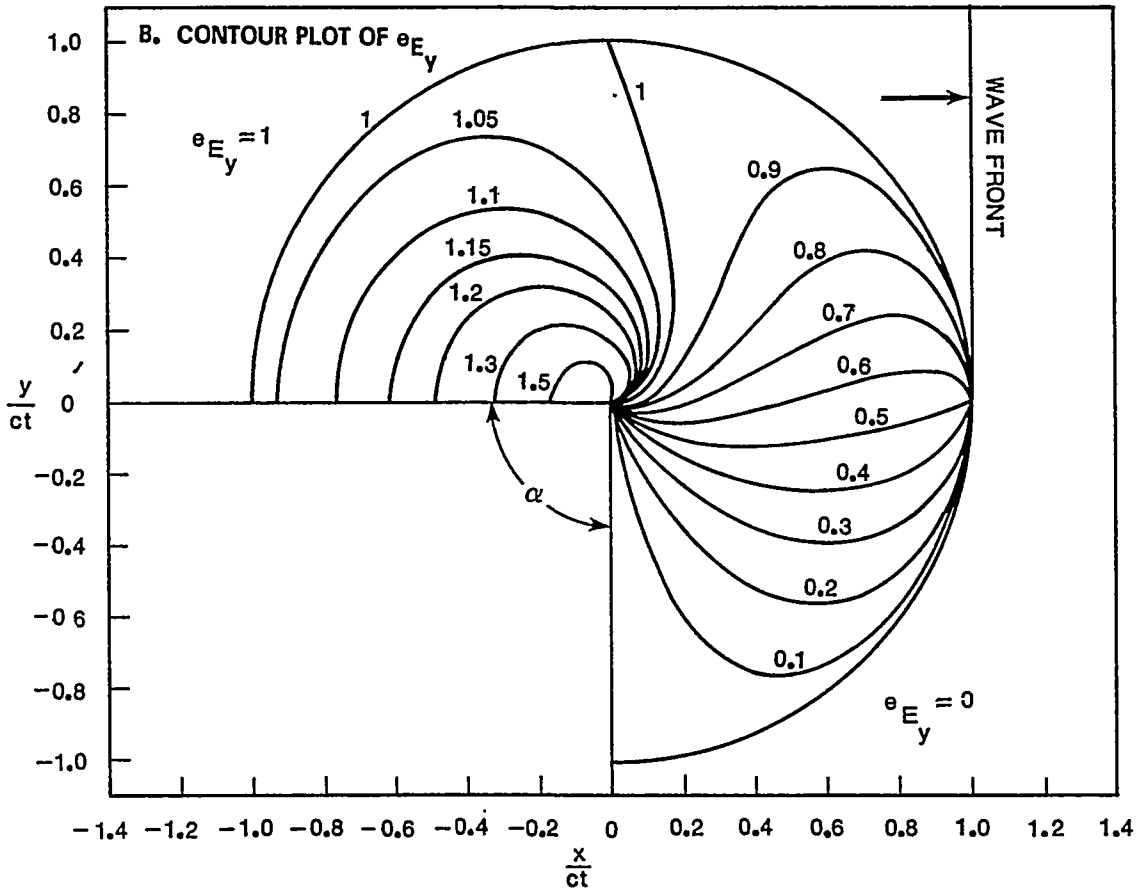

FIGURE 28. DIFFRACTION OF A STEP FUNCTION WAVE AT A BEND IN A PERFECTLY CONDUCTING SHEET FOR $\frac{\alpha}{\pi} = 0.5$

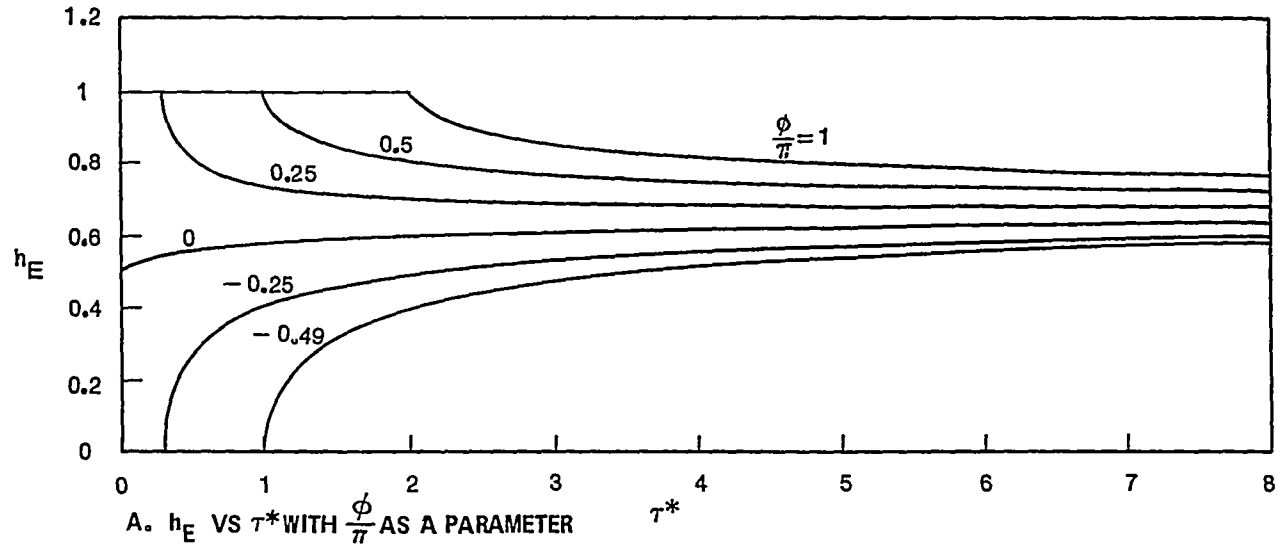

A. h_E VS τ^* WITH $\frac{\phi}{\pi}$ AS A PARAMETER

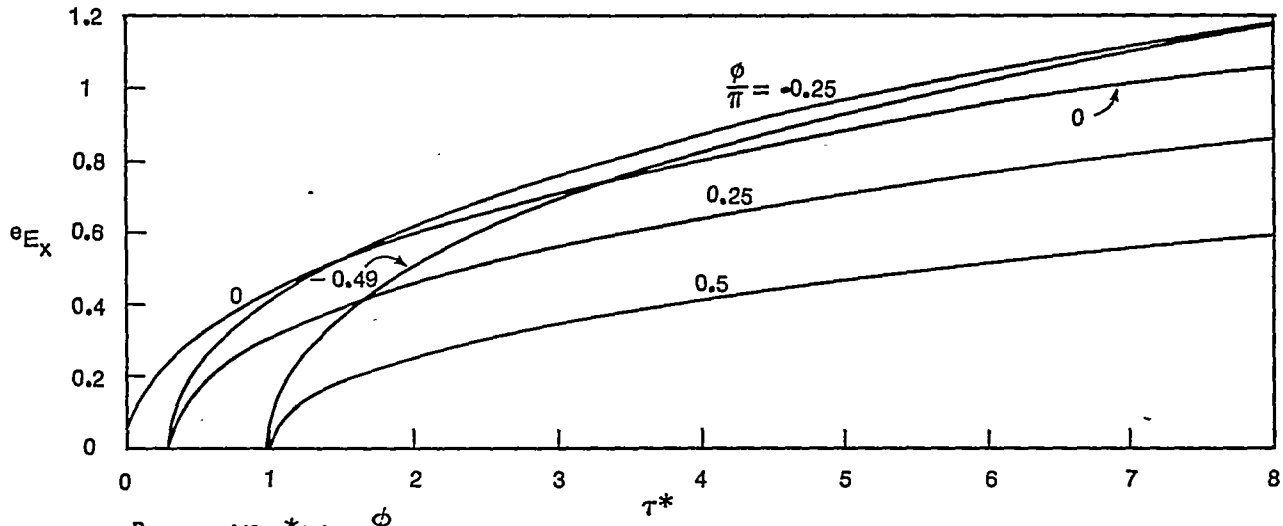

B. e_{E_x} VS τ^* WITH $\frac{\phi}{\pi}$ AS A PARAMETER

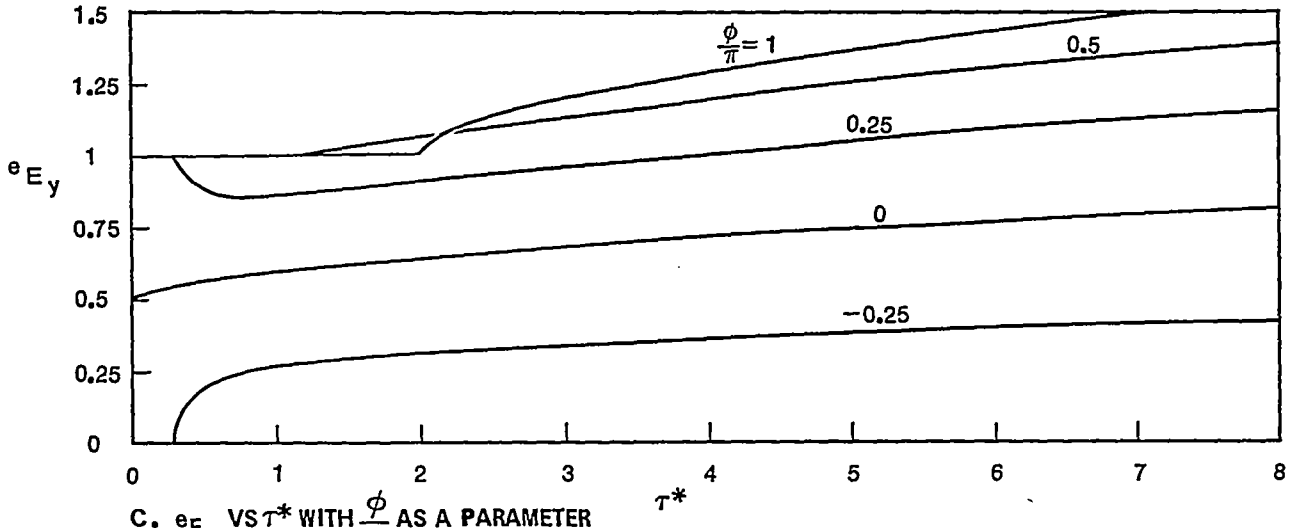

C. e_{E_y} VS τ^* WITH $\frac{\phi}{\pi}$ AS A PARAMETER

FIGURE 29. PULSE SHAPES FOR DIFFRACTION OF A STEP FUNCTION WAVE AT A BEND IN A PERFECTLY CONDUCTING SHEET $\frac{\alpha}{\pi} = 0.5$

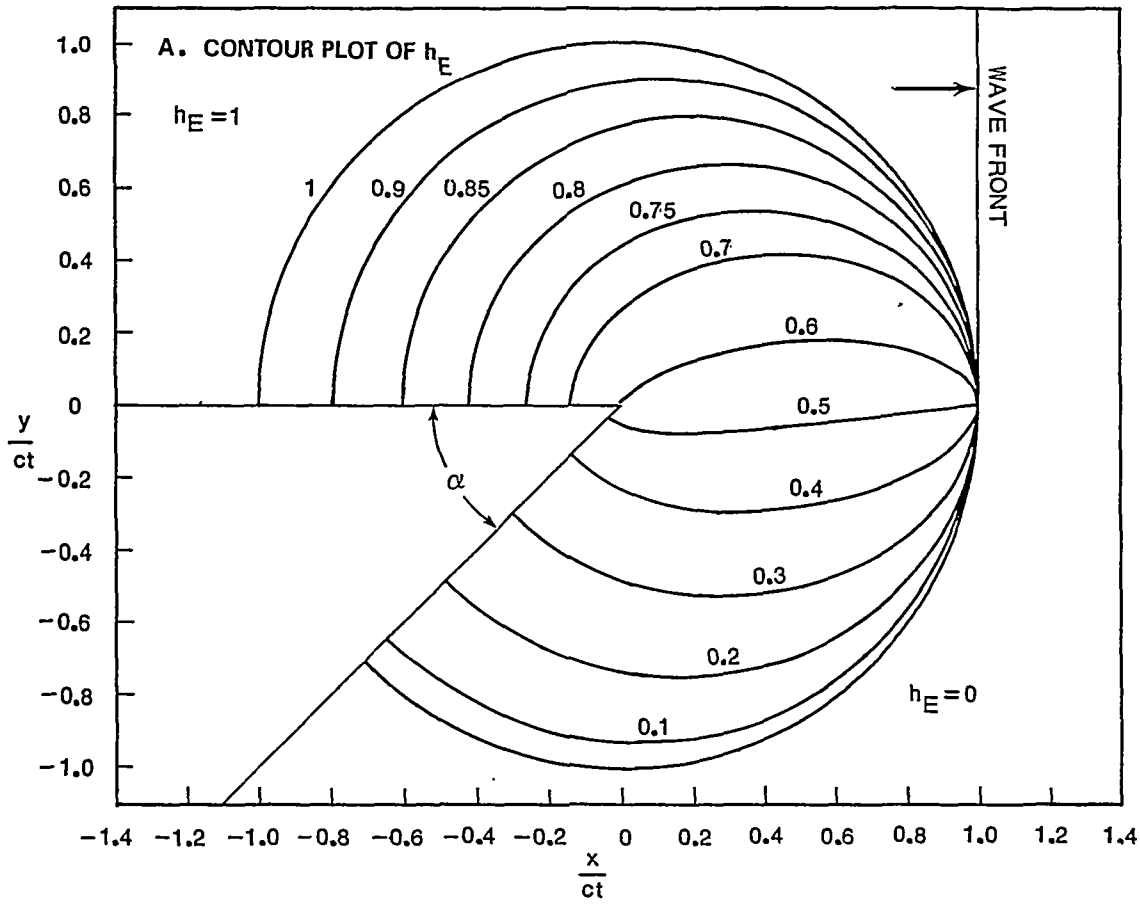

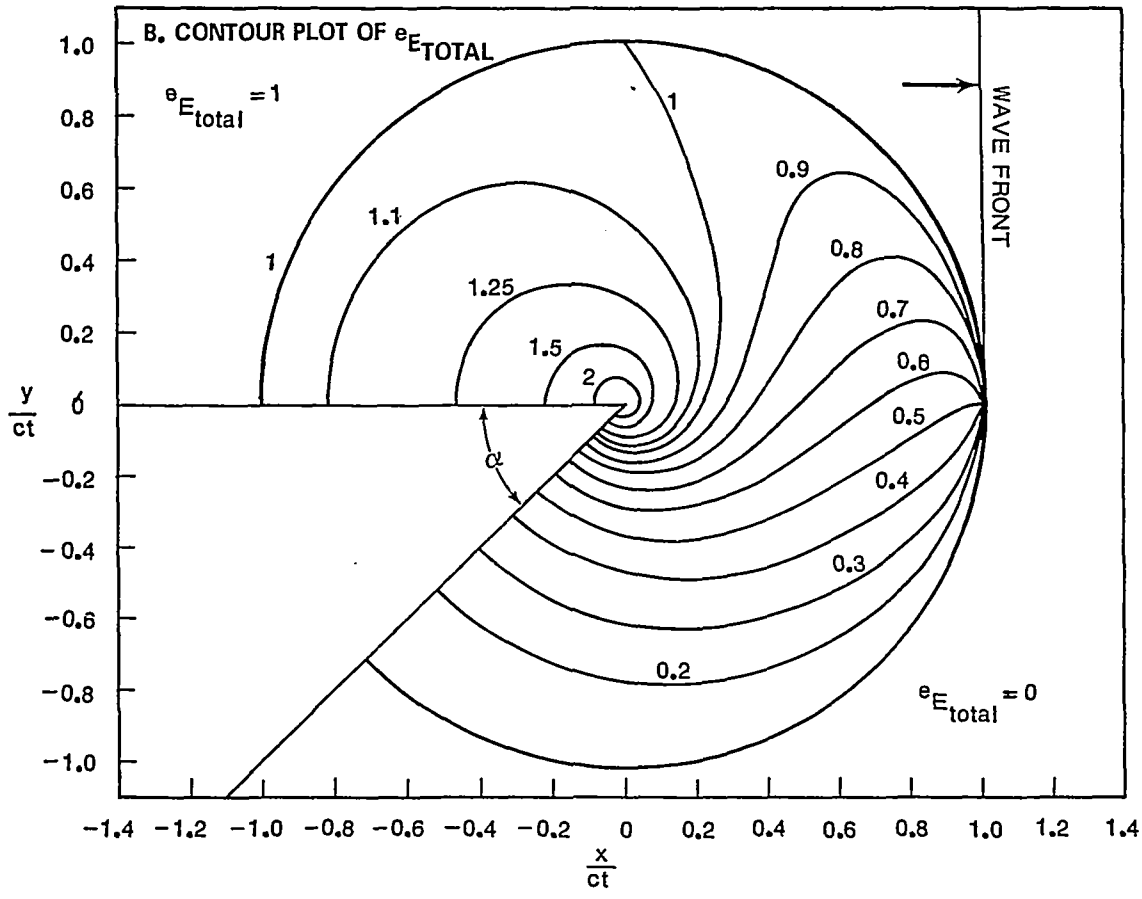

FIGURE 30. DIFFRACTION OF A STEP FUNCTION WAVE AT A BEND IN A PERFECTLY CONDUCTING SHEET FOR $\frac{\alpha}{\pi} = 0.25$

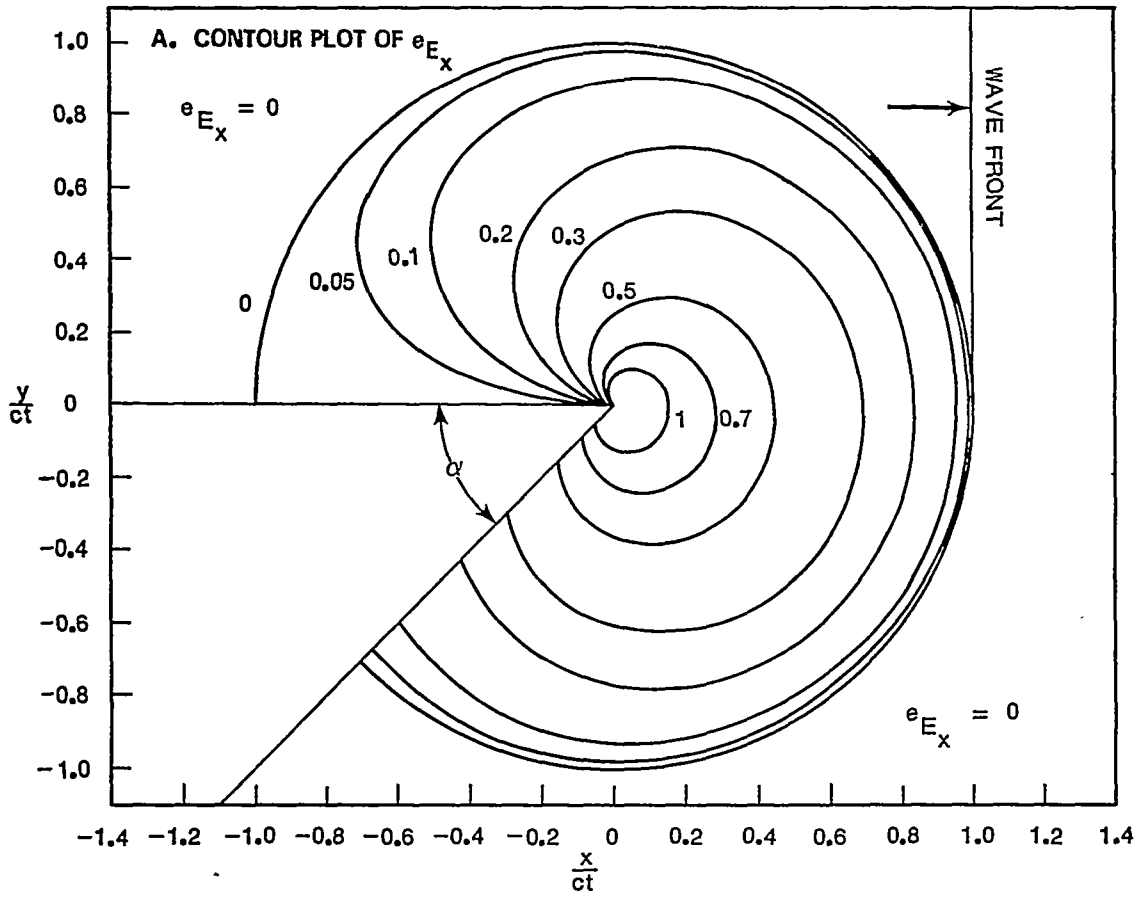

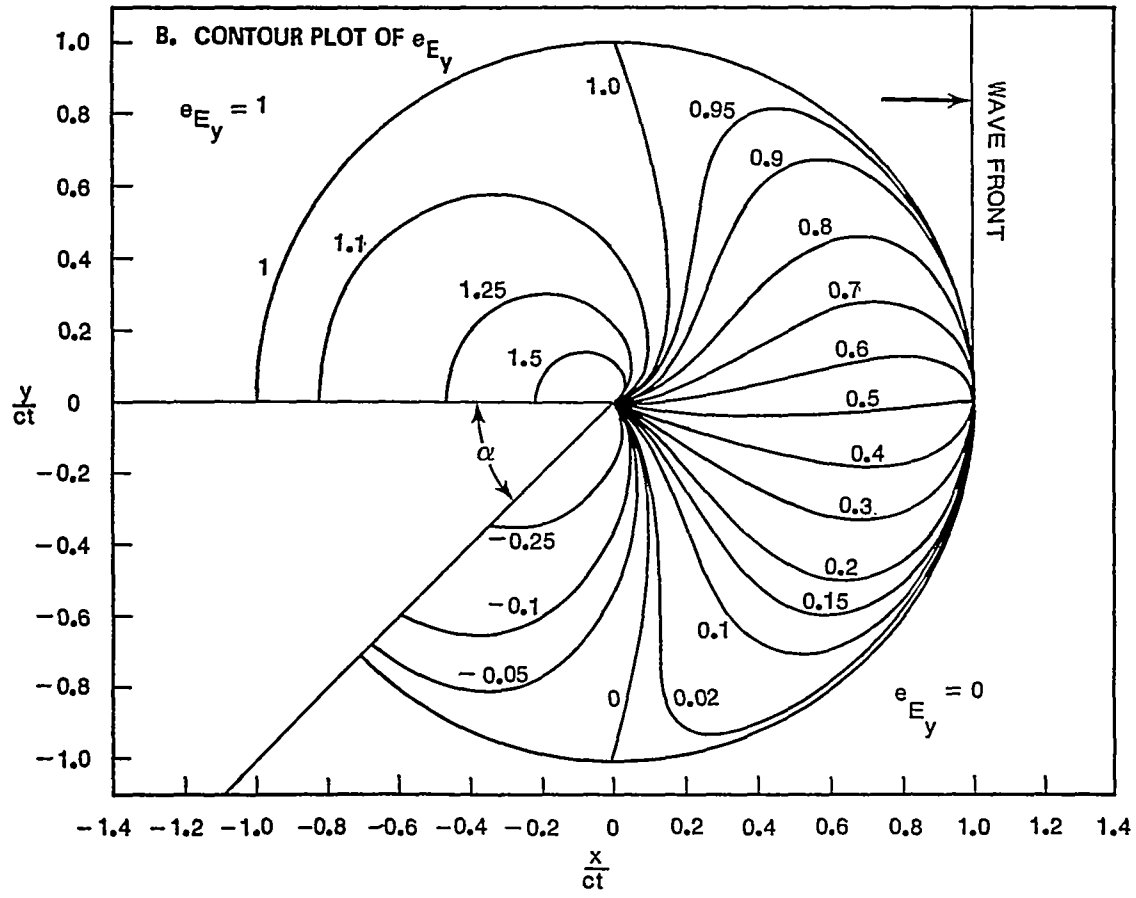

FIGURE 31. DIFFRACTION OF A STEP FUNCTION WAVE AT A BEND IN A PERFECTLY CONDUCTING SHEET FOR $\frac{\alpha}{\pi} = 0.25$

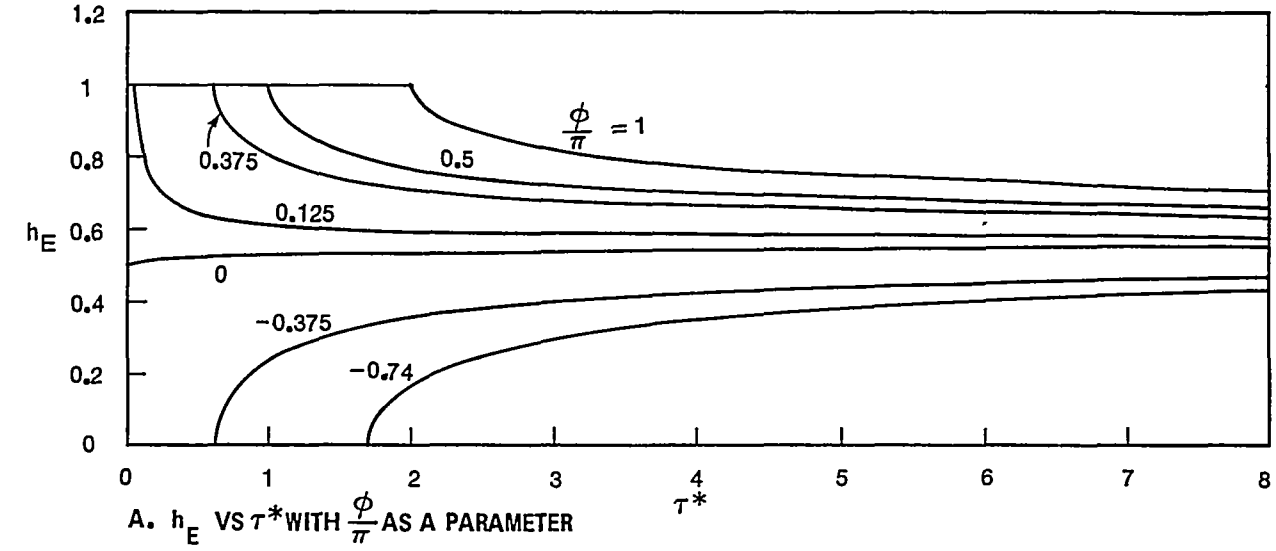

A. h_E VS τ^* WITH $\frac{\phi}{\pi}$ AS A PARAMETER

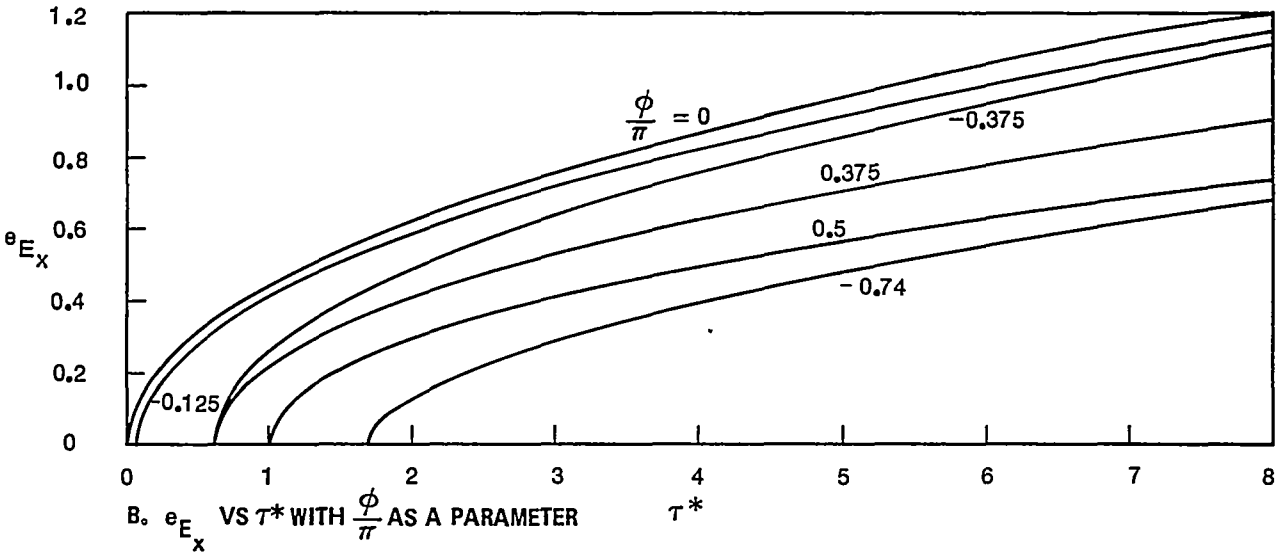

B. e_{E_x} VS τ^* WITH $\frac{\phi}{\pi}$ AS A PARAMETER

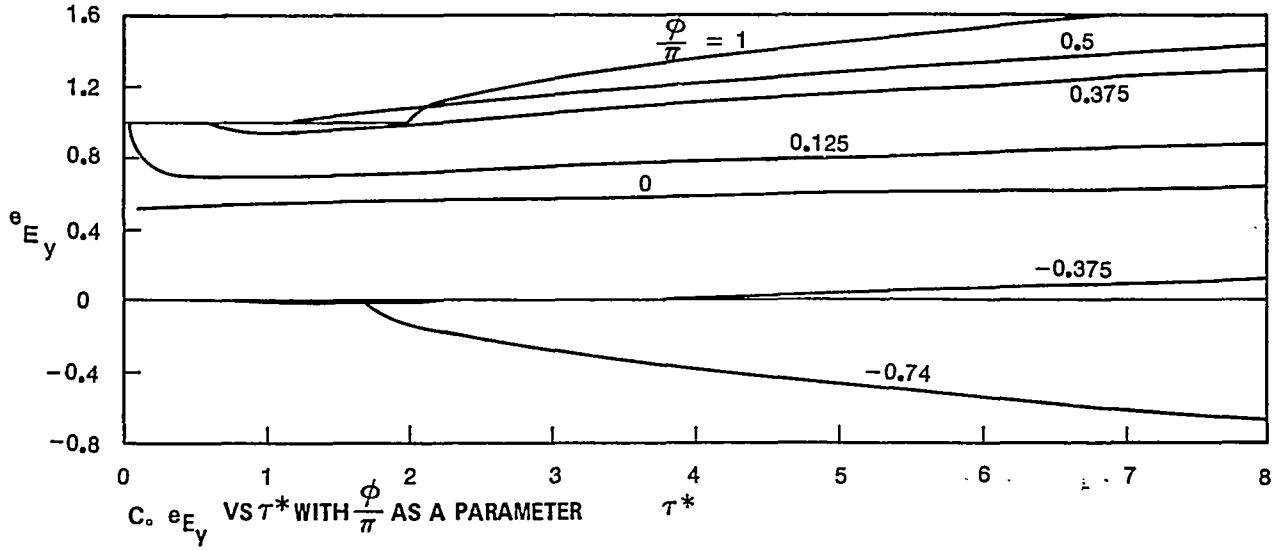

C. e_{E_y} VS τ^* WITH $\frac{\phi}{\pi}$ AS A PARAMETER

FIGURE 32. PULSE SHAPES FOR DIFFRACTION OF A STEP FUNCTION WAVE AT A BEND IN A PERFECTLY CONDUCTING SHEET $\frac{\alpha}{\pi} = 0.25$

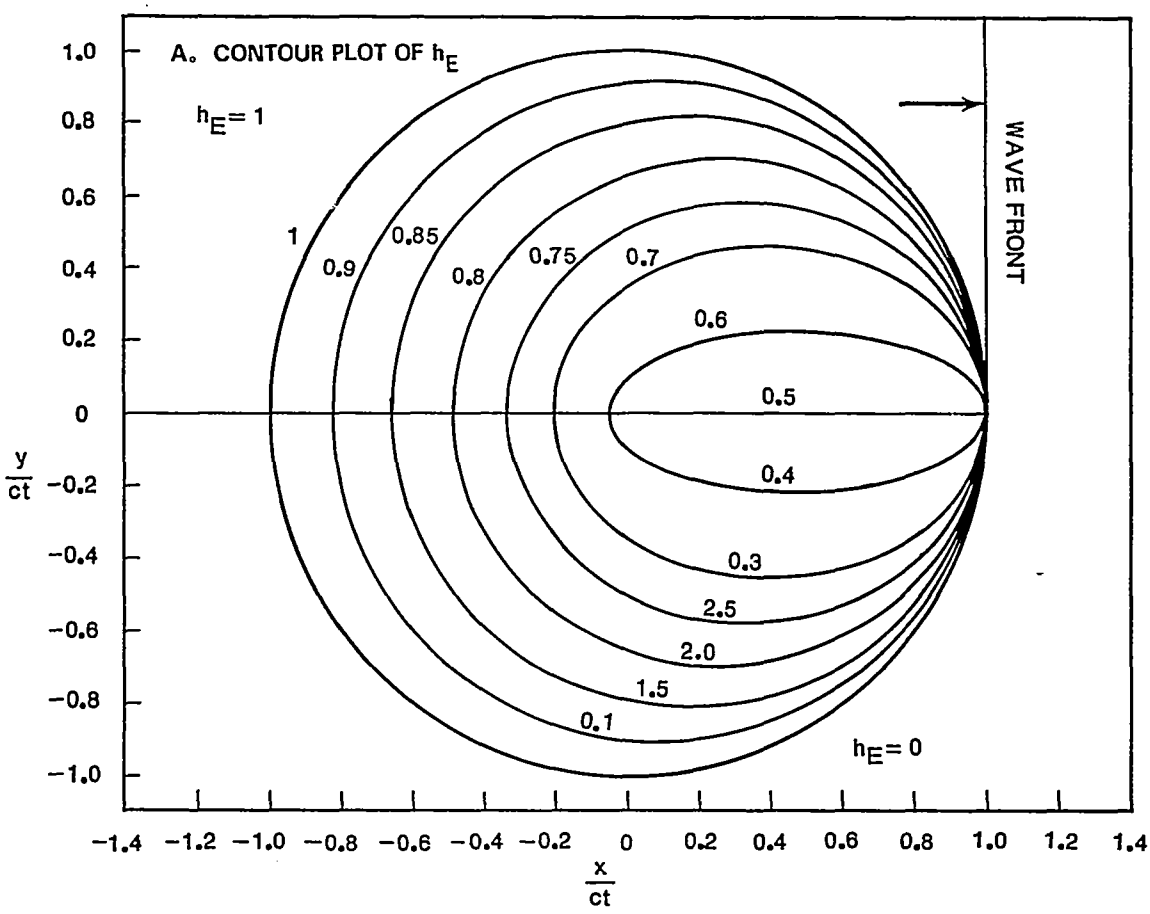

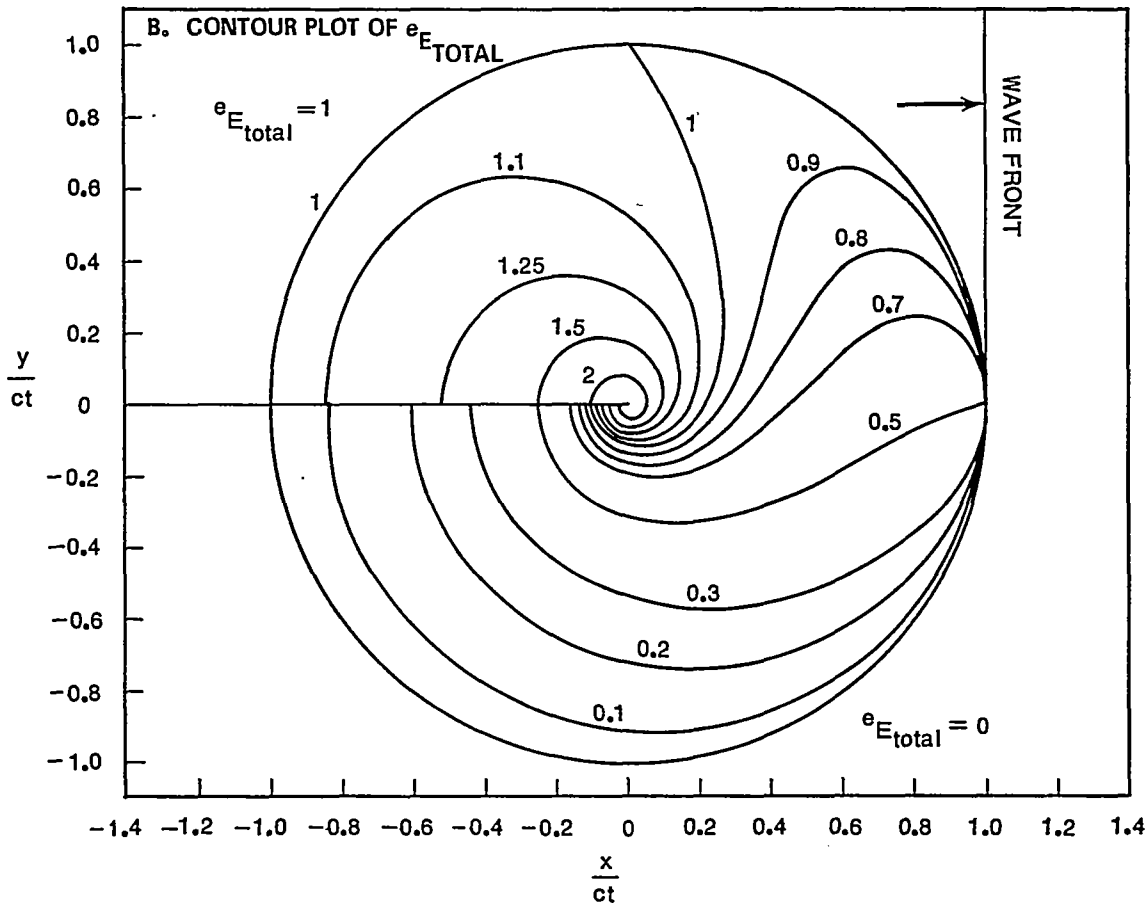

FIGURE 33. DIFFRACTION OF A STEP FUNCTION WAVE AT A BEND IN A PERFECTLY CONDUCTING SHEET FOR $\frac{\alpha}{\pi}=0$

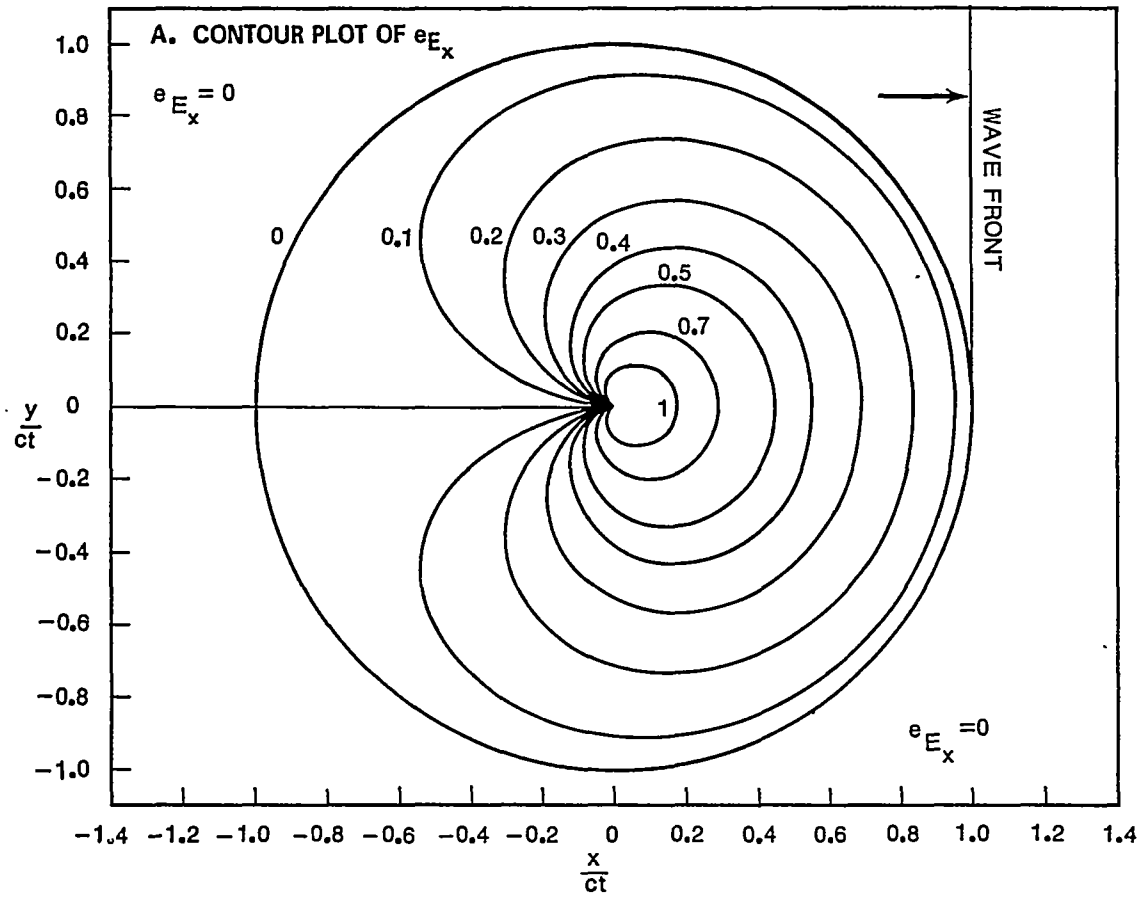

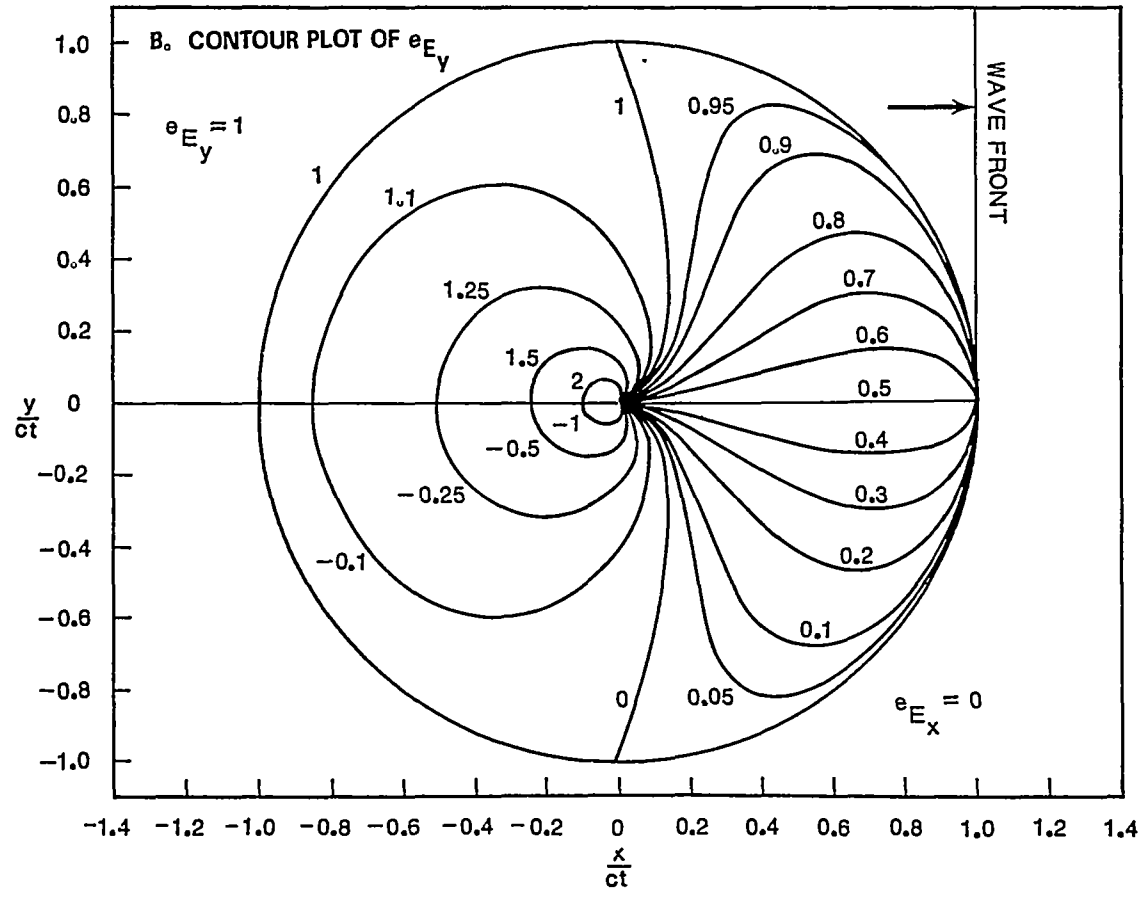

FIGURE 34. DIFFRACTION OF A STEP FUNCTION WAVE AT A BEND IN A PERFECTLY CONDUCTING SHEET FOR $\frac{\alpha}{\pi} = 0$

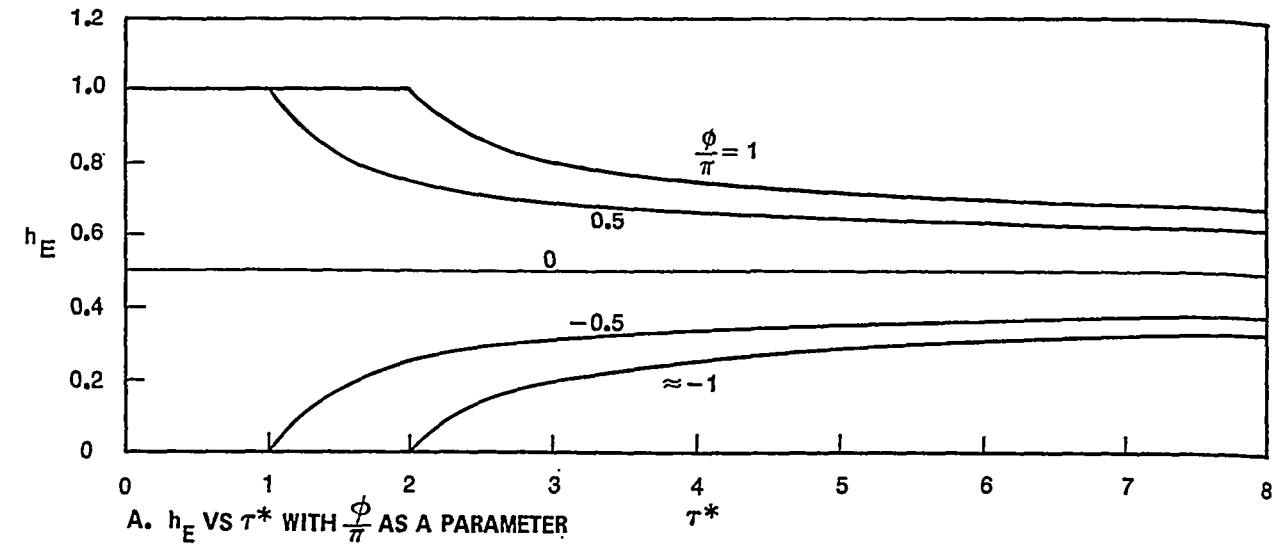

A. h_E VS τ^* WITH $\frac{\phi}{\pi}$ AS A PARAMETER

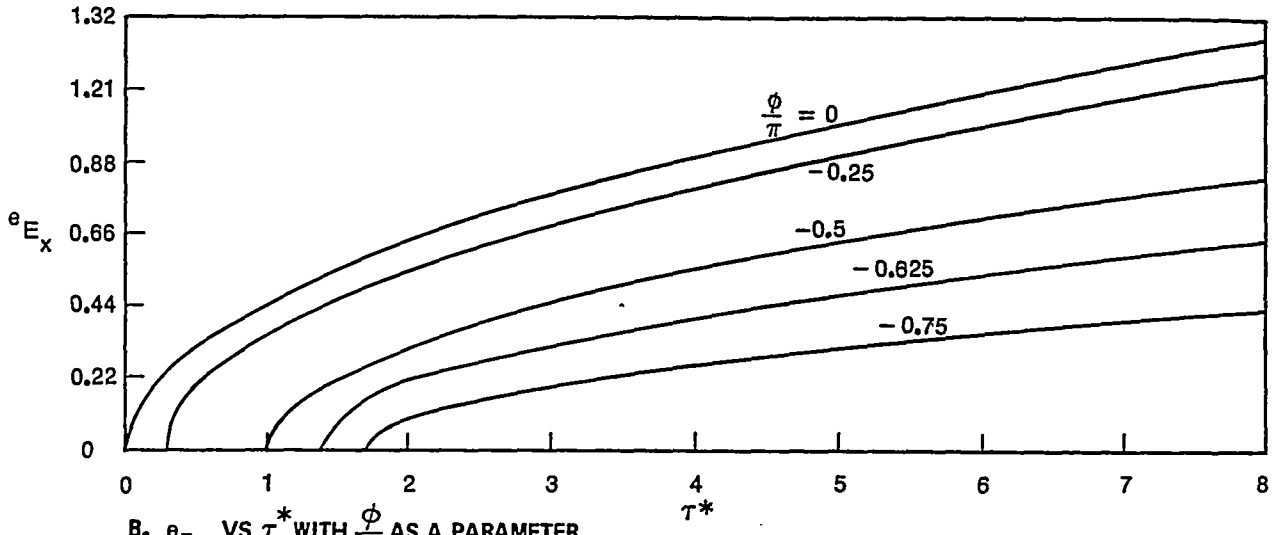

B. e_{E_x} VS τ^* WITH $\frac{\phi}{\pi}$ AS A PARAMETER

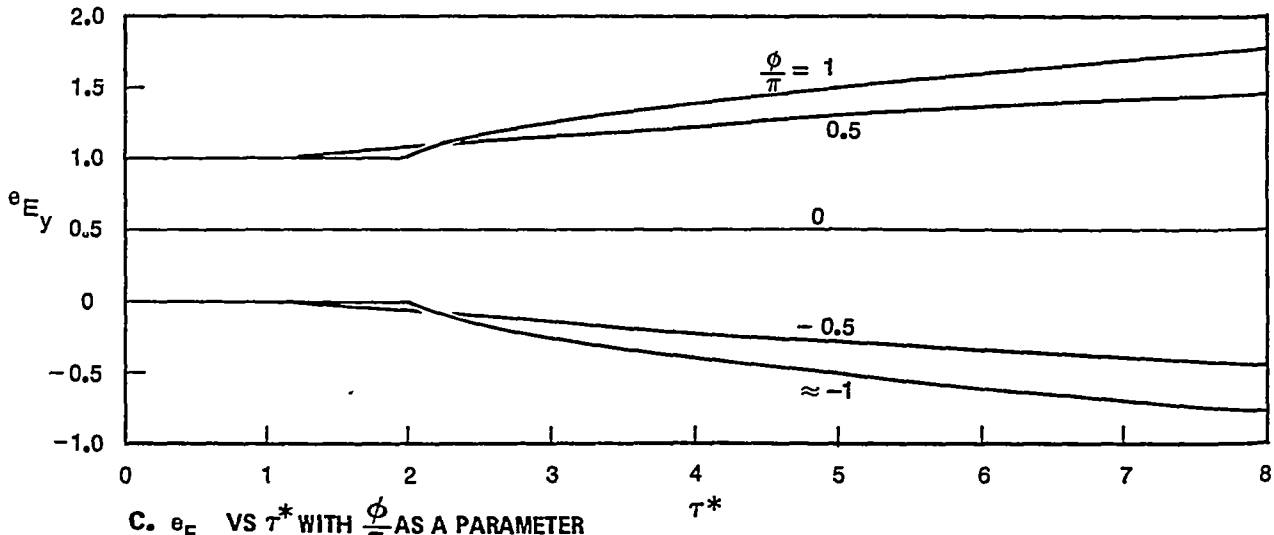

C. e_{E_y} VS τ^* WITH $\frac{\phi}{\pi}$ AS A PARAMETER

FIGURE 35. PULSE SHAPES FOR DIFFRACTION OF A STEP FUNCTION WAVE AT A BEND IN A PERFECTLY CONDUCTING SHEET $\frac{\alpha}{\pi} = 0$